2012

The Behavior Of Cerium Oxide Nanoparticles In Polymer Electrolyte Membranes In Ex-situ And In-situ Fuel Cell Durability Tests

Benjamin Pearman
University of Central Florida

THE BEHAVIOR OF CERIUM OXIDE NANOPARTICLES IN POLYMER ELECTROLYTE MEMBRANES IN EX-SITU AND IN-SITU FUEL CELL DURABILITY TESTS

by

BENJAMIN PIETER PEARMAN
MChem University of Bath, 2007

A dissertation submitted in partial fulfillment of the requirements
for the degree of Doctor of Philosophy
in the Department of Chemistry
in the College of Sciences
at the University of Central Florida
Orlando, Florida

Fall Term
2012

Major Professor: Michael D. Hampton

ABSTRACT

Fuel cells are known for their high efficiency and have the potential to become a major technology for producing clean energy, especially when the fuel, e.g. hydrogen, is produced from renewable energy sources such as wind or solar. Currently, the two main obstacles to wide-spread commercialization are their high cost and the short operational lifetime of certain components.

Polymer electrolyte membrane (PEM) fuel cells have been a focus of attention in recent years, due to their use of hydrogen as a fuel, their comparatively low operating temperature and flexibility for use in both stationary and portable (automotive) applications.

Perfluorosulfonic acid membranes are the leading ionomers for use in PEM hydrogen fuel cells. They combine essential qualities, such as high mechanical and thermal stability, with high proton conductivity. However, they are expensive and currently show insufficient chemical stability towards radicals formed during fuel cell operation, resulting in degradation that leads to premature failure. The incorporation of durability improving additives into perfluorosulfonic acid membranes is discussed in this work.

Cerium oxide (ceria) is a well-known radical scavenger that has been used in the biological and medical field. It is able to quench radicals by facilely switching between its Ce(III) and Ce(IV) oxidation states.

In this work, cerium oxide nanoparticles were added to perfluorosulfonic acid membranes and subjected to ex-situ and in-situ accelerated durability tests.

The two ceria formulations, an in-house synthesized and commercially available material, were found to consist of crystalline particles of 2 – 5 nm and 20 – 150 nm size, respectively, that did not change size or shape when incorporated into the membranes.

At higher temperature and relative humidity in gas flowing conditions, ceria in membranes is found to be reduced to its ionic form by virtue of the acidic environment. In ex-situ Fenton testing, the inclusion of ceria into membranes reduced the emission of fluoride, a strong indicator of degradation, by an order of magnitude with both liquid and gaseous hydrogen peroxide. In open-circuit voltage (OCV) hold fuel cell testing, ceria improved durability, as measured by several parameters such as OCV decay rate, fluoride emission and cell performance, over several hundred hours and influenced the formation of the platinum band typically found after durability testing.

ACKNOWLEDGEMENTS

I would first like to thank God for graciously providing the school, FSEC, the research, the finances and especially the people who have encouraged, pushed, consoled and cajoled me in the ways I needed to perform and finish the work presented here.

There are many people I owe much to for getting me here.

Thank you, FSEC hydrogen team. I could not have asked for a better group.

Nahid, thank you for your daily supervision, your ideas, your availability to answer any and all questions, your encouragement and all your out-of-work time. This dissertation would not exist without you.

Dr. Slattery, thank you for striking a delicate balance between pressure and encouragement. Thank you for taking such a committed interest in my academic and financial well-being, for going the extra mile to make sure I was taken care of.

Dr. Hampton, thank you for your willingness to take me on as a PhD student in my time of need. Thank you for your patience, availability, pressure and encouragement.

Dr. Diaz, thank you for being my advisor in spite of the low payoff. Thank you for your knowledge, availability and commitment. You have been a great example to me.

Paul and Marianne, thank you for everything! Thanks for the laughs. Thanks for the lab supervision. Thanks for continually and patiently answering all my questions. Your efforts are written all over this dissertation.

Randy, thanks for going out of your way to help me get stuff done in the lab and life.

Jordan and Jigna, thank you for all the fun and the emotional and academic support.

Dr. Sudipta Seal and Dr. Ajay Karakoti, thank you for getting me started with ceria and helping me finish.

Dr. Richard Blair, Dr. Andres Campiglia, Dr. Christian Clausen and Dr. Cherie Yestrebsky for your hard work and willingness to be on my committee.

Dave Cullen, a big thank you for all your TEM and STEM efforts and contribution of knowledge to this endeavor.

Pete, Nick, thanks for the IC pains. I dedicate my fluoride emission graphs to you.

Dr. David Richardson, thank you for all your NMR help.

I have to thank my family for their chemistry genes. Thank you to my parents for everything they have done to get me here and specifically providing ample accommodation for the duration of my studies. Thank you to Jim and Jody for setting me up at FSEC in the first place. Thank you to my grandparents for their interest in my work and manifold support.

I would gratefully like to acknowledge several funding sources and characterization facilities:

Financial support was provided by the Department of Energy through the Florida Hydrogen Initiative, contract #DE-FC36-04GO14225.

This research was supported in part by Oak Ridge National Laboratory's ShaRE User Facility, which is sponsored by the Office of Basic Energy Sciences, U.S. Department of Energy. The sample preparation expertise of Dr. Shawn Reeves and XPS capabilities of Dr. Harry Meyer III were greatly appreciated.

Some of the data for this work was obtained on instrumentation at the Materials Characterization Facility, Advanced Materials Processing & Analysis Center at the University of Central Florida. A special thank you must go to Kirk Scammon.

DART mass spectroscopy measurements were performed at the Department of Chemistry at the Florida Institute of Technology. A great thank you to Dr. Nasri Nesnas for his and his students' time.

Thanks to J.M. Zuo and J.C. Mabon for their Web-based Electron Microscopy Application Software: Web-EMAPS, Microscopy Microanalysis 10 (Supplement S02), 2004;
URL: http://emaps.mrl.uiuc.edu/

TABLE OF CONTENTS

LIST OF FIGURES

LIST OF TABLES

LIST OF ACRONYMS/ABBREVIATIONS

CCM – Catalyst coated membrane

CV – Cyclic voltammetry

DI water – De-ionized water

DOE – U.S. Department of Energy

EW – Equivalent weight

FC – Fuel cell

FER - Fluoride emission rate

GDL – Gas diffusion layer

HFR – High frequency resistance

IC – Ion chromatography

IEC – Ion-exchange capacity

LSV – Linear sweep voltammetry

MEA – Membrane electrode assembly

OCV – Open circuit voltage

PEM – Polymer electrolyte membrane

PEMFC - Polymer electrolyte membrane fuel cell

RH – Relative humidity

ROS – Reactive oxygen species

SEM – Scanning electron microscope

STEM – Scanning transmission electron microscope

TEM – Transmission electron microscope

TFA – Trifluoroacetic acid

XPS – X-ray photoelectron spectroscopy

XRD – X-ray diffraction

xx/xx/xx (e.g. 25/25/25) – cell temperature/anode temperature/cathode temperature

yy/yy (e.g. H_2/N_2) – anode fuel/cathode fuel

CHAPTER 1: INTRODUCTION

1.1 Fuel Cells Background

A fuel cell is an electrochemical cell that converts chemical energy from a supplied fuel directly to electricity. The types of fuel cells that are currently of most interest are listed in Table 1. The main differentiating factors between the technologies are the electrolyte used, the fuel consumed, and their operating temperature.

Table 1 Main types of fuel cells [1-3]

Fuel Cell Type	Operating Temperature	Fuel	Examples
Polymer Electrolyte Membrane	60 - 120 °C	Hydrogen	Mercedes F-Cell
Direct Alcohol	~90 °C	Methanol, Ethanol	PolyFuel, Samsung
Alkaline	60 - 120 °C	Hydrogen	Space Shuttle
Phosphoric acid	160 - 220 °C	Hydrogen	UTC Power
Molten Carbonate	600 - 700 °C	Most hydrocarbons	MTU Friedrichshafen
Solid Oxide	800 - 1000 °C	Most hydrocarbons	Bloom Energy; Ceramic Fuel Cells

Fuel cells are a technology of great interest, mainly for their high efficiency and low emissions. When combined with heat recovery, system energy conversions rates of up to 80% are possible. Ceramic Fuel Cells has published data demonstrating that their stationary solid oxide fuel cells can achieve over 50% electrical efficiency from natural gas over a period of 18 months while reaching a total energy efficiency of over 80% through water heating [4]. Especially hydrogen fuel cells, whose only exhaust product is

water, are touted for their clean energy credentials. Hydrogen gas is of great interest as a storage medium for intermittent renewable energy resources such as solar and wind power. During the daytime and high winds, excess power is used to create hydrogen, through electrolysis of water or other methods, which is subsequently converted to electricity during periods of low production. This part of the proposed hydrogen economy could help alleviate the difficulty of modulating the inevitable powder grid fluctuations caused by these renewable energy sources, making them more viable for proliferation.

1.2 Polymer Electrolyte Membrane Fuel Cell Operation

Polymer electrolyte membrane fuel cells (PEMFCs) have been the recipient of the most research attention, due to their operating temperature range, use of hydrogen as a fuel, and flexibility in application. This technology has found uses in both stationary and portable systems and is the leading alternative to internal combustion engines (ICEs) in cars, buses and trucks [2, 5].

$$H_2 \rightarrow 2\ H^+ + 2\ e^- \qquad (1.1)$$

$$\tfrac{1}{2}\ O_2 + 2\ e^- + 2\ H^+ \rightarrow H_2O \qquad (1.2)$$

$$H_2 + \tfrac{1}{2}\ O_2 \rightarrow H_2O \qquad E_0 = 1.23\ V \qquad (1.3)$$

The reaction of hydrogen with oxygen (Equation 1.3) is well-known and mostly associated with very energetic explosions. In a fuel cell, the oxidation (Equation 1.1) and reduction reactions (Equation 1.2) are physically separated. Figure 1 shows a schematic of a PEMFC, which consists of five layers: the two gas supplies, which often involve diffusion media to evenly distribute the reactants to the reaction sites; the two electrodes with catalyst; most commonly platinum; and finally the polymer electrolyte membrane (PEM), that separates the two gas inlets both physically and electrically, but is able to transport protons from the anode to the cathode.

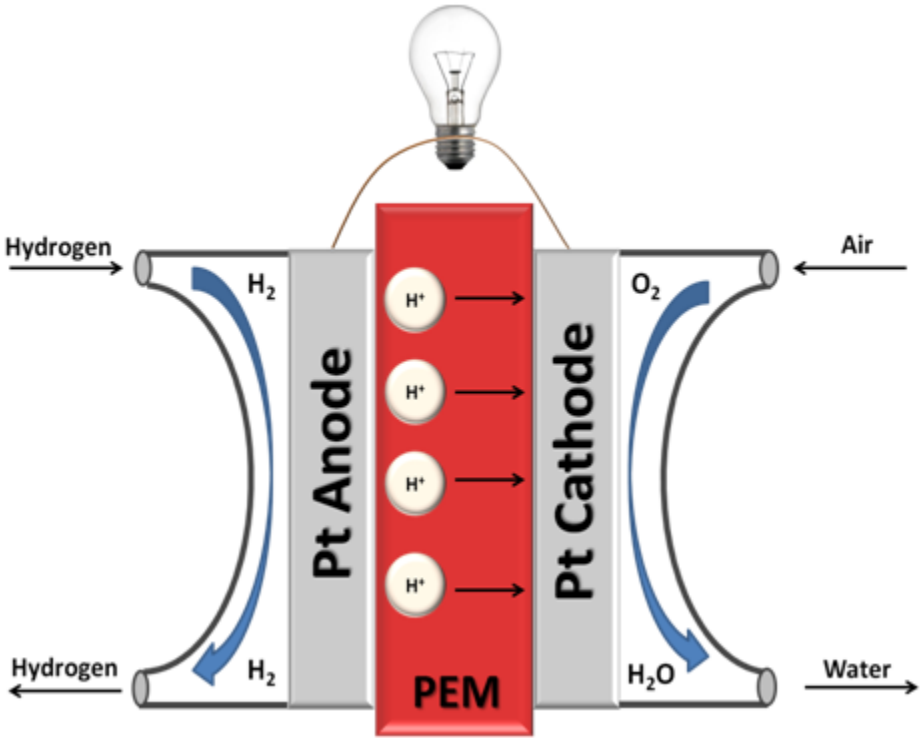

Figure 1 Schematic of a polymer electrolyte membrane fuel cell [6]

The splitting of hydrogen into protons, shown in Equation 1.1, occurs at the anode. The electrons released from this reaction are conducted via the circuit and provide the electrical power to the load (represented in Figure 1 as a light bulb). The protons are transported through the PEM to the cathode where they react with oxygen and the electrons to form water (Equation 1.2).

Consequently, membranes for PEMFCs need to exhibit the following properties:

- Impermeable to gases
- Mechanically stable towards compression and differential pressures
- Proton conducting
- Electrically insulating
- Thermally stable

The materials that have shown the best combination of these properties will be discussed in the following section.

1.3 Perfluorosulfonic Acid Membranes

1.3.1 Molecular Structure and Morphology

Perfluorosulfonic acid (PFSA) polymers, such as DuPont's Nafion®, 3M's Acquivion®, Asahi Glass' Flemion® or Dow's polymer [7], are the polymer class of choice for PEMFC. Of these, Nafion®, whose molecular structure is given in Figure 2, is the most heavily researched and the material against which all other PEMs are judged [8]. Though the listed polymers vary slightly, they all have the same basic structure: a main chain or backbone, consisting of polytetrafluoroethylene, and a side-chain ending in a sulfonate group. They are manufactured by the radical copolymerization of tetrafluoroethylene and a perfluorinated vinyl ether monomer that contains a sulfonyl fluoride functional group that is converted to the sulfonate group as part of the synthesis [7, 8]. As the sulfonate group is ionically bound to a proton, making it a sulfonic acid, these materials are referred to as ionomers.

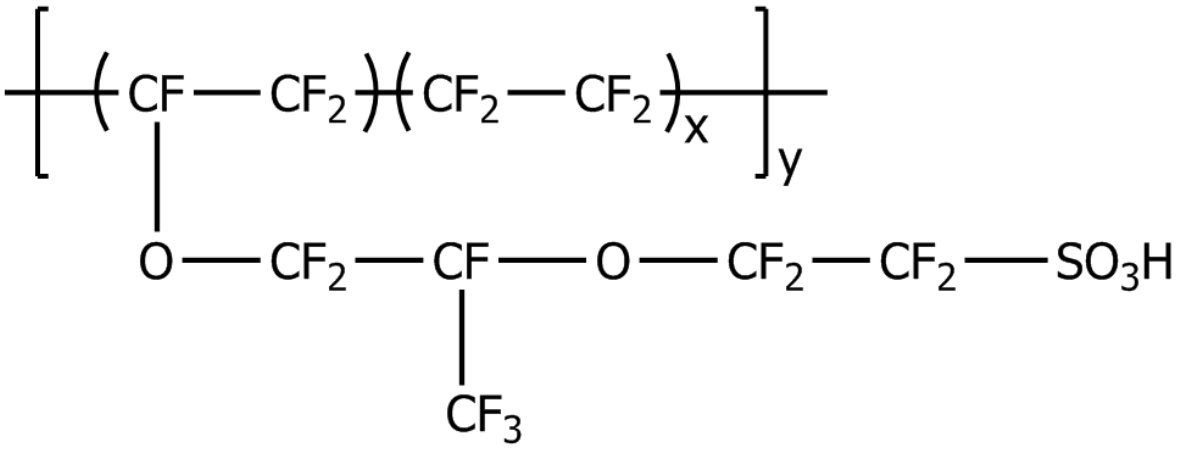

Figure 2 Molecular structure of Nafion®

Determining the molecular weight of these polymers is difficult and they are generally classified by their equivalent weight (EW) or ion exchange capacity (IEC). The equivalent weight (g eq^{-1}) is the measure of polymer mass per equivalent (or molar concentration) of the sulfonic acid. It is calculated using Equation 1.4.

$$\mathrm{EW} = \frac{\mathrm{m(ionomer)}}{\mathrm{n(sulfonate\ groups)}} \qquad (1.4)$$

The IEC (Units: meq g^{-1}) is the inverse of the equivalent weight. EWs of 1100 g eq^{-1} (IEC of 0.91 meq g^{-1}) are typical for PEMs used in fuel cells and were also employed in this study. For such equivalent weights, the value of x in Figure 2 would be approximately seven, though it must be noted that due to the random nature of the polymerization reaction, the frequency of side-chains is irregular and the EW must be viewed as an average bulk value.

One of the defining features of Nafion®'s physical structure is the presence of both highly hydrophobic (backbone) and the highly hydrophilic (side-chain) domains. The main chain aligns to form crystalline regions that give the material its mechanical strength. At the same time, clusters of sulfonic acid groups in hydrated membranes yield interconnected hydrophilic domains which provide the pathways that allow proton conduction. The physical structure of Nafion® is still not completely resolved and is outside the scope of this work [8], though some important aspects will be touched on in the following sections.

1.3.2 Proton Conductivity

The clustering of the ionic side-chains is one of the important features of PFSAs, providing the ability to transport ions, which in the case of hydrogen fuel cells are protons. The first morphological structure proposed for such proton-conduction pathways was the cluster-network by Gierke *et al.* [9]. Though other models have been suggested since its inception 30 years ago, its basic approach still gives an adequate understanding of the way Nafion® works [8]. This model, illustrated in Figure 3, shows how side-chain clusters, under humidified conditions, result in the formation of a sulfonate group-lined pathway. The transport of protons occurs via two mechanisms:

- Grotthus mechanism: protons "hop" from one sulfonic acid group to sulfonic acid group through the membrane
- Water transport: protons, as H_3O^+ or $H_2O_5^+$ molecules diffuse through the membrane (considered to be about 20% of the overall proton mobility [10])

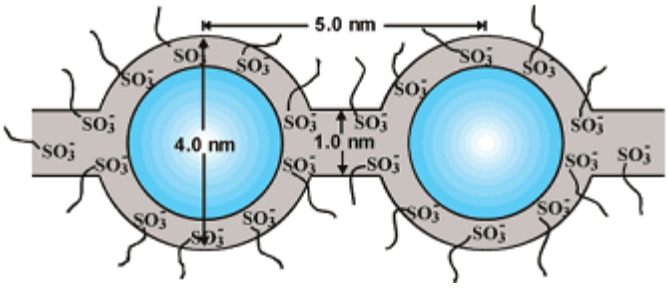

Figure 3 Cluster-network model of Nafion® (blue circle is water) (Reprinted with permission from [9] Copyright (2012) American Chemical Society)

Both mechanisms are dependent on the presence of water. The absorption of water causes membrane swelling that opens up the pathways for proton hopping and provides the molecular vehicle for diffusion. Though Nafion® demonstrates reasonably high proton conductivity (~0.1 S cm^{-1}), such values are only achieved at high relative humidity (>90% at 80 °C) and decrease dramatically as the RH is decreased. For an 1100 EW PTFE-supported PFSA membrane produced in-house the conductivity decreases 25-fold upon lowering the RH from 90 to 20%, as shown in Figure 4. For fuel cell operation, maintaining high humidities poses significant engineering problems in terms of water management, which increases complexity and adds to the already high cost of the overall system. This problem is further exacerbated when operating at higher temperatures. To increase the slow oxygen reduction kinetics and increase tolerance of the catalyst towards poisons such as carbon monoxide, operation above 100 °C is desirable. At these temperatures, water is vaporized and leaves the system which greatly impacts membrane conductivity and therefore cell performance and efficiency [2, 3, 5, 11].

One general approach to decrease membrane resistance is to reduce its thickness. This however leads to issues with mechanical and chemical durability. Another approach has been to decrease the EW, thereby increasing the number of sulfonic acid groups, leading to higher proton conductivity. Though successful, as can be seen from the remarkably higher conductivity of the 750 EW membrane in Figure 4, this approach is fraught with its own issues, especially with regards to mechanical stability. The higher

number of sulfonic acid groups result in a higher uptake of water and therefore increased membrane swelling. This increases gas permeability and leads to a loss in efficiency. Cycling between various humidities also causes mechanical stress that leads to premature cell failure due to crack or pinhole formation brought on by membrane fatigue. Other efforts have involved the use of highly proton conducting additives such as heteropolyacids and zirconia-based materials [12-15].

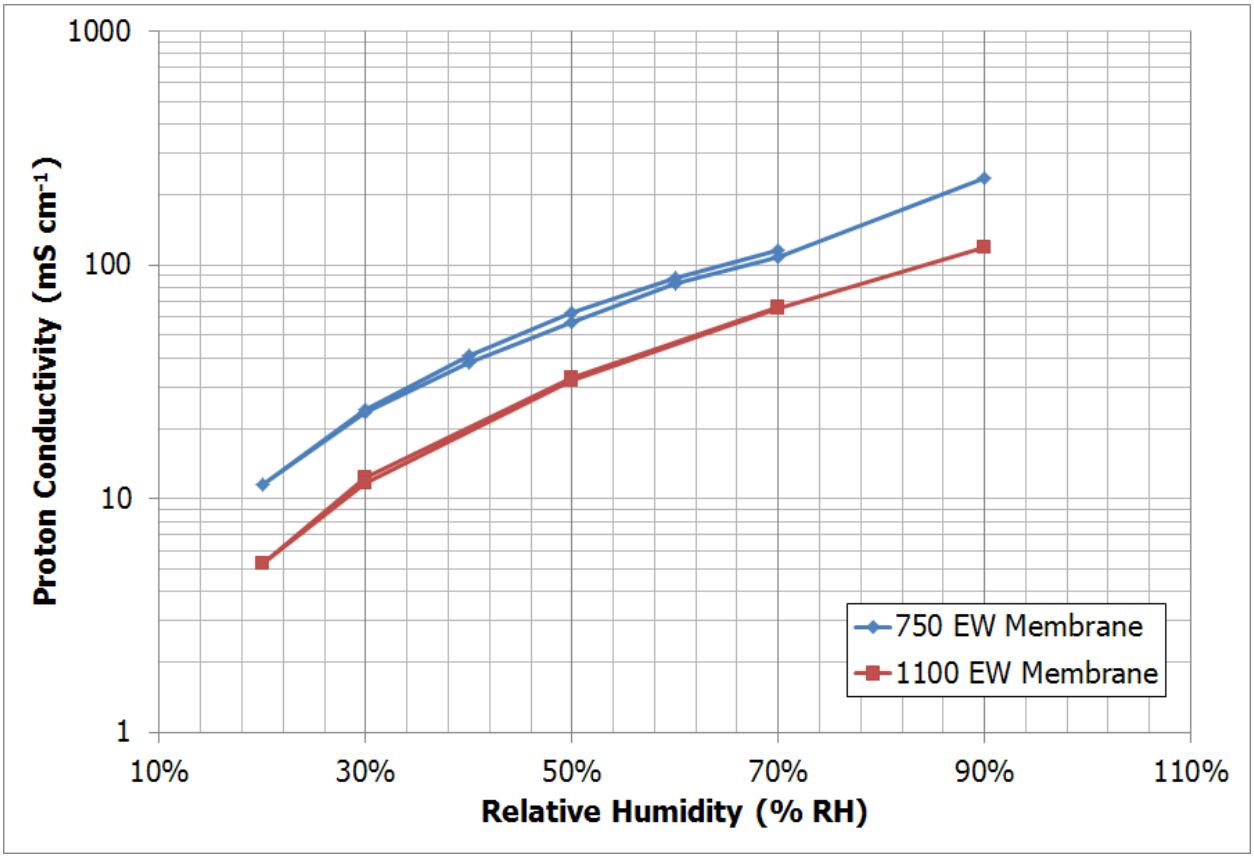

Figure 4 Proton conductivity as a function of relative humidity for 750 EW and 1100 EW PFSA membranes at 120 °C

1.3.3 Cost

The main obstacle facing the wide-spread commercialization of fuel cells has been their cost. One great factor in financial calculations is the lifetime of cell parts, especially with regard to membrane durability. Currently, no ionomer is commercially available that meets the Department of Energy (DOE) required targets of 5000 and 40000 hours in vehicular and stationary applications, respectively [16]. Some of the aspects of membrane durability, especially with regards to chemical stability and approaches to mitigate these issues will follow.

1.3.4 Mechanical Stability

Any amount of gas that crosses over from the anode to the cathode, and vice versa, is a loss in efficiency. Therefore, maintaining the mechanical integrity of the membrane is of vital importance. If a pinhole or crack forms, gas crossover increases greatly, leading to an unacceptable loss in performance and efficiency, resulting in effective cell failure.

Membranes in fuel cells are exposed to a number of stress factors:

- Mechanical pressure from cell building (plates, GDLs, catalyst layers, gaskets, etc.)
- Pressure differentials between the anode and cathode gases

- Cycling in membrane swelling from uptake and loss of water due to changes in relative humidity (the thickness can increase by up to 15% on changing the RH from 0 – 100% for 1100 EW PFSAs [17, 18])

Unfortunately, as a consequence of the described conduction pathways, even pristine Nafion® is permeable to gas diffusion, a fact that is exacerbated by the aforementioned drive to reduce the thickness of the membrane. A common approach to marry these contradicting requirements is to incorporate a reinforcing PTFE support [13, 16, 19], a technique also used in this study. Other successful systems have been developed, mainly networks of interconnected inorganic materials [12, 17, 18, 20-22].

1.3.5 Chemical Degradation

The mechanisms involved in membrane degradation are very complex and a matter of much debate. One important characteristic, however, is that reactant gas crossover plays a pivotal part in the process. Consequently, mechanical and chemical durability are closely linked [23, 24].

Reactive oxygen species (ROS), mainly hydroxyl ($HO^{\cdot}$) and hydroperoxyl ($HOO^{\cdot}$) radicals, are considered the degrading species in fuel cells. They are thought to be formed either from hydrogen peroxide or directly from hydrogen and oxygen on platinum [7, 8, 16, 20, 24-35].

$$O_2 + 2\ e^- + 2\ H^+ \rightarrow H_2O_2 \quad (1.5)$$

$$H_2 \rightarrow 2\ H_{Pt\ ads} \quad (1.6)$$

$$H_{Pt\ ads} + O_2 \rightarrow HOO_{Pt\ ads} \quad (1.7)$$

$$HOO_{Pt\ ads} + H_{Pt\ ads} \rightarrow H_2O_2 \quad (1.8)$$

It has been proposed that H_2O_2 is formed at the cathode via a 2-electron reduction of oxygen (Equation 1.5) or at the anode in a three step reaction (Equations 1.6, 1.7 and 1.8), involving hydrogen adsorbed on platinum and crossover oxygen. The peroxide then diffuses into the membrane where it reacts with Pt particles or other metal ion impurities to form radicals that degrade the membrane (Equation 1.9) [26, 36].

Hydrogen peroxide has been measured in fuel cell effluents and estimates suggest that during operation a consistent concentration of ~10 ppm is present [26, 37], making it a reasonable culprit for involvement in degradation process. However, other studies have cast doubt on its influence on the chemical decomposition of membranes. Mittal *et al.* demonstrated that using H_2O_2 as a reactant gas in place of hydrogen and oxygen, reduced the emission of fluoride by 25-30 times in OCV hold tests [34]. They also showed that the concentration of peroxide was independent of hydrogen crossover, while the emission of fluoride was not. Related work indicated that both hydrogen and oxygen, and not just one of the reagents, is required for significant degradation to

occur [24]. They, and others, have suggested the direct formation of radical species from reactions between H_2, O_2 and Pt at the electrodes or in the membrane though no specific mechanism was offered [36].

Regardless of the debate over the precise mechanism of ROS formation, there is consensus that such radicals are largely responsible for the degradation observed in PFSA-based fuel cells.

1.3.6 Degradation Mechanisms

In spite of its perfluorinated nature, Nafion® is susceptible to degradation under fuel cell conditions. The main points of attack that have been suggested are illustrated in Figure 5.

1. Carboxylic acid (COOH) end groups [25]
2. Sulfonic acid (SO_3H) end groups [26]
3. Ether-adjacent carbons atoms on the side-chain [38]
4. Abstraction of primary fluorine [26]

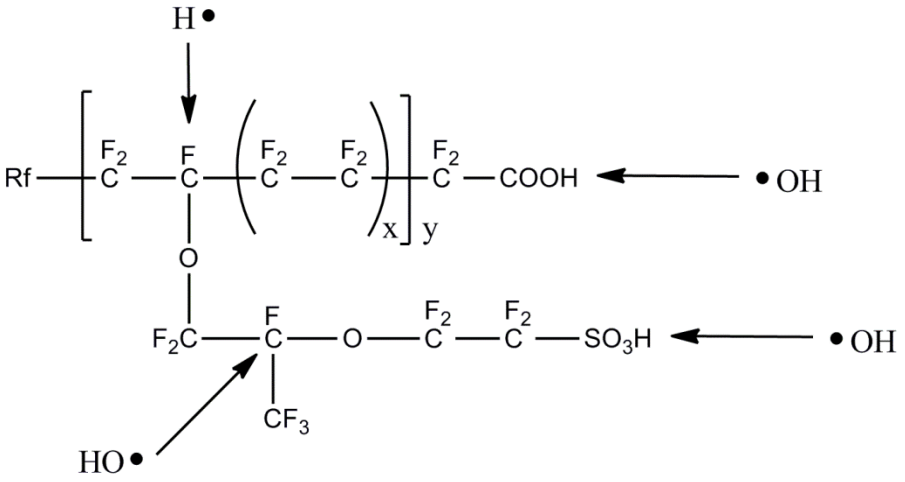

Figure 5 Radical attack points on PFSAs

The first recognized mechanism that is still considered to be the main source of degradation is the hydrogen abstraction from carboxylic acid end groups [25]. These groups are unavoidable impurities resulting from the polymerization process. The mechanism of degradation is shown in Figure 6.

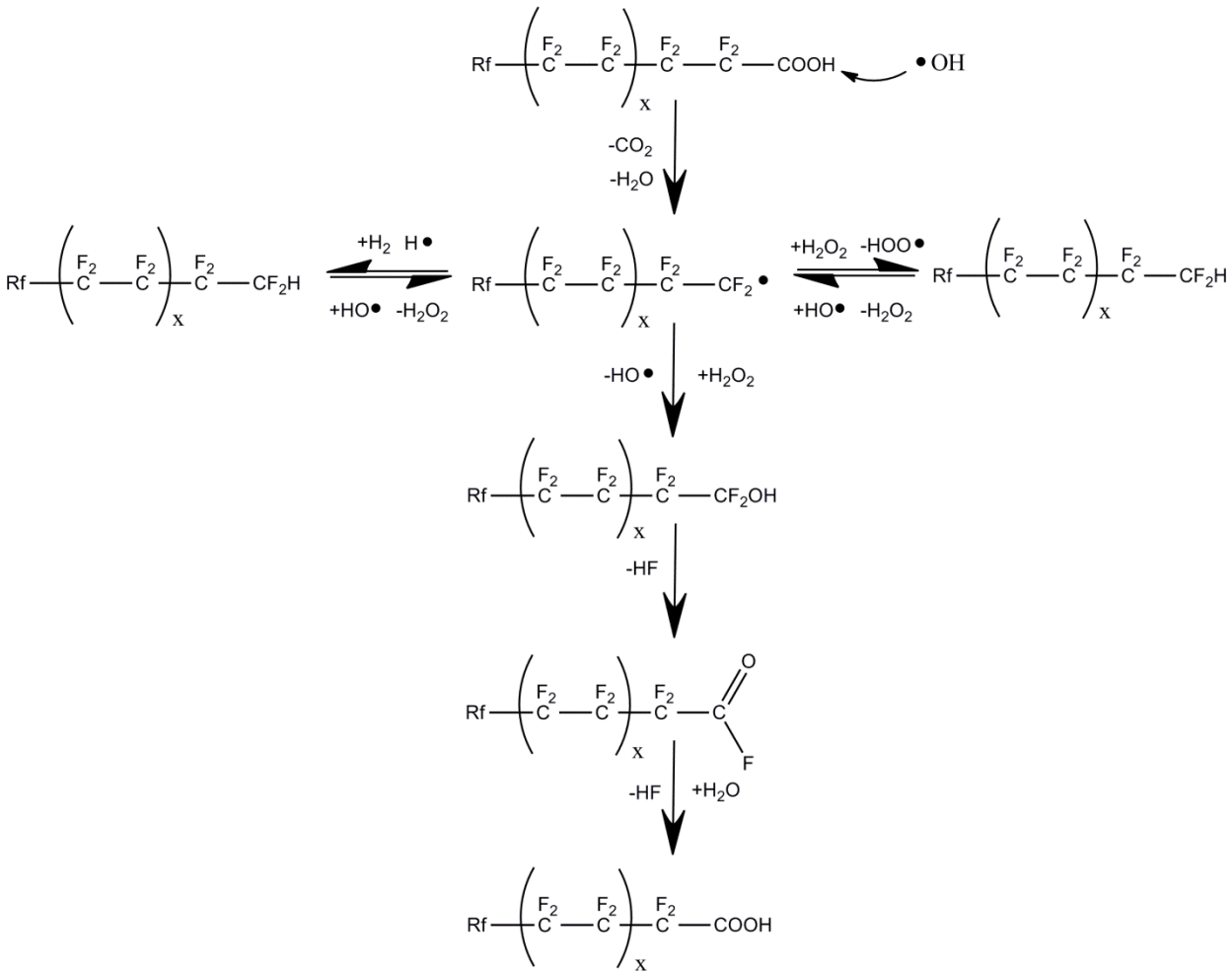

Figure 6 Main chain unzipping (redrawn from [26])

The COOH hydrogen atom is abstracted by a hydroxyl radical. The resultant radical decarboxylates forming a fluorocarbon radical. For the next step, Curtin *et al.* [25] originally proposed the reaction of this species with another hydroxyl radical. However, Coms [26] cognizantly argued that it was unlikely that two radicals, that are present at such low concentrations in the membrane, would react. Alternatively, he proposed three reactions, two of which are reversible. In the first reversible reaction, the fluorocarbon

radical abstracts a hydrogen atom from the crossover H_2 abundantly present during fuel cell operation. This results in the formation of a hydrogen radical that causes further damage, as will be shown later. In a similar reaction, hydrogen is abstracted from the consistently present hydrogen peroxide, which results in the formation of the hydroperoxyl radical. The end groups that form in these two reactions still contain a vulnerable hydrogen atom which is again subject to abstraction to form the original fluorocarbon radical.

The irreversible reaction, which was originally proposed to occur with another $HO^{\cdot}$, is a reaction of the fluorocarbon radical with H_2O_2 to form an alcohol with the release of a hydroxyl radical. Accompanied by the loss of HF, the alcohol rearranges to an acid fluoride, which itself is hydrolyzed, releasing another hydrogen fluoride molecule and re-forming the carboxylic acid group. The reaction is summarized in Figure 7. Through the attack of a radical, a CF_2 unit is lost with the re-formation of the carboxylic acid. The whole process is repeated, effectively unzipping the backbone.

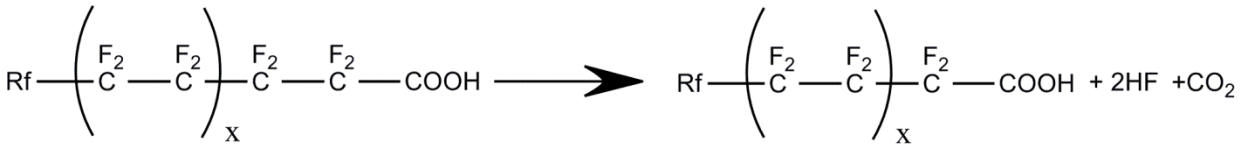

Figure 7 Main chain unzipping summary

The amount of fluoride released due to this, and other reactions, can be quantified in effluent water and is a strong indication of degradation. A rate can be calculated, which will be referred to as the fluoride emission rate (FER).

Another degradation mechanism is attack on the sulfonic acid, as shown in Figure 8. At low RH (<40%), a significant number of protons reside on the sulfonate group which can be abstracted by hydroxyl radicals. The resultant sulfonyl radical dissociates, with the release of sulfuric acid, forming a fluorocarbon radical. The side-chain undergoes a process similar to the main chain unzipping, which results in the formation of two new carboxylic acid end groups, which themselves are susceptible to radical attack. This reaction explains the observation that fluoride emission rates increase with time [30, 39, 40].

Coms also proposed the formation of sulfonyl radicals due to the hydrogen peroxide-induced cross-linking of sulfonic acid groups, which degrade in the same manner [26].

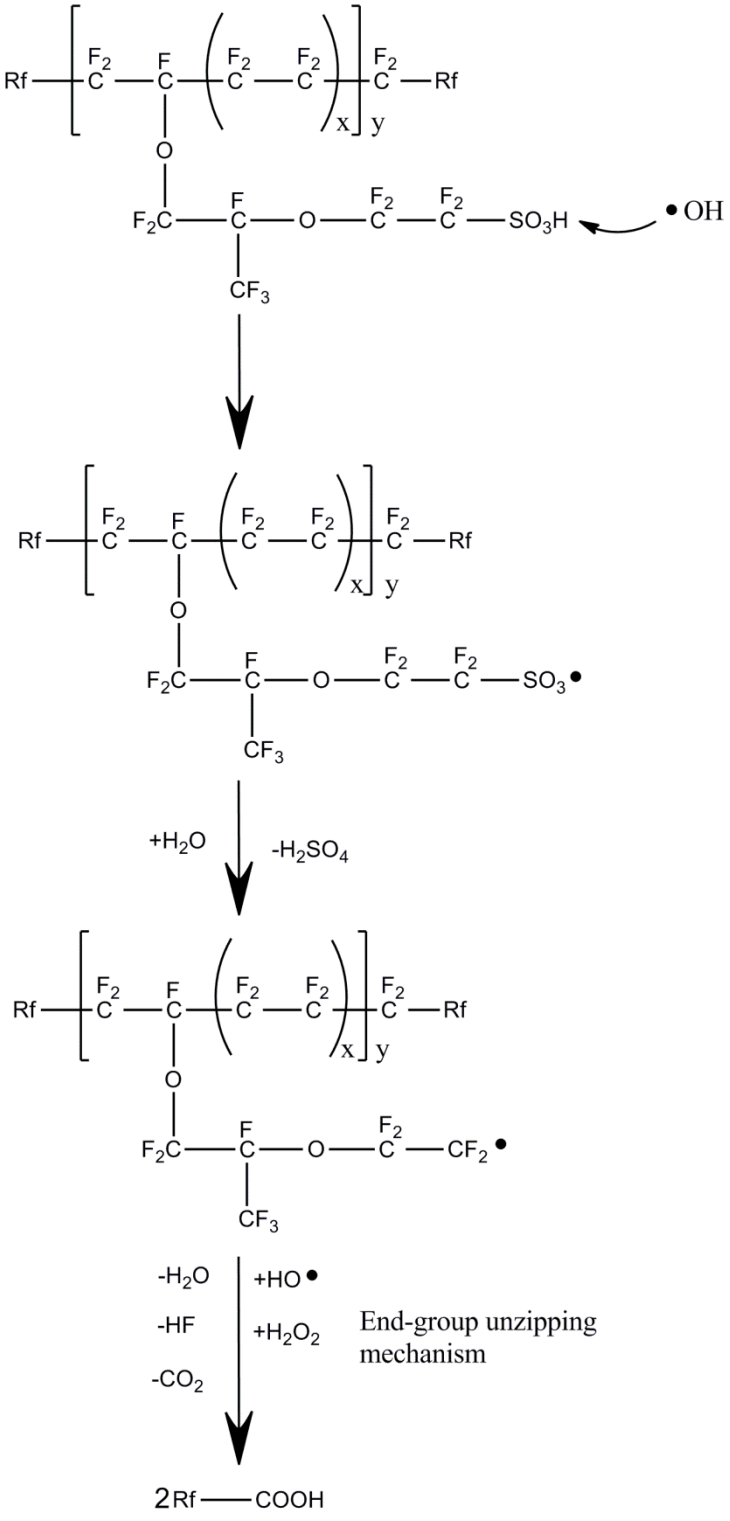

Figure 8 Sulfonate group attack (redrawn from [26])

The third degradation route was proposed by Chen and Fuller [38]. In this mechanism, shown in Figure 9, a hydroxyl radical attacks an ether-adjacent carbon, splitting off a side-chain fragment. The fluorocarbon radical degrades following the unzipping mechanism, again resulting in the formation of two COOH end groups. The side-chain fragment rearranges with the loss of HF, followed by hydrolysis to form trifluoroacetic acid (TFA) and 1,1,2,2-tetrafluoro-2-hydroxy-ethanesulfonic acid, both compounds that are susceptible to further degradation.

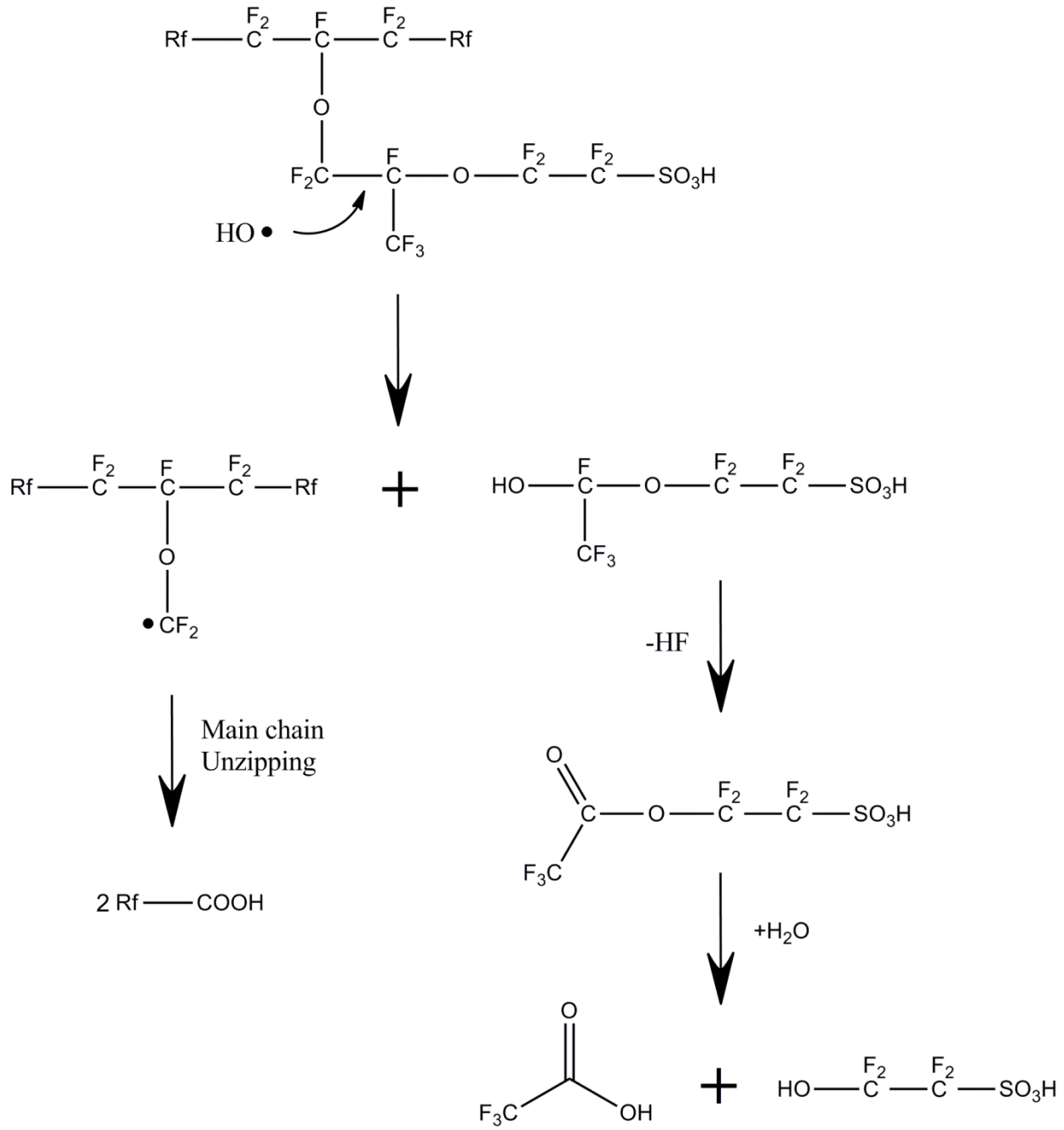

Figure 9 Ether-adjacent carbon attack (redrawn from [38])

One further reaction, that should be noted and is illustrated in Figure 10, is that during the main chain unzipping reaction, every so often a carboxylic acid adjacent to a side-chain linkage will be consumed. The backbone continues its degradation pathway but a polymer fragment, containing a carboxylic and a sulfonic acid group is split off. This fragment is susceptible to degradation again forming TFA, and 2,2-difluoro-2-sulfo-acetic acid, two compounds that can be degraded further unless removed from the system [41].

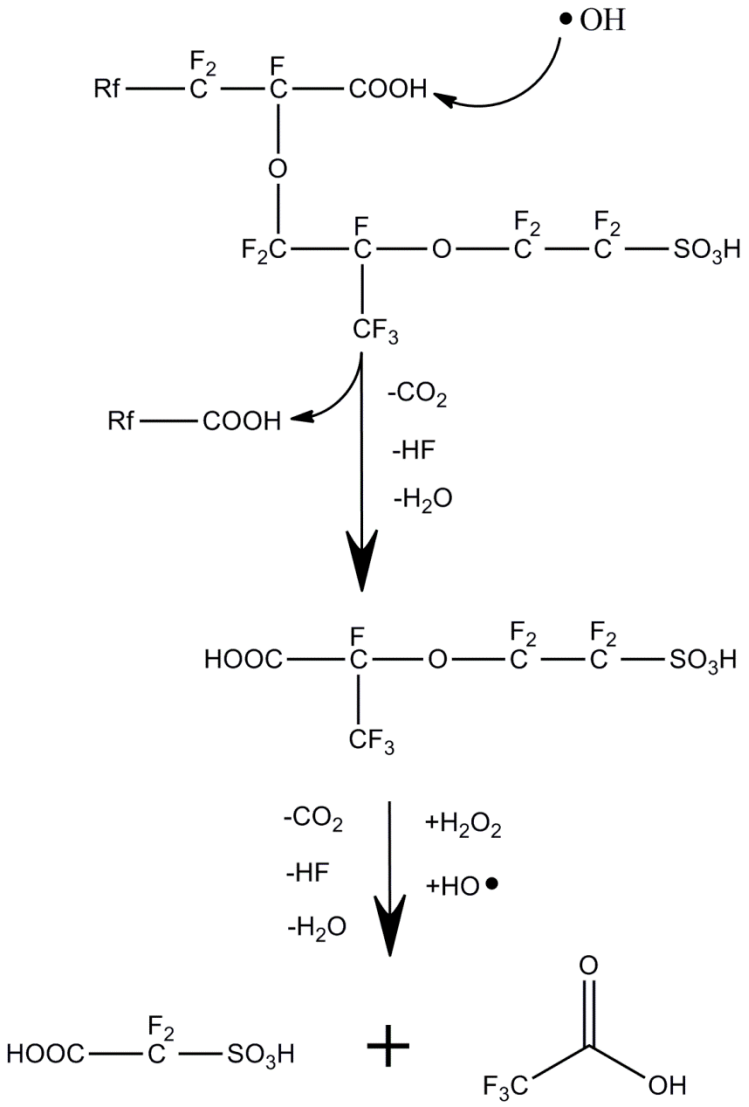

Figure 10 Secondary unzipping reaction (redrawn from [41])

The hydrogen radical formed from the abstraction of a hydrogen atom from H_2, has been proposed to attack the fluorine bonded to the carbon connected to the side-chain. This abstraction results in another pathway that leads to backbone splitting and therefore an increase in vulnerable groups [26].

From the literature review it can be concluded that the degradation of membranes is a complex mix of reactions that are dependent on conditions such as temperature, relative humidity, gas types, flow rates and pressures, membrane thickness and chemical structure, contaminants, etc. The precise origin of the reactive species has not been fully elucidated, though the consensus is that reactive oxygen radicals, mainly $HO^{\cdot}$, are the main aggressors in the degradation of PFSA polymers. This results in membrane thinning, which increases gas crossover with the possibility of shorting a cell due to direct anode-cathode contact. The loss of sulfonate groups causes a decrease in proton conductivity; all of which adds up to a loss in cell performance and efficiency. The final result of these processes is the formation of pinholes or other defects in the membrane, which ultimately lead to the catastrophic failure of the fuel cell.

1.3.7 Fenton Testing

Given the long time scales involved in determining membrane lifetime from real-world fuel cell testing (thousands of hours), accelerated test protocols have been developed to reduce the time and cost of experiments and increase the turnover rate of membrane improvements.

One simple and fast ex-situ test, that has been used as an accelerated durability test for fuel cell membranes, is the Fenton test. It involves the Fenton reaction, alluded to earlier and given in Equation 1.9. Hydrogen peroxide, in the presence of catalytic amounts of Fe^{2+} in acidic conditions forms hydroxyl radicals. The reformation of Fe^{2+}

can occur by a number of mechanisms, the main one being a reaction with H_2O_2 to form hydroperoxyl radicals, which is shown in Equation 1.10.

$$Fe^{2+} + H_2O_2 + H^+ \rightarrow Fe^{3+} + H_2O + HO\cdot \quad (1.9)$$

$$Fe^{3+} + H_2O_2 \rightarrow Fe^{2+} + HOO\cdot + H^+ \quad (1.10)$$

For durability testing, membranes are exposed to hydrogen peroxide in the presence of Fe^{2+} that has either been added to the solution or incorporated in the membranes by ion-exchange. The radicals formed in this reaction attack the membrane as described above. Degradation has been measured by membrane mass loss, FTIR and the emission of fluoride [26, 29, 34, 42-50].

1.3.8 OCV Hold Testing

A useful in-situ test method for specifically targeting membrane degradation is the open-circuit voltage (OCV) hold test. A fuel cell is exposed to hydrogen and air (or oxygen) gas flows (sometimes under pressure) at low relative humidity (<50% RH) and held at OCV. At OCV, insignificant amounts of the reactants are consumed and the gas crossover is maximized, leading to the maximum amount of radical formation [51]. Though the low relative humidity lowers the gas crossover by decreasing membrane swelling and shrinking the pathways, it exacerbates the degradation by providing more radical attack sites on the polymer side-chain [26, 38]. This method is very specific in

promoting chemical attack on the membrane while avoiding degradation due to mechanical fatigue.

1.3.9 Degradation Mitigation

Several approaches have been taken in order to improve the chemical durability of PFSAs.

1. Chemical stabilization of membranes by removing COOH end group impurities left over from polymerization by exposure to fluorine gas under high pressure [7, 25, 39, 40]
2. Fabrication of reinforced membranes by incorporation of a mechanical support such as a polytetrafluoroethylene layer [16, 19] or networks of interconnected inorganic materials [12, 17, 18, 20-22] to reduce gas crossover and improve mechanical stability [15, 17, 18, 52]
3. Use of different electrode materials, such as Pt with Cr, Co, MnO_2, TiO_2 or WO_3 to reduce the production of hydrogen peroxide [53-55]
4. Incorporation of hydrogen peroxide decomposition materials such as heteropolyacids and zirconia [19, 47, 56-58]
5. Incorporation of radical scavenging materials [20, 47, 58-69]

The latter method was investigated in this work and will be reviewed here.

1.3.10 Radical Scavenging Materials

Numerous materials, such as platinum, palladium, gold, silver, titania, silica, cerium oxide and manganese oxide nanoparticles, as well as heteropolyacids and cations, such as Ce^{3+} and Mn^{2+} are capable of mitigating the effect of radicals and many have been tested in hydrogen fuel cells. Of these, the most researched is the Ce^{3+}/Ce^{4+} redox couple.

Cerium is a member of the lanthanides that is notable for its ability to facilely switch back and forth between its +3 and +4 oxidation states. This functionality enables it to react with radicals through an easy exchange of electrons [20, 70-76].

PFSA membranes have been ion-exchanged with low levels of cerium ions and open circuit voltage hold tests have shown a decrease in the fluoride emission rate by up to three orders of magnitude over a period of 200 h versus a baseline [71]. However, the exchange of some of the protons on the sulfonate groups by Ce^{3+} ions leads to a reduction in proton conductivity and performance. Furthermore, there have been indications that ions leach from the membrane, making them inadequate for long-term use. As an alternative approach to ion exchange, addition of Ce in the form of cerium oxide (ceria) has been explored [20, 69]. As ceria, cerium retains its ability to switch oxidation states without a loss of its lattice structure [73, 74, 76, 77]. In one instance, it has been reported that PFSA membranes containing ceria nanoparticles showed a ten-fold reduction in the emission of fluoride during 24 hour OCV hold tests with no

significant impact on either performance or proton conductivity. For the given time frame, this observation was proven to be independent of ceria formulation and particle size and concentration [20]. In similar work, the OCV decay of one ceria-containing membrane was found to be small (0.1 mV h^{-1}) with little degradation over 150 h [69]. Cerium oxide, when acting as a support for a heteropolyacid hydrogen peroxide decomposition catalyst, showed improved durability enhancement. It was postulated that the H_2O_2 was first decomposed to radicals by the heteropolyacids which subsequently were scavenged by the attached cerium oxide [47].

1.4 Rationale and Objective of this Study

Some literature data are available on the behavior of ceria as a radical scavenger in accelerated durability tests. However, the majority of these experiments were short (24 hours) and limited in the parameters that were measured, yielding proof-of-concept but little information about the long-term behavior of the material. Furthermore, the chemistry of ceria in fuel cell membranes has not been elucidated. For example, it is known that ceria dissolves in concentrated sulfuric acid [78, 79] but there are no known publications on how the highly acidic environment of PFSA membranes affects this radical scavenger. The limited fuel cell data for cerium oxide as a degradation mitigation agent available in the open literature, as well as the lack of understanding of the chemical behavior of ceria in fuel cell environment, has been the driving force of this research. In this document, certain aspects of ceria chemistry and its effects on

membrane degradation using ex-situ, liquid and gas Fenton, and in-situ accelerated durability tests are presented.

1.5 References

[1] M.L. Perry, T.F. Fuller, J. Electrochem. Soc., 149 (2002) S59.

[2] S. Srinivasan, Fuel cells : From Fundamentals to Applications, 1st ed., Springer, New York, 2006.

[3] X. Li, Principles of fuel cells, Taylor & Francis, New York, 2006.

[4] C.F. Cells, in: Clean Power for Global Markets - Shareholder Update 12 July 2012, Ceramic Fuel Cells, 2012.

[5] F. Barbir, PEM fuel cells : theory and practice, Elsevier Academic Press, Amsterdam ; Boston, 2005.

[6] J.M. Anderson, in: Department of Chemistry, University of Central Florida, Orlando, FL, USA, 2012, pp. 188.

[7] H. Wang, H. Li, X.-Z. Yuan, Editors, PEM Fuel Cell Failure Mode Analysis, CRC Press, 2012.

[8] K.A. Mauritz, R.B. Moore, Chem. Rev., 104 (2004) 4535-4586.

[9] W.Y. Hsu, T.D. Gierke, Journal of Membrane Science, 13 (1983) 307-326.

[10] B. Wetton, Thermal and Electrical Coupling in Stacks, in, 2009, pp. 317-337.

[11] F.C. 2000, in, http://www.fuelcells.org/fuel-cells-and-hydrogen/benefits/, 2012.

[12] K. Wang, S. McDermid, J. Li, N. Kremliakova, P. Kozak, C. Song, Y. Tang, J. Zhang, J. Zhang, J. Power Sources, 184 (2008) 99-103.

[13] V. Ramani, H.R. Kunz, J.M. Fenton, Journal of Membrane Science, 279 (2006) 506-512.

[14] G. Alberti, M. Casciola, D. Capitani, A. Donnadio, R. Narducci, M. Pica, M. Sganappa, Electrochim. Acta, 52 (2007) 8125-8132.

[15] K.T. Park, U.H. Jung, D.W. Choi, K. Chun, H.M. Lee, S.H. Kim, J. Power Sources, 177 (2008) 247-253.

[16] M.M. Mench, E.C. Kumbur, T.N. Veziroglu, Editors, Polymer Electrolyte Fuel Cell Degradation, 1st ed., Elsevier Ltd., 2012.

[17] Y. Patil, S. Kulkarni, K.A. Mauritz, J. Appl. Polym. Sci., (2011) n/a-n/a.

[18] Y. Patil, S. Sambandam, V. Ramani, K. Mauritz, J. Electrochem. Soc., 156 (2009) B1092-B1098.

[19] T.R. Ralph, D.E. Barnwell, P.J. Bouwman, A.J. Hodgkinson, M.I. Petch, M. Pollington, J. Electrochem. Soc., 155 (2008) B411.

[20] P. Trogadas, J. Parrondo, V. Ramani, Electrochemical and Solid State Letters, 11 (2008) B113-B116.

[21] K. Mauritz, M. Hassan, Polymer Reviews, 47 (2007) 543-565.

[22] K.A. Mauritz, Mater. Sci. Eng., C, 6 (1998) 121-133.

[23] W. Yoon, in: Department of Mechanical, Materials, and Aerospace Engineering, University of Central Florida, Orlando, 2010, pp. 188.

[24] J.M. Fenton, M.P. Rodgers, D.K. Slattery, X. Huang, V.O. Mittal, L.J. Bonville, H.R. Kunz, ECS Trans., 25 (2009) 233-247.

[25] D.E. Curtin, R.D. Lousenberg, T.J. Henry, P.C. Tangeman, M.E. Tisack, J. Power Sources, 131 (2004) 41-48.

[26] F.D. Coms, ECS Trans., 16 (2008).

[27] W.K. Liu, S.J.C. Cleghorn, B.E. Delaney, M. Crum, in, John Wiley & Sons Ltd., 2009, pp. 385-402.

[28] V. Mittal, R. Kunz, J. Fenton, ECS Trans., 1 (2006) 295-301.

[29] L. Gubler, S.M. Dockheer, W.H. Koppenol, J. Electrochem. Soc., 158 (2011) B755.

[30] S.F. Burlatsky, V. Atrazhev, N. Cipollini, D. Condit, N. Erikhman, ECS Trans., 1 (2006) 239-246.

[31] V. Mittal, H.R. Kunz, J.M. Fenton, ECS Trans., 3 (2006) 507-517.

[32] V. Mittal, R. Kunz, J. Fenton, ECS Trans., 1 (2006) 275-282.

[33] V.O. Mittal, H.R. Kunz, J.M. Fenton, J. Electrochem. Soc., 154 (2007) B652-B656.

[34] V.O. Mittal, H.R. Kunz, J.M. Fenton, Electrochemical and Solid State Letters, 9 (2006) A299-A302.

[35] V.O. Mittal, H.R. Kunz, J.M. Fenton, J. Electrochem. Soc., 153 (2006) A1755-A1759.

[36] Y. Luan, Y. Zhang, in, CRC Press, 2012, pp. 73-108.

[37] W. Liu, D. Zuckerbrod, J. Electrochem. Soc., 152 (2005) A1165-A1170.

[38] C. Chen, T.F. Fuller, Polym. Degrad. Stab., 94 (2009) 1436-1447.

[39] N.E. Cipollini, Mater. Res. Soc. Symp. Proc., 885 (2006) 33-44.

[40] N.E. Cipollini, ECS Trans., 11 (2007) 1071-1082.

[41] T. Xie, C.A. Hayden, Polymer, 48 (2007) 5497-5506.

[42] W.E. Delaney, W. Liu, ECS Trans., 11 (2007) 1093-1104.

[43] S. Kundu, L.C. Simon, M.W. Fowler, Polym. Degrad. Stab., 93 (2008) 214-224.

[44] R.V. Lloyd, P.M. Hanna, R.P. Mason, Free Radical Biol. Med., 22 (1997) 885-888.

[45] T. Sugawara, N. Kawashima, T.N. Murakami, J. Power Sources, 196 (2011) 2615-2620.

[46] S. Xiao, H. Zhang, X. Li, Z. Mai, Int. J. Hydrogen Energy, 36 (2011) 10934-10939.

[47] D. Zhao, B.L. Yi, H.M. Zhang, H.M. Yu, L. Wang, Y.W. Ma, D.M. Xing, J. Power Sources, 190 (2009) 301-306.

[48] H. Liu, ECS Trans., 1 (2006) 11.

[49] S. Manatt, L., M. Manatt, R. R. , Chem.--Eur. J., 10 (2004) 6540-6557.

[50] M. Danilczuk, F.D. Coms, S. Schlick, The Journal of Physical Chemistry B, 113 (2009) 8031-8042.

[51] S. Kundu, M. Fowler, L.C. Simon, R. Abouatallah, J. Power Sources, 182 (2008) 254-258.

[52] M.A. Navarra, C. Abbati, B. Scrosati, J. Power Sources, 183 (2008) 109-113.

[53] P. Trogadas, V. Ramani, J. Power Sources, 174 (2007) 159-163.

[54] P. Trogadas, V. Ramani, J. Electrochem. Soc., 155 (2008) B696-B703.

[55] N.R. de Tacconi, C.R. Chenthamarakshan, K. Rajeshwar, W.-Y. Lin, T.F. Carlson, L. Nikiel, W.A. Wampler, S. Sambandam, V. Ramani, J. Electrochem. Soc., 155 (2008) B1102-B1109.

[56] G.M. Haugen, F. Meng, N. Aieta, J.L. Horan, M.-C. Kuo, M.H. Frey, S.J. Hamrock, A.M. Herring, ECS Trans., 3 (2006) 551-559.

[57] S. Xiao, H. Zhang, C. Bi, Y. Zhang, Y. Ma, X. Li, H. Zhong, Y. Zhang, J. Power Sources, 195 (2010) 8000-8005.

[58] M. Aoki, H. Uchida, M. Watanabe, Electrochem. Commun., 7 (2005) 1434-1438.

[59] V. Ramani, P. Trogadas, S. Sambandam, Abstracts of Papers, 238th ACS National Meeting, Washington, DC, United States, August 16-20, 2009, (2009) FUEL-183.

[60] P. Trogadas, in: Department of Chemical and Biological Engineering, Illinois Institute of Technology, Illinois, 2009.

[61] P. Trogadas, J. Parrondo, F. Mijangos, V. Ramani, J. Mater. Chem., 21 (2011) 19381.

[62] P. Trogadas, J. Parrondo, V. Ramani, Abstracts of Papers, 238th ACS National Meeting, Washington, DC, United States, August 16-20, 2009, (2009) PMSE-100.

[63] P. Trogadas, J. Parrondo, V. Ramani, Degradation Mitigation in PEM Fuel Cells Using Metal Nanoparticle and Metal Oxide Additives, in: Functional Polymer Nanocomposites for Energy Storage and Conversion, American Chemical Society, 2010, pp. 187-207.

[64] P. Trogadas, J. Parrondo, V. Ramani, PMSE Preprints, 100 (2009) 459-460.

[65] P. Trogadas, J. Parrondo, V. Ramani, Chem. Commun., 47 (2011) 11549.

[66] P. Trogadas, V. Ramani, ECS Trans., 25 (2009) 443-451.

[67] P. Trogadas, V.K. Ramani, PMSE Preprints, (2010).

[68] E. Endoh, ECS Trans., 16 (2008) 1229-1240.

[69] S. Xiao, H. Zhang, C. Bi, Y. Zhang, Y. Zhang, H. Dai, Z. Mai, X. Li, J. Power Sources, 195 (2010) 5305-5311.

[70] A. Trovarelli, Catalysis by ceria and related materials, Imperial College Press, London, 2002.

[71] F.D. Coms, H. Liu, J.E. Owejan, ECS Trans., 16 (2008) 1735-1747.

[72] A. Karakoti, in: Mechanical, Materials and Aerospace Engineering University of Central Florida Orlando, 2010.

[73] A. Karakoti, S. Singh, J.M. Dowding, S. Seal, W.T. Self, Chem. Soc. Rev., 39 (2010) 4422-4432.

[74] A.S. Karakoti, N.A. Monteiro-Riviere, R. Aggarwal, J.P. Davis, R.J. Narayan, W.T. Self, J. McGinnis, S. Seal, JOM, 60 (2008) 33-37.

[75] A.S. Karakoti, S. Singh, A. Kumar, M. Malinska, S.V.N.T. Kuchibhatla, K. Wozniak, W.T. Self, S. Seal, J. Am. Chem. Soc., 131 (2009) 14144-14145.

[76] T. Pirmohamed, J.M. Dowding, S. Singh, B. Wasserman, E. Heckert, A.S. Karakoti, J.E.S. King, S. Seal, W.T. Self, Chem. Commun., 46 (2010) 2736-2738.

[77] J.M. Anderson, J. Patel, A.S. Karakoti, N. Greeneltch, D.J. Díaz, S. Seal, Electrochim. Acta, 56 (2011) 2541-2545.

[78] N. Um, M. Miyake, T. Hirato, Zero-Carbon Energy Kyoto, (2011) 165-170.

[79] R.A. Day, Jr., A.L. Underwood, Quantitative Analysis. 5th Ed, Prentice-Hall, Inc., 1986.

CHAPTER 2: EXPERIMENTAL

2.1 Synthesis of Nanoparticulate Cerium Oxide

Nanoparticulate ceria was prepared by thermal hydrolysis. Ammonium hydroxide, 0.50 ml (Fisher Scientific; 29.04%), was added to 50 ml of a boiling solution of 0.02 M ammonium cerium(IV) nitrate (Acros Organics; 99.5% for analysis) in ethanol (Decon Labs; 200 proof) which, after the addition, was left to cool overnight under constant stirring. The yellow precipitate of cerium oxide that formed was centrifuged, washed five times with 5 ml of ethanol and then dried at 100 °C under vacuum, yielding ca. 0.17 g of product (90 – 95% yield).

2.2 Preparation of Ceria Dispersions

The synthesized ceria was dispersed in ethanol in a Branson 2510 ultrasound bath using sonication at 40 kHz to give 7 mM colloidal dispersions in ethanol. Using the same technique, 7 mM dispersions of a commercial cerium oxide powder (Alfa Aesar; 99.9% min (REO)) in ethanol were also prepared.

2.3 Membrane Casting

PFSA membranes were cast in a humidity controlled environment (<30% RH) onto a porous PTFE support (Donaldson Filtration Solution; Tetratex® membrane; 7 μm) from mixtures of 5% 1100 EW PFSA dispersions in alcohols (Ion Power, Inc.), ethanol and

dimethylformamide (Acros Organics; 99.5% for HPLC) in a 5.8 : 4.0 : 1.0 volume ratio. Ceria was incorporated by replacing some of the ethanol with appropriate amounts of the ceria dispersions to yield membranes with 0.5, 1.0 and 2.0 weight percent of cerium oxide relative to the polymer mass. Membranes without ceria were also cast as baselines. After room temperature drying, membranes were heated at 150 °C for three hours under vacuum after purging three times with nitrogen gas (Airgas; UHP) to remove residual solvent.

2.4 Membrane Electrode Assembly Fabrication

Membranes were coated with a catalyst by a spraying method.

2.4.1 Catalyst Ink Preparation

The catalyst ink was prepared by mixing 720 ± 1 mg of Pt on carbon catalyst (Tanaka; 46.7% Pt on C) with 3.158 ± 0.1 g of water, 20 ± 0.3 g of methanol (Acros Organics; 99.9% for HPLC) and 6.78 ± 0.08 g of 5% 1100 EW Nafion® dispersion. This mixture was homogenized with an Omni International GLH-01 homogenizer at 18800 rpm for 6 ± 0.5 hours in an ice-bath. The suspension was then weighed, stored under continuous stirring at 750 rpm and used within one week.

2.4.2 Catalyst Spraying

The setup for the catalyst spraying is shown in Figure 11. Two membranes were taped side by side between two polypropylene die-cut sheets and mounted on a metal frame. Two smaller metal frames were screwed onto either side of the membranes to hold them in place. The whole setup was mounted in a nitrogen ventilated enclosure in front of a 100 °C heated plate. The catalyst was applied using a nitrogen gas flow-controlled Badger Model 150 artist's spray gun mounted on a computer-controlled track. The membrane was covered with a 25 cm^2 area of catalyst in an A-B-A-B pattern and loadings were kept at gravimetrically determined 0.375 ± 0.025 gPt cm^{-2}. The resulting product is referred to as a catalyst coated membrane (CCM).

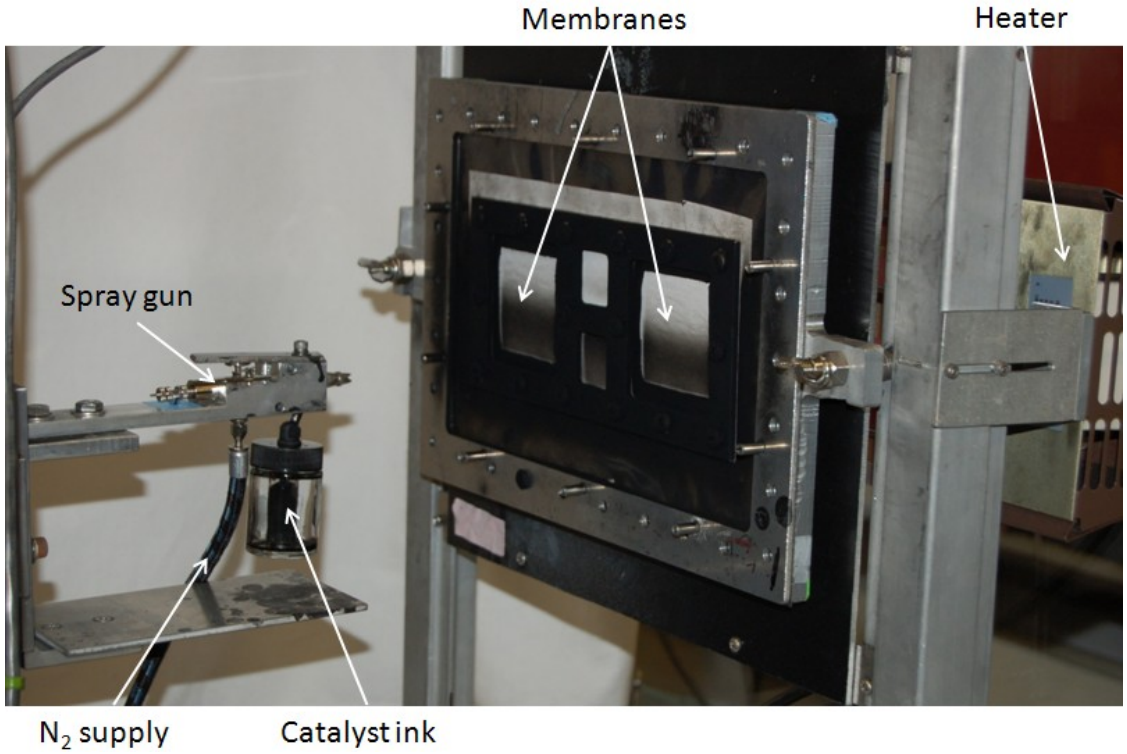

Figure 11 Catalyst coated membrane spraying setup

2.4.3 CCM Preparation

To prevent sulfonate group decomposition during the following thermal treatment, the CCMs were ion-exchanged with Cs^+ by immersion in 200 ml of a 0.05 M cesium carbonate solution (Alfa Aesar; 99% (metals basis)) overnight. Soaking in water for 30 min removed excess ions which was followed by drying at 100 °C for 10 min and then a hot press between two PTFE sheets between two graphite plates at 180 °C at 75 psi for 30 min. Hot-pressing allows polymer chains to move and align themselves into an optimal structure.

Reprotonation of the sulfonate groups was achieved by immersion in 0.5 M sulfuric acid (BDH; 98.0%) at 60 °C for three hours, followed by washing in water at 60 °C for one hour and drying at 70 °C for two hours.

2.4.4 Gas Diffusion Layers

A gas-diffusion layer was used to evenly distribute the reactant gases across the CCM. The Gurley number is a measure of a gas diffusion media's ability to let gases flow through it [1]. It was measured using the setup presented in Figure 12. A GDL was cut from Ion Power, Inc., Sigracet 10BC sheets and built into the cell assembly with seven PTFE gaskets on each side. As shown in the schematic in Figure 12, the gas flow through the GDL was measured at 0.05, 0.1, 0.15 and 0.2 in H_2O pressure differentials (measured on the slant pressure gauge) and the Gurley number was calculated from

Equation 2.1. Only GDLs with Gurley numbers greater than 20 dm^3 min^{-1} cm H_2O^{-1} cm^{-2} were used.

$$GN = \frac{gas\ flow\ rate}{\Delta p \times 2.54 \times active\ area} \qquad (2.1)$$

Where Δp is the pressure difference, 2.54 is the conversion factor from in H_2O to cm H_2O and the active area is 33.6 cm^2 (5.8 x 5.8 cm^2).

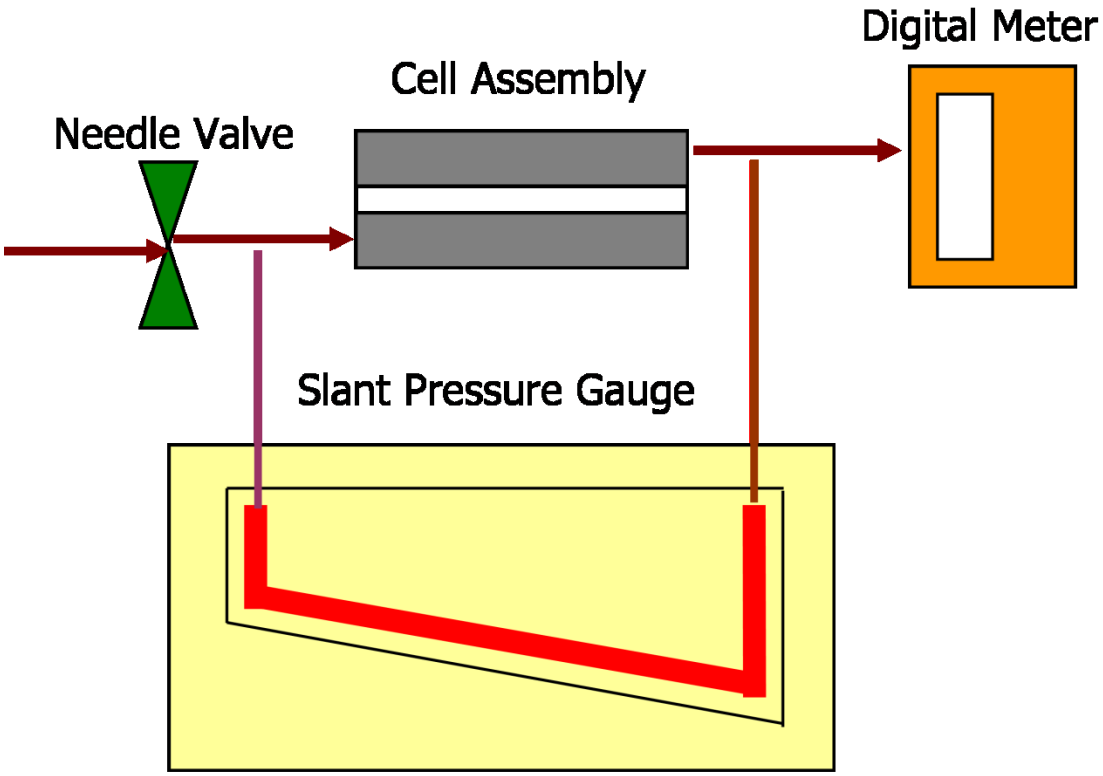

Figure 12 Gurley number measurement schematic

2.5 Cell Building

Figure 13 shows a schematic of a cell build. A GDL was placed on each electrode of the CCM yielding a membrane electrode assembly (MEA). The thicknesses of the CCM and the GDLs were measured using a micrometer (Mitutoyo; Absolute Series 547). The amount of pressure applied to the MEA, referred to as "pinch" and measured in micrometers, was calculated from Equation 2.2.

$$cell\ pinch = \ CCM\ thickness + GDL\ thicknesses\ - gasket\ thickness \quad (2.2)$$

PTFE gaskets were chosen so their measured thicknesses yielded a pinch between 9 and 10 μm. The MEA and gaskets were sandwiched between two graphite bipolar plates with gas flow fields that themselves were each covered by a conductive metal plate with end plates providing the backing support for screws (Fuel Cell Technologies; 25 cm^2 hardware). Eight cell screws were incrementally tightened: first 20, then 30 and finally 40 inch pounds to apply adequate pressure to the system. Images of the cell build are shown in Figure 14.

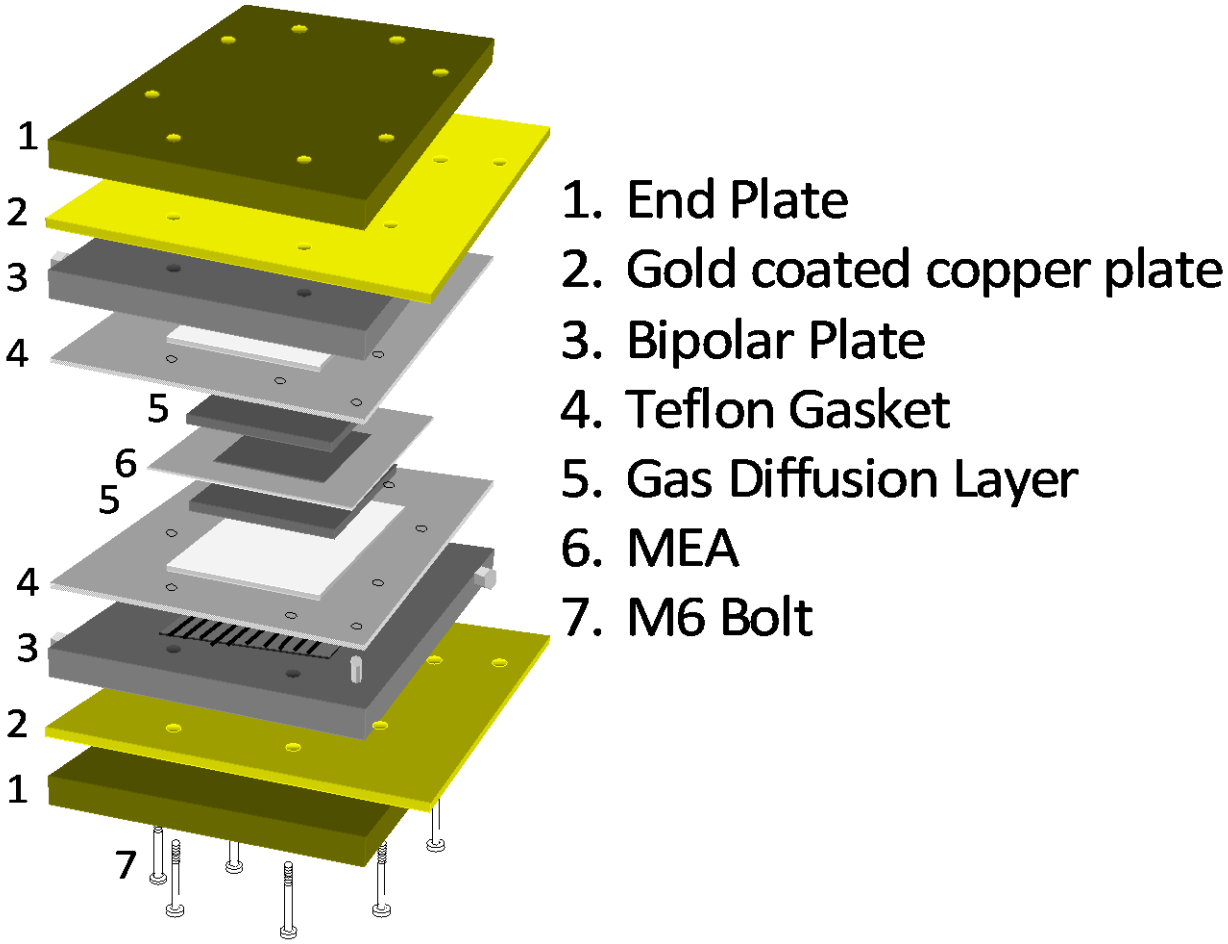

Figure 13 Schematic of cell build

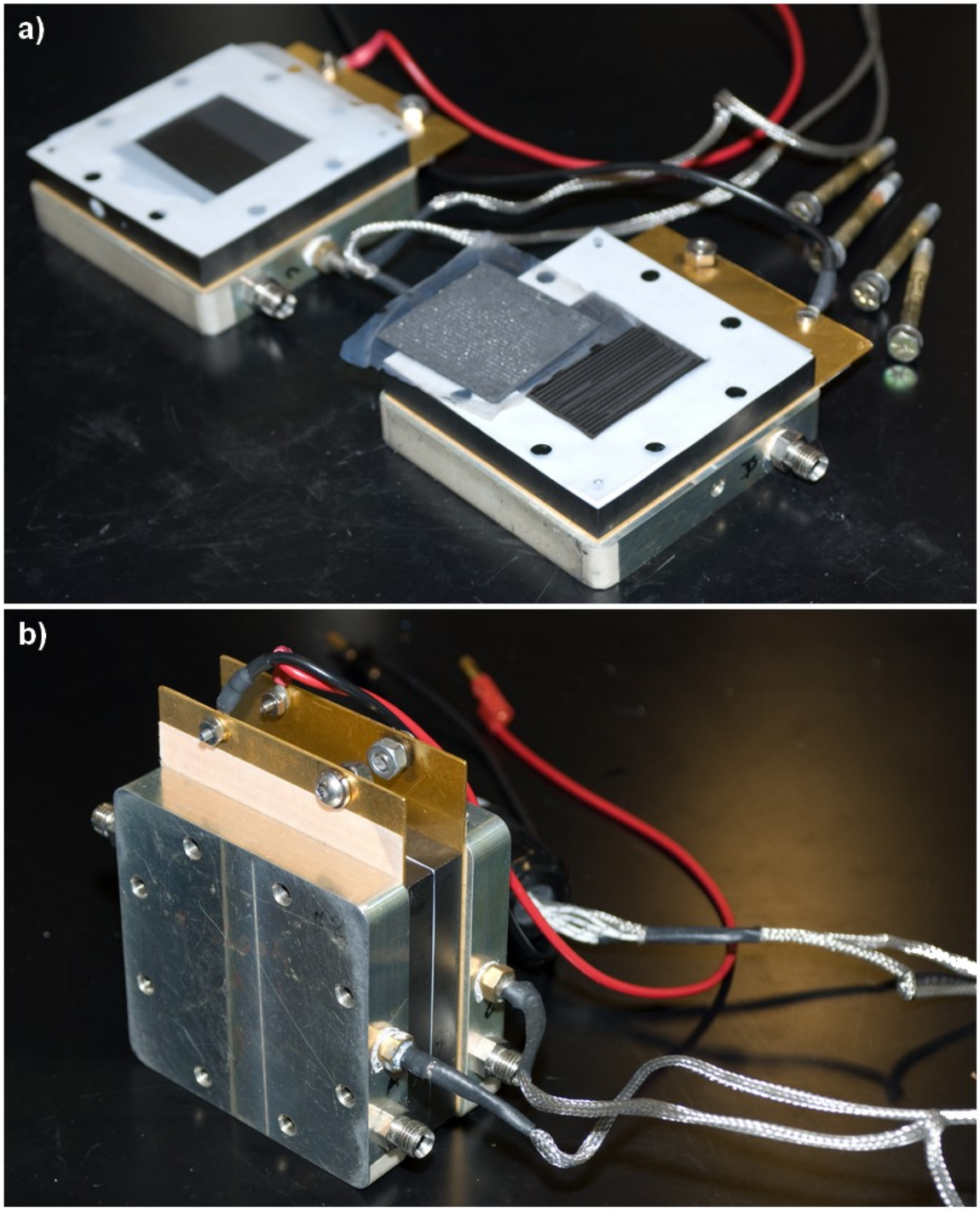

Figure 14 Images of cell building: a) cathode (left) and anode (right) assembled end plate, copper plate, graphite flow field and Teflon gaskets with MEA placed on anode section; and b) built cell

2.6 Electron Microscopy

Electron imaging was performed on several instruments:

- Hitachi TM3000 scanning electron microscope (SEM) with integrated Physical Electronics 5400 energy dispersive x-ray spectroscopy (EDS) detector
- Zeiss ULTRA-55 FEG SEM
- JEOL 1100 transmission electron microscope (TEM)
- JEOL 2200FS TEM/scanning transmission electron microscope (STEM) equipped with a Bruker Quantax EDS detector

For TEM imaging, ceria powders were supported on a copper grid with a Holey carbon film (Electron Microscopy Sciences; 200 mesh). For STEM with EDS measurements, ceria powders were supported on copper grids with Lacey carbon films. Electron diffraction patterns were recorded in a Tecnai F20 TEM operated in nanoprobe mode. Calculated d-spacings were obtained using the online WebEMAPS software [2].

For SEM imaging of cross-sections, membranes and CCMs were embedded in resin (Struers; SpeciFix® Resin), polished and sputter-coated with gold. For TEM and STEM imaging of cross-sections, membranes and CCMs were embedded in Araldite 502 resin (Electron Microscopy Sciences) and cut using diamond-knife ultramicrotomy.

Platinum particle counting on TEM and STEM images was performed using the ImageJ software package [3].

2.7 X-Ray Diffraction

X-ray diffraction (XRD) measurements of the nanoparticles were performed on a Rigaku D/Max-B diffractometer using a Cu X-ray source with 2θ values from 20 to 80°. Spectra processing was performed using the MDI Jade software package.

2.8 X-Ray Photoelectron Spectroscopy

X-ray photoelectron spectroscopy (XPS) measurements of the ceria nanoparticles were performed on a Thermo Scientific K-Alpha instrument (Al-K_α monochromatic X-rays charge compensated with low energy electrons and Ar-ions; Pass Energy 50 eV) with dry powder supported on glass.

Deconvolution of the obtained Ce3d5 peaks was performed following literature procedures [4-6] with the AugerScan software package.

2.9 UV/Vis Spectroscopy

Transmission UV/Vis spectra were obtained on a Shimadzu UV-2401PC for both liquids and solids.

2.10 NMR Spectroscopy

^{19}F-NMR measurements in water with a D_2O lock were performed on a Varian VNMRS 500M Hz instrument.

2.11 Mass Spectroscopy

Mass spectrometry of solids was performed on a PerkinElmer Diamond TG/DTA connected to a Pfeiffer GSD301 T2 mass spectrometer.

Mass spectroscopy of liquids and gases was performed on an Agilent Technologies 6890N gas chromatograph connected to a JEOL MS-BU25 mass spectrometer and on a JEOL AccuTOF-DART mass spectrometer.

2.12 Proton Conductivity

The resistance of membranes was measured using a Princeton Applied Research Potentiostat/Galvanostat Model 263A by performing cyclic voltammetry from -0.3 to 0.3 V at a scan rate of 30 mV s^{-1} on a piece of membrane under a 1000 cm^3 min^{-1} hydrogen gas flow (Airgas, Inc.; UHP) at 80 °C in a 4-probe BekkTech conductivity cell, which is shown in Figure 15. The relative humidity of the gas stream was varied from 20 – 90% and the in-plane conductivity of the membrane was calculated based on the membrane dimensions, as given in Equation 2.3.

$$\sigma = \frac{l}{Rwt} \qquad (2.3)$$

Where σ is the conductivity, l is the distance between V1 and V2 (Figure 15) (0.425 cm), R is the measured resistance, w is the width of the membrane piece (0.5 cm) and t is the measured thickness of the membrane piece (~0.0025 cm).

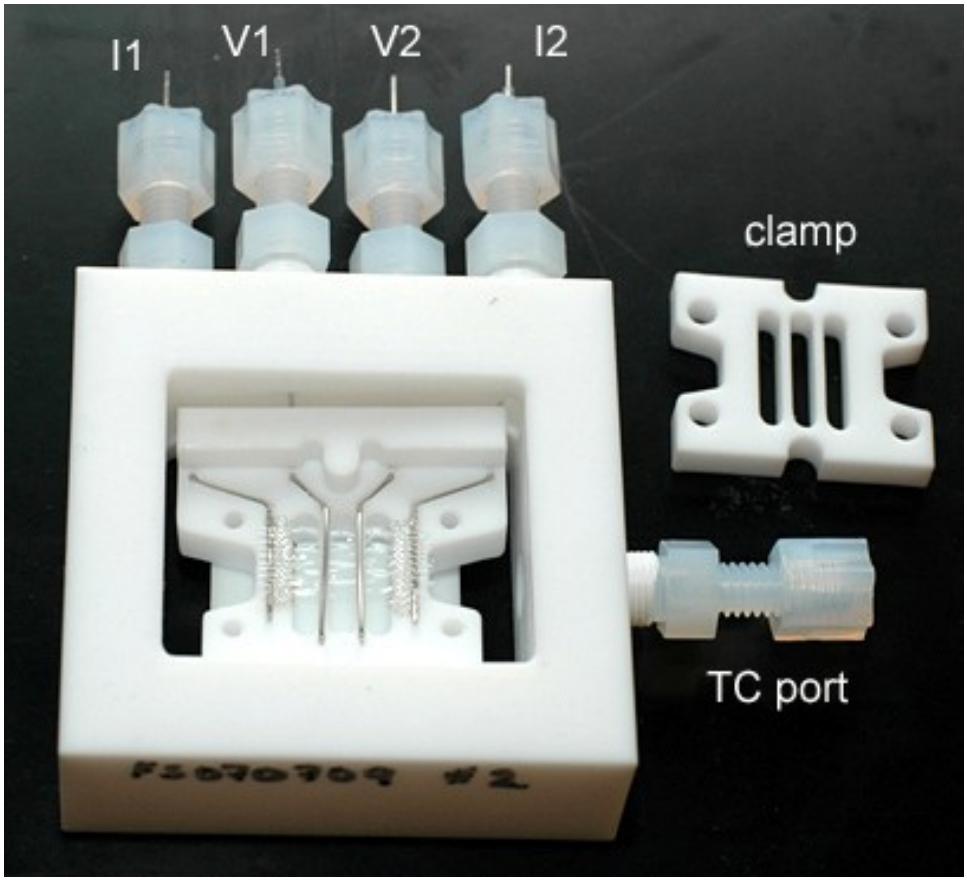

Figure 15 Bekktech 4-probe conductivity cell (I1 – counter, V1 – reference, V2 – sense, and I2 – working electrode; TC - thermocouple)

2.13 Fenton Testing

2.13.1 Membrane Preparation

Membranes were treated in the same manner as described in section "2.4.3: CCM Preparation" prior to use in any experiments.

2.13.2 Fe^{2+} Ion-Exchange

Prepared membranes were ion-exchanged with Fe^{2+} ions. First, they were dried at 100 °C under vacuum for one hour and then weighed immediately. The dry weight was used to calculate the number of protons in the membrane based on their equivalent weight of 1100 g eq^{-1}. The membranes were then immersed in 200 ml of a solution of $FeSO_4 \cdot 7H_2O$ (Acros Organics; 99.5% for analysis) in a mole ratio of 10 : 1 of H^+ to Fe^{2+}.

2.13.3 Fe^{2+} Uptake Determination

To determine the amount of Fe^{2+} ions exchanged, a UV/Vis spectroscopic method was used [7]. Pieces of membrane were dried at 100 °C under vacuum for one hour, weighed and then immersed in 25 ml of a 1 M potassium chloride (Acros Organics; ACS grade) solution overnight to dissolve all iron ions into the water. After removing the membrane, one ml of a 1.43 M solution of hydroxylamine hydrochloride (Alfa Aesar; 99%) to reduce any Fe^{3+} to Fe^{2+}, 10 ml of a 5.6 mM solution of 1,10-phenanthroline (Fisher Scientific; certified ACS) as the Fe(II) complexing agent and eight ml of a 0.735 M buffer solution of sodium acetate (Fisher Scientific; certified ACS) were added and made up to 100 ml with water. The absorbance at 508 nm was measured on the UV/Vis spectrometer and the concentration of Fe^{2+} calculated from a calibration curve prepared from $FeSO_4$ standards.

2.13.4 Liquid Fenton Test

A schematic for the liquid Fenton test setup is shown in Figure 16. Fe^{2+} ion-exchanged membranes were immersed in 3.0% hydrogen peroxide solutions (VWR; ACS Grade; 30%) under reflux conditions at 80 °C for 48 hours. After 24 hours, using test strips (EMD Chemicals; 100 – 1000 mg l^{-1} H_2O_2), the hydrogen peroxide was found to be completely decomposed and the solution was replaced. Three membranes were measured simultaneously.

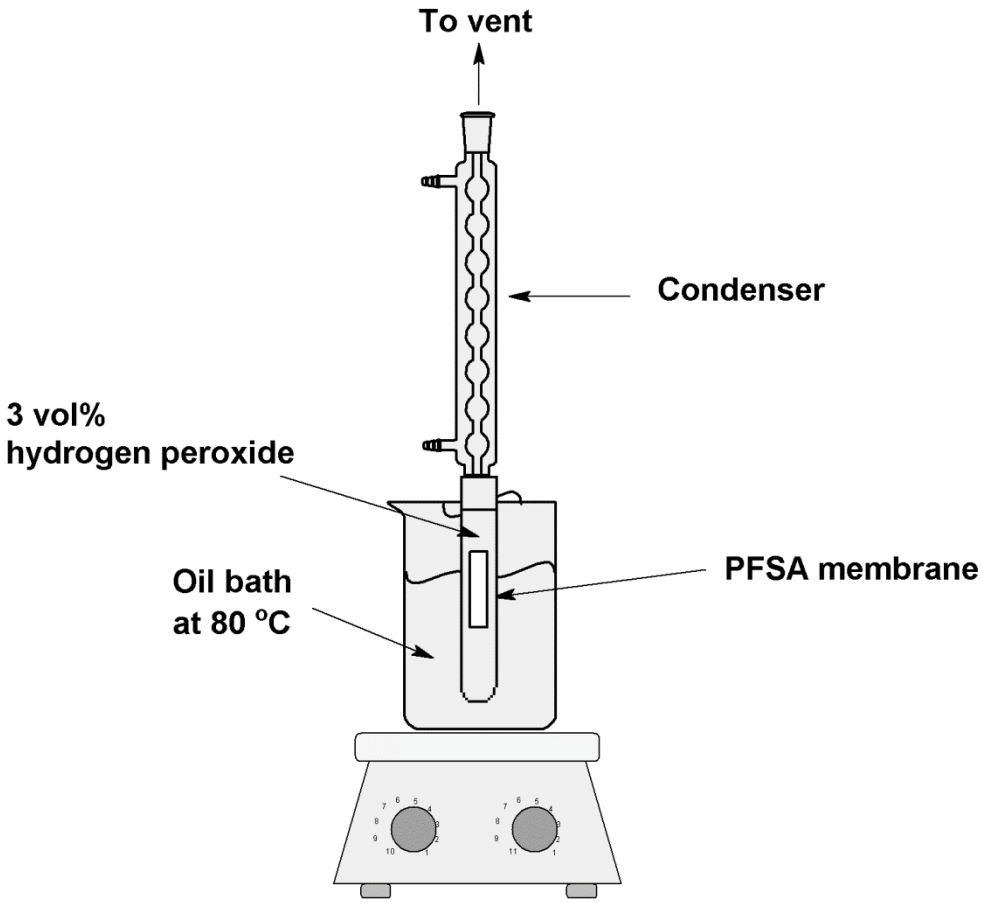

Figure 16 Liquid Fenton test setup schematic

2.13.5 Gas Fenton Test

A schematic for the gas Fenton test setup is shown in Figure 17. It was modeled on a test setup devised by Hommura *et al.* [8] and Endoh *et al.* [9]. Fe^{2+} ion-exchanged membranes, in an 80 °C reaction chamber, were exposed to a 50 cm^3 min^{-1} flow of nitrogen gas (Airgas, Inc.; UHP) that was previously bubbled through a 60 °C solution of 30% hydrogen peroxide. The degradation products were trapped by passing the exit gases through a potassium hydroxide solution (VWR; 0.1 M; Baker Analyzed).

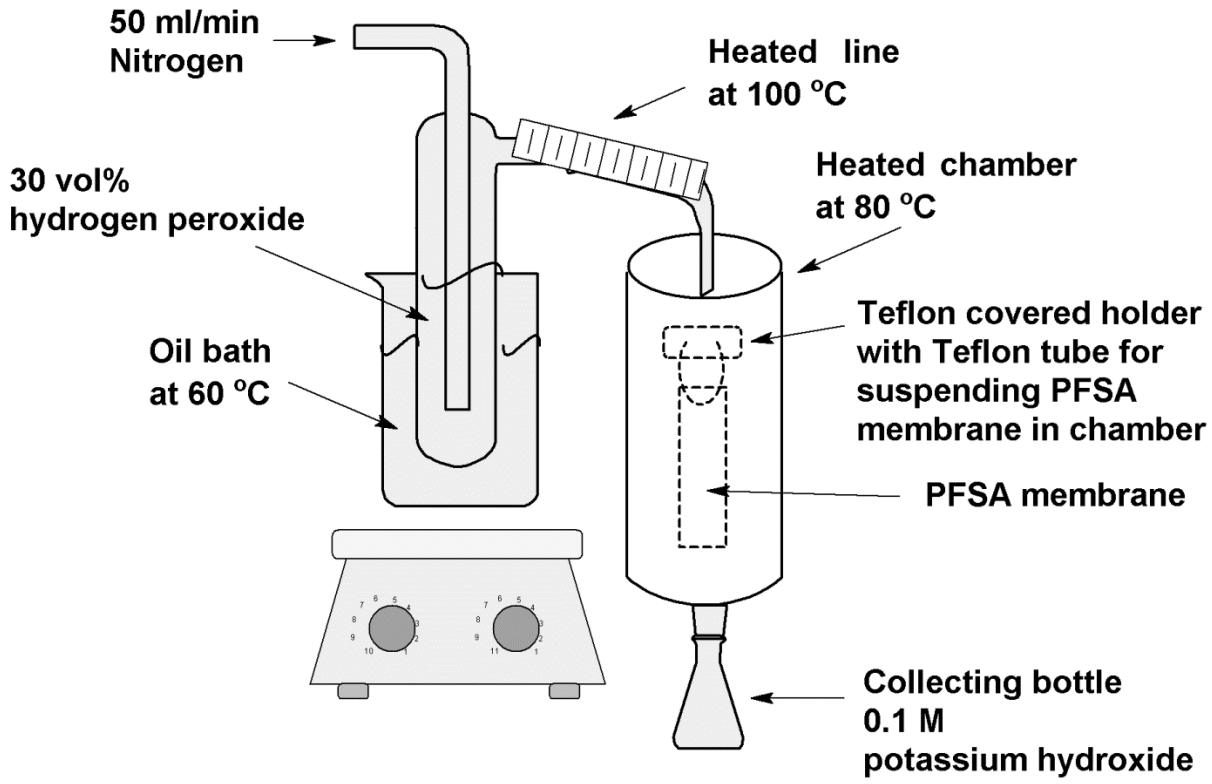

Figure 17 Gas Fenton test setup schematic

2.14 94 h OCV Hold Test

Two OCV hold experiments were executed, one for 94 hours and the other for 500 hours. Though both tests were similar, conditions and measurements varied enough to warrant description under separate headings. The following section describes the 94 hour OCV hold experiment.

2.14.1 General Equipment

Linear sweep voltammetry and cyclic voltammetry were performed using a Princeton Applied Research Potentiostat/Galvanostat Model 263A.

Gas flows and applied potentials and currents were controlled by a Scribner Associates, Inc. 850C or a Teledyne Energy Systems, Inc. Medusa fuel cell test station.

The Scribner, Inc. CorrWare, CorrView and FuelCell software packages were used for electrochemical and fuel cell experiments and for data analysis.

2.14.2 Cell Integrity Determination

Built cells were tested for internal and external leaks and overall cell resistance at room temperature, to verify their basic integrity.

For the internal leak test, nitrogen gas at a pressure of 3 psi was applied to the cathode side and the gas flow on the anode was measured. Only cells with no measurable internal leaks were used.

For external leak tests, nitrogen gas at a pressure of 3 psi was applied to the capped cell. The gas flow was shut of and the time taken for the pressure to drop from 3 to 2 psi was measured. Only cells that took longer than 10 seconds to lose 1 psi of pressure were used.

Only cells that showed resistances greater than 60 Ω, as measured using a multimeter, were used.

2.14.3 Hydrogen Crossover and Electrochemically Active Area Measurement

Linear sweep voltammetry from 0.1 to 0.8 V at a scan rate of 4 mV s^{-1} was performed at 25/25/25 (cell temperature/anode humidifier temperature/cathode humidifier temperature) with flow rates of 170 cm^3 min^{-1} of H_2/N_2 (anode gas/cathode gas). The hydrogen crossover was determined from the current density at 0.5 V.

Cyclic voltammetry was performed between 0.025 and 0.8 V at a scan rate of 30 mV s^{-1} for five cycles at 25/25/25 with flow rates of 170 cm^3 min^{-1} of H_2/N_2. The electrochemically active area (ECA) of the platinum catalyst was calculated from the hydrogen adsorption area during the cathodic sweep.

Hydrogen crossover and ECA were determined before and after OCV hold testing.

2.14.4 Humidification and Break-In

Humidification of the MEAs was achieved by exposing the cell to 170 cm^3 min^{-1} of H_2/N_2 at 80/80/73 for three hours.

The MEAs were broken in by operating under benign fuel cell conditions. The cells were exposed to H_2/Air at 80/80/73 with the potential set at 0.55 V. Below 200 mA cm^{-2} gas flow rates were set at 170 cm^3 min^{-1}, but above that current density the flow rates were adapted to provide for 30% and 25% utilization at the anode and cathode, respectively. The cells were considered ready when the current changed less than 5% per hour.

2.14.5 Performance Measurements

The performance of cells was measured by exposing membranes to H_2/Oxidant at 80/80/73. Below 200 mA cm^{-2} gas flow rates were set at 170 cm^3 min^{-1}, but above that current density the flow rates were adapted to provide for 30% and 25% utilization at the anode and cathode, respectively. Increasing loads were applied: 0, 10, 20, 40, 60, 80, 100, 200, 300, 400, 500, 600, 700, 800, 900, 1000, 1100, 1200, 1300, 1400, 1500, 1600, 1700, 1800, 1900 and 2000 mA cm^{-2}. The potential after 5 min of equilibration was measured and plotted as function of current density. Performance was first measured with H_2/Air, then H_2/O_2, and finally with H_2/Air, before and after OCV hold testing.

2.14.6 OCV Hold Testing

Cells were exposed to open circuit voltage conditions at 90/63/63 with 200 cm^3 min^{-1} of H_2/Air for 94 hours on a Scribner Associates, Inc. MEADS Model 755 membrane electrode assemble durability test system. The potential was monitored during the course of the experiment and condensed water samples were taken twice a day. The cells tested are listed in Table 2. The test conditions are summarized in Table 3.

Table 2 Cells used in the 94 hour OCV hold test

MEA	Ceria	# of cells
Baseline	None	3
Synthesized Ceria	0.5 wt%	2
Synthesized Ceria	1.0 wt%	2
Synthesized Ceria	2.0 wt%	2
Commercial Ceria	0.5 wt%	2
Commercial Ceria	1.0 wt%	2
Commercial Ceria	2.0 wt%	2

Table 3 Summary of OCV hold test conditions.

	Type	Flow	RH	Pressure
94 h OCV hold Anode fuel	H_2	200 cm^3 min^{-1}	30%	Ambient
94 h OCV hold Cathode fuel	Air	200 cm^3 min^{-1}	30%	Ambient
500 h OCV hold Anode fuel	H_2	350 cm^3 min^{-1}	30%	150 kPa
500 h OCV hold Cathode fuel	Air	830 cm^3 min^{-1}	30%	150 kPa

2.15 500 h OCV Hold Test

The following section describes the 500 hour OCV hold experiment.

2.15.1 General Equipment

Linear sweep voltammetry and cyclic voltammetry were performed using a Princeton Applied Research Potentiostat/Galvanostat Model 263A.

Gas flows and applied potentials and currents were controlled by a Scribner Associates, Inc. 850C fuel cell test station.

The Scribner, Inc. CorrWare, CorrView and FuelCell software packages were used for electrochemical and fuel cell experiments and data analysis.

2.15.2 Cell Integrity Determination

Internal and external leak tests and cell resistance measurements were performed in the same manner as for the 94 h OCV hold test (see section "2.14.2: Cell Integrity Determination").

2.15.3 Hydrogen Crossover, Electrochemically Active Area, Cell Resistance and High Frequency Resistance Measurements

Linear sweep voltammetry from 0.1 to 0.4 V was performed at a scan rate of 2 mV s^{-1}. Before and after the 500 h OCV hold test measurements were performed at 25/25/25 with flow rates of 500 cm^3 min^{-1} of H_2/N_2. During the 500 h OCV hold test measurements were performed at 90/61/61 with anode flow rates of 350 cm^3 min^{-1} of H_2 and cathode flow rates of 830 cm^3 min^{-1} of N_2. The hydrogen crossover was determined from the current density at 0.4 V.

The resistance and high frequency resistance were measured every 24 h during the 500 h OCV hold in order to determine the occurrence of shorts. For resistance, 0.5 V were applied for 5 min at 90/61/61 with anode flow rates of 350 cm^3 min^{-1} of N_2 and cathode flow rates of 830 cm^3 min^{-1} of N_2. The resistance was calculated from the average current of the last 10 s with a target of over 1000 ohm cm^2. For the high frequency resistance, 0.2 mA cm^2 were applied at 90/61/61 with anode flow rates of 350 cm^3 min^{-1} of H_2 and cathode flow rates of 830 cm^3 min^{-1} of air and the value for the HFR was noted after 30 s from the FuelCell software.

Cyclic voltammetry was performed between 0.025 and 0.8 V at a scan rate of 30 mV s^{-1} for five cycles at 25/25/25 with flow rates of 500 cm^3 min^{-1} of H_2/N_2. The ECA of the platinum catalyst was calculated from the hydrogen adsorption area during the cathodic sweep.

2.15.4 Humidification and Break-In

Humidification and break-in were performed in the same manner as for the 94 h OCV hold test (see section "2.14.4: Humidification and Break-In").

2.15.5 Performance Measurements

Performance measurements were performed in the same manner as for the 94 h OCV hold test (see section "2.14.5: Performance Measurements").

2.15.6 OCV Hold Testing

Cells were exposed to open circuit voltage conditions at 90/61/61 with 350 cm^3 min^{-1} of H_2 and 830 cm^3 min^{-1} of Air and 150 kPa of pressure for 500 hours on a Scribner Associates, Inc. 850C fuel cell test system. The potential was monitored throughout the duration of the experiment and condensed water samples were taken once a day. The cells tested are listed in Table 4. The test conditions are summarized in Table 3.

Table 4 Cells used in the 500 hour OCV hold test

MEA	Ceria	# of cells
Baseline	None	1
Synthesized Ceria	1.0 wt%	1
Commercial Ceria	1.0 wt%	1

2.16 Ion Chromatography

Ionic compounds of eluents from accelerated durability tests were measured by ion chromatography on a Dionex ICS-1500 equipped with an AS9-HC carbonate eluent anion-exchange column. Fluoride concentrations were calculated from 0.5, 1.0, 10 and 100 ppm F^- standards (VWR; 100 ppm fluoride in water).

2.17 Infrared Imaging of Hydrogen Crossover

Infrared (IR) images of tested MEAs were obtained using a Fluke Ti25 IR camera. The MEAs with gaskets were placed on a graphite plate and secured so that the cathode side was visible and exposed to air. A mixture of 4% hydrogen in nitrogen gas was allowed to flow on the anode side and IR images were recorded. Hydrogen gas that penetrated the membrane reacted with oxygen at the cathode and the resultant exothermic reactions appeared on IR images as areas of elevated temperature.

2.18 References

[1] F. Barbir, PEM fuel cells : theory and practice, Elsevier Academic Press, Amsterdam ; Boston, 2005.

[2] J.M. Zuo, J.C. Mabon, in, http://emaps.mrl.uiuc.edu/, 2004.

[3] W.S. Rasband, in, http://imagej.nih.gov/ij/, U. S. National Institutes of Health, Bethesda, Maryland, USA, 1997-2012.

[4] F. Zhang, P. Wang, J. Koberstein, S. Khalid, S.-W. Chan, Surf. Sci., 563 (2004) 74-82.

[5] D.R. Mullins, S.H. Overbury, D.R. Huntley, Surf. Sci., 409 (1998) 13.

[6] S. Deshpande, S. Patil, S.V.N.T. Kuchibhatla, S. Seal, Appl. Phys. Lett., 87 (2005) 133113.

[7] R.A. Day, Jr., A.L. Underwood, Quantitative Analysis. 5th Ed, Prentice-Hall, Inc., 1986.

[8] S. Hommura, K. Kawahara, T. Shimohira, Y. Teraoka, J. Electrochem. Soc., 155 (2008) A29-A33.

[9] E. Endoh, S. Hommura, S. Terazono, H. Widjaja, J. Anzai, ECS Trans., 11 (2007) 1083-1091.

CHAPTER 3: CERIA AND MEMBRANE CHARACTERIZATION

3.1 Introduction

Cerium is a rare earth metal that, as an ion, has two oxidation states, 3+ and 4+ [1]. Cerium oxide or ceria can therefore exist as either Ce_2O_3 (hexagonal lattice) or CeO_2 (cubic fluorite lattice). Ceria is well-known for having the ability to facilely switch back and forth between its oxidation states without a break-up of its lattice structure. For example, the loss of a neutral oxygen atom creates an oxygen vacancy which is accounted for by the reduction of Ce^{4+} and Ce^{3+}. This reaction is a localized and therefore in ceria, generally, a higher concentration of Ce(III) is found on the surface of the particles than in the bulk.

Decreasing the size of particles increases their surface area to volume ratio resulting in higher non-uniformity on the surface of the material. At the nanoscale this effect is exacerbated with high lattice strain and an increase in surface oxygen vacancies. Deshpande *et al.* [2] established an increase in Ce^{3+} concentration with decreasing particle size.

Several publications have demonstrated a relationship between Ce(III) concentration and superoxide scavenging [1, 3-6]. In fuel cells, hydroxyl radicals are the main degrading agent. The quenching reaction of $HO^{\cdot}$ by cerium is given in Equation 3.1 [7, 8], demonstrating that in fuel cell reactions Ce(III) is of importance for degradation

mitigation. Ceria can act catalytically by returning to its Ce(III) oxidation state through reaction with hydrogen peroxide, as shown in Equation 3.2 followed by quenching of the resulting hydroperoxyl radical to form oxygen, as shown in Equation 3.3 [7, 8].

$$Ce^{3+} + HO^{\cdot} + H^{+} \rightarrow Ce^{4+} + H_2O \quad (3.1)$$

$$Ce^{4+} + H_2O_2 \rightarrow Ce^{3+} + HOO^{\cdot} + H^{+} \quad (3.2)$$

$$Ce^{4+} + HOO^{\cdot} \rightarrow Ce^{3+} + O_2 + H^{+} \quad (3.3)$$

3.2 Ceria Characterization

In order to better understand the cerium oxide used, the synthesized and commercial powders and ceria-containing membranes were studied by a variety of analytical techniques.

3.2.1 Diffraction

The XRD spectra of the synthesized and commercial ceria are shown in Figures 18 and 19, respectively. These spectra confirm the crystalline nature of both ceria formulations by the presence of typical cerium oxide 2θ peaks at 29, 33, 48 and 56, 77 and 79° [8]. The peaks for the synthesized ceria are less well defined compared to the peaks from the commercial material, an observation attributed to their very small particle size.

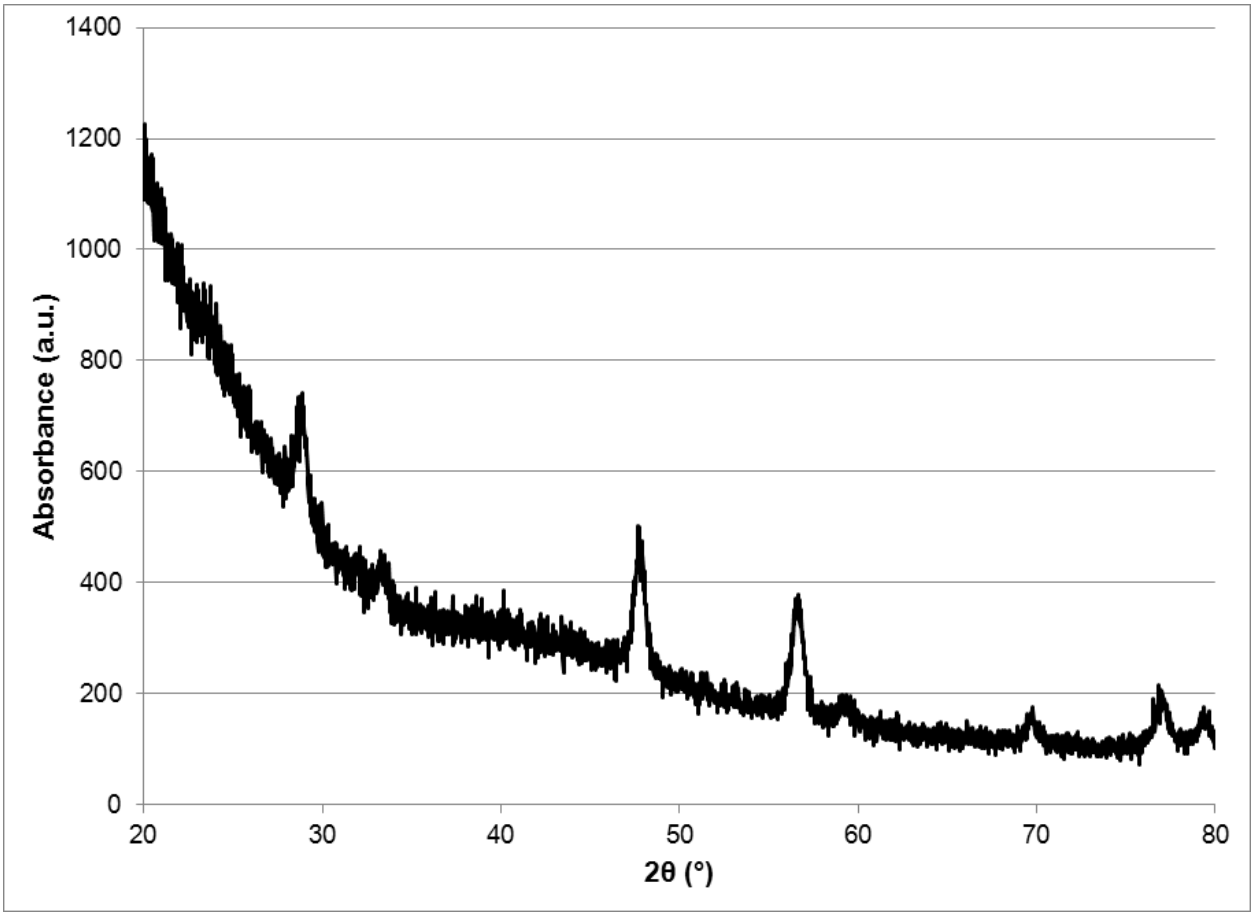

Figure 18 XRD spectrum of synthesized ceria

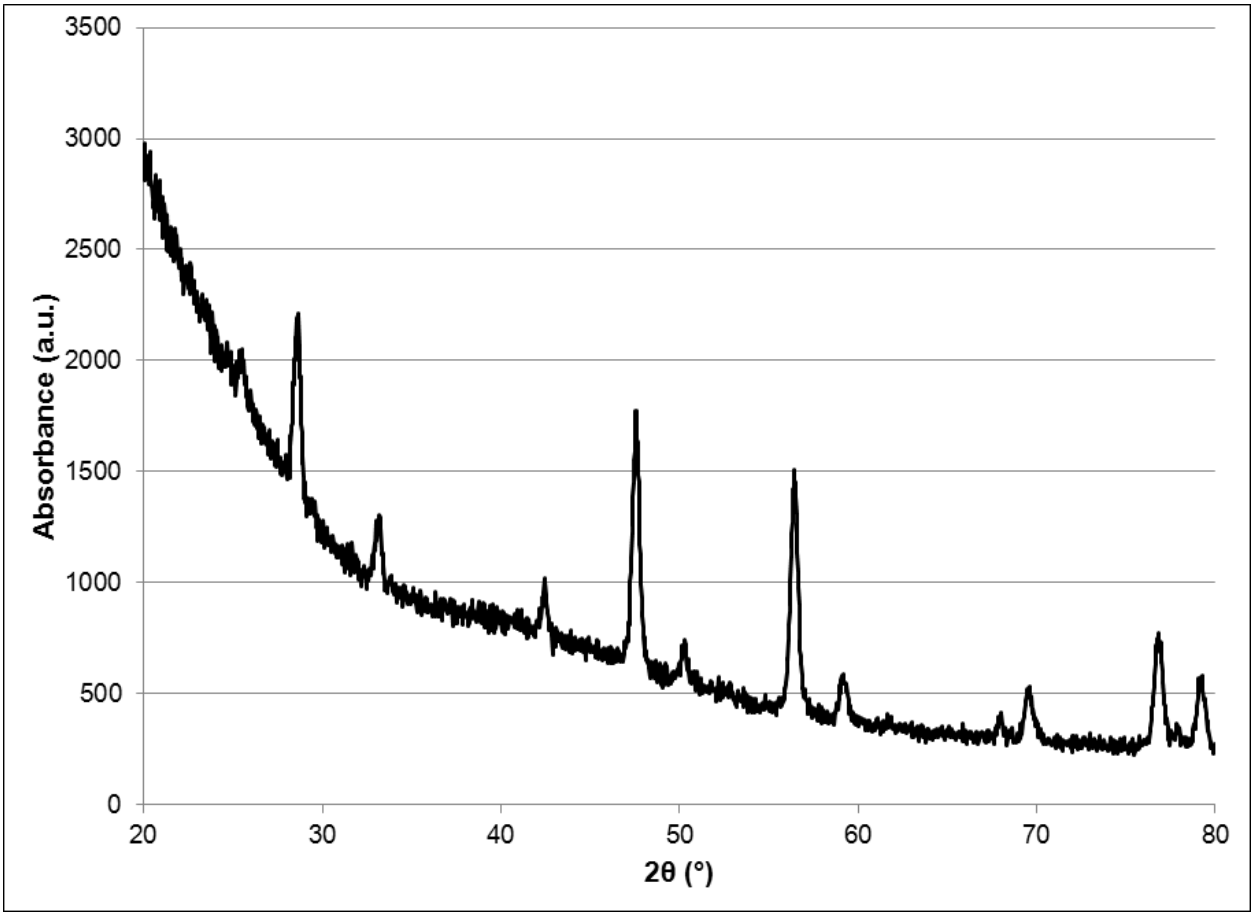

Figure 19 XRD spectrum of commercial ceria

Electron diffraction patterns from each powder are shown in Figure 20. The difference in the two ring patterns, characteristic of polycrystalline materials, reflects the difference in nanoparticle morphology. The sharper rings with discrete spots observed in commercial ceria (Figure 20b) suggest a larger particle size than the synthesized powder, which had wider, more diffuse diffraction rings (Figure 20a). The indexed diffraction patterns matched those of CeO_2.

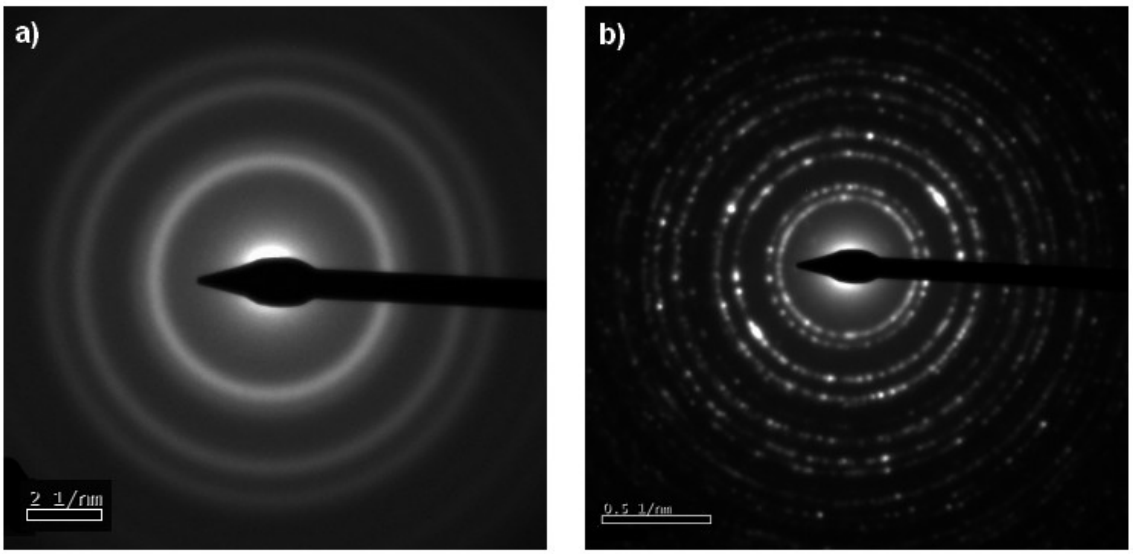

Figure 20 Electron diffraction pattern of a) synthesized ceria and b) commercial ceria

3.2.2 Electron Imaging and Energy-Dispersive X-ray Spectroscopy

3.2.2.1 Powders

The crystalline nature of both formulations was further confirmed by high magnification STEM imaging. The synthesized ceria, shown in Figure 21a, was made up of polycrystalline nanoparticles with a very uniform size distribution of 2-5 nm.

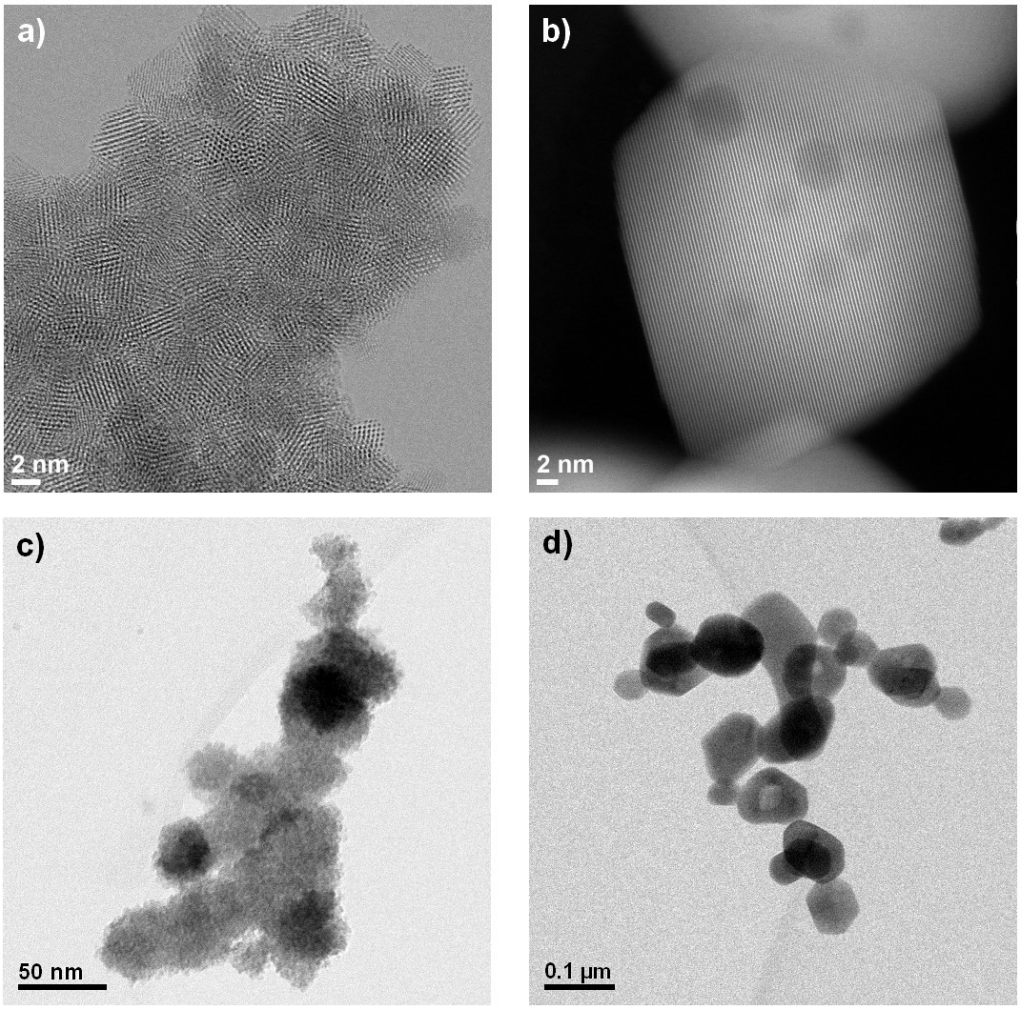

Figure 21 STEM Images of ceria powder: a) Bright-field image of synthesized ceria, b) Z-contrast image of commercial ceria, c) Bright-field image of agglomerated synthesized ceria and d) Bright-field image of agglomerated commercial ceria

The commercial ceria showed large, faceted particles on the order of 20 – 150 nm. As seen in the high magnification STEM image given in Figure 21b, the individual particles were single crystal and voids were also observed, which appear as dark regions within the particles. The low magnification STEM images of Figures 21c and d show that both formulations had the tendency to agglomerate and precipitate from the colloidal dispersions, with the commercial material falling out faster due to the larger particle sizes. This agglomeration resulted, on a microscopic level, in a heterogeneous distribution of particles during membrane casting, as seen in Figure 29a. Furthermore, increasing the amounts of ceria in the clear PFSA membranes resulted in an increase in opacity.

EDS spectra obtained from both samples are given in Figures 22 and 23. Using the standardless quantification routine within the Bruker Esprit software showed the atomic ratio of cerium to oxygen was within a few percent of the anticipated stoichiometry (Table 5).

Table 5 Atomic composition of ceria powders quantified through EDS measurements

	Normalized atomic %	
Atom	Synthesized	Commercial
Cerium	34%	37%
Oxygen	66%	63%

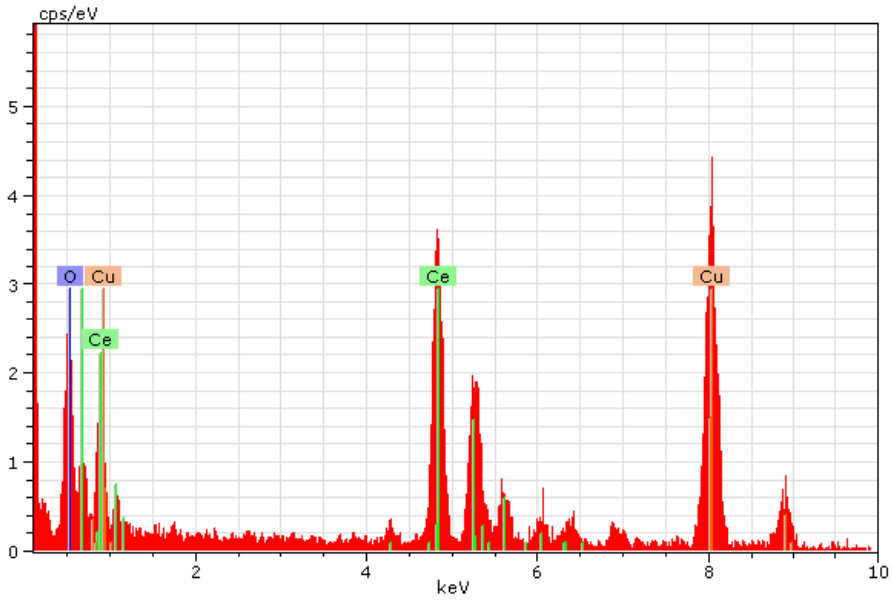

Figure 22 EDS spectrum of synthesized ceria

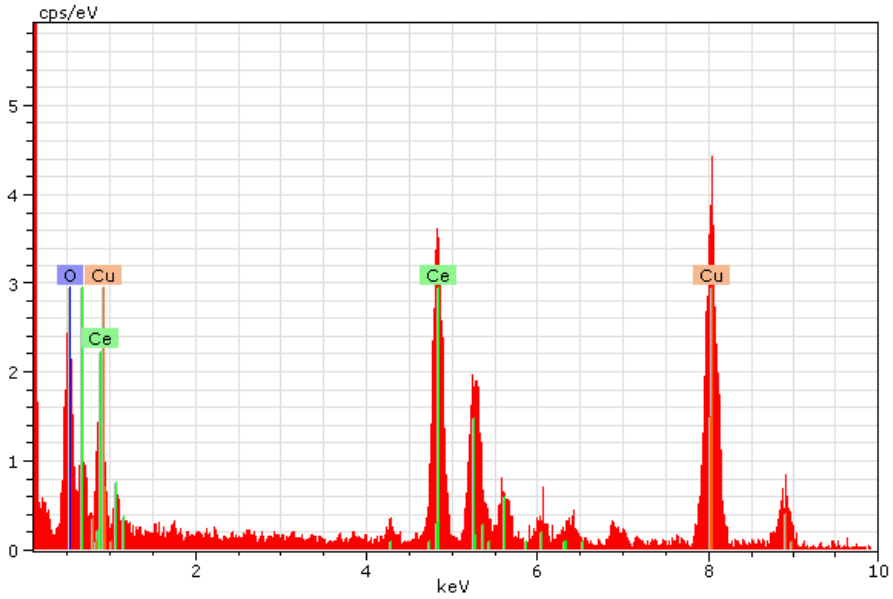

Figure 23 EDS spectrum of commercial ceria

3.2.2.2 In the Membrane

High magnification STEM imaging of membrane cross-sections (Figure 24) showed that both ceria samples, when incorporated into membranes, maintained the same morphology and crystal structure observed in the powder samples. EDS measurements confirmed that the nature of these particles was indeed cerium. However, due to the embedment in the membrane, the poorer signal provided data was not adequate for quantification.

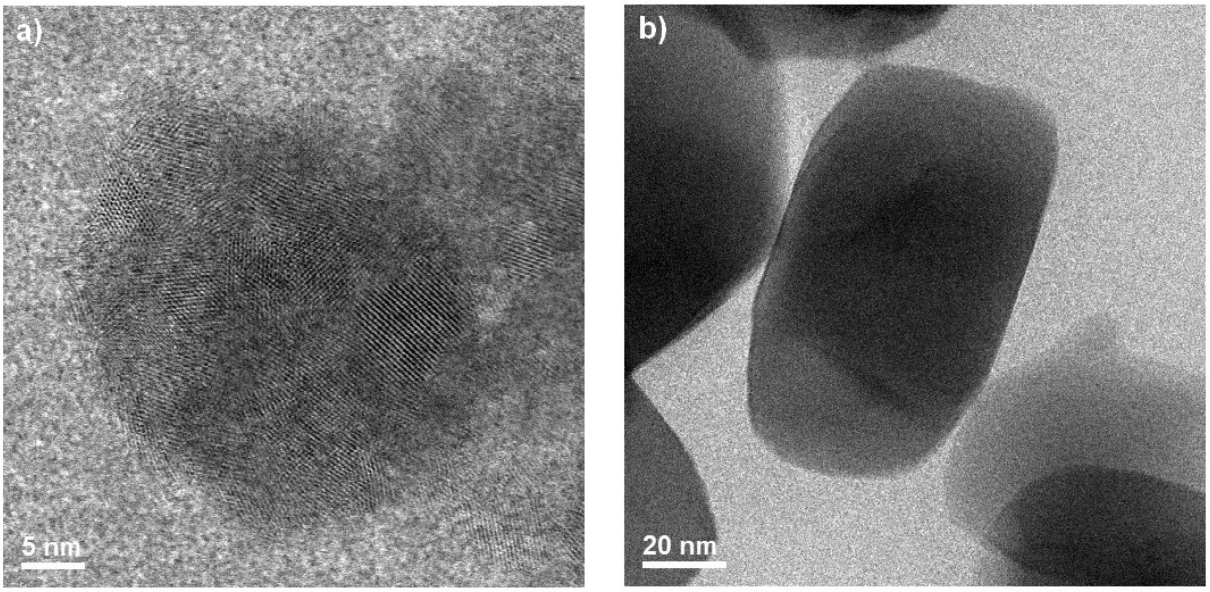

Figure 24 Bright-field STEM image of ceria powders in CCMs a) synthesized ceria in a 2.0 wt% untested CCM and b) commercial ceria in a 2.0 wt% untested CCM

3.2.3 X-Ray Photoelectron Spectroscopy

3.2.3.1 Powders

Synthesized and commercial ceria samples supported on a glass slide were measured on a Thermo Scientific instrument. The Ce3d5 peaks were deconvoluted following literature procedures [2, 9, 10]. Figures 25 and 26 show that the spectra obtained were well defined and matched literature data. The ratios of Ce(III) to Ce(IV) in the ceria formulations were obtained from the fitted curves and are shown in Table 6.

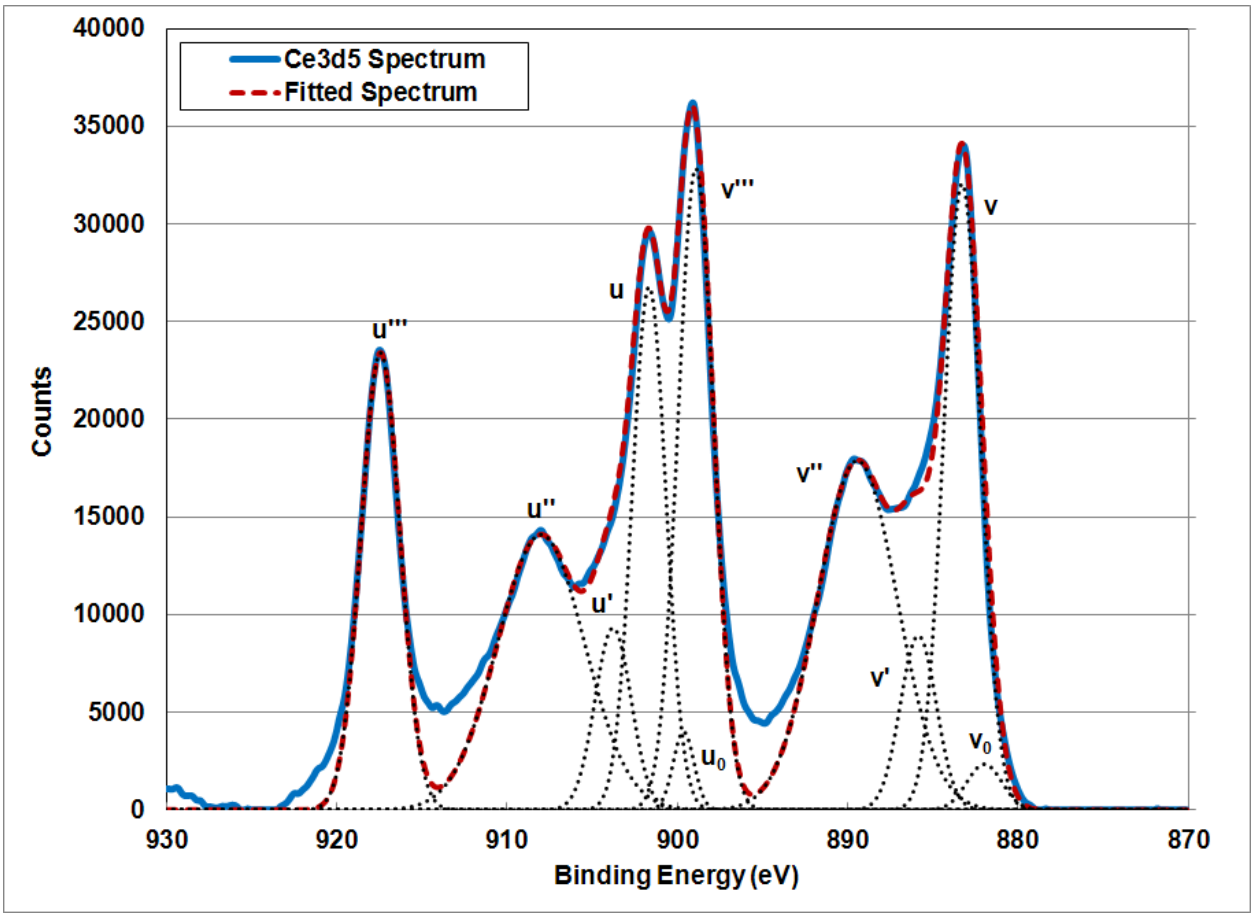

Figure 25 Spectrum of Ce3d5 peaks of synthesized ceria powder with fitted peaks from a Thermo Scientific K-Alpha XPS instrument

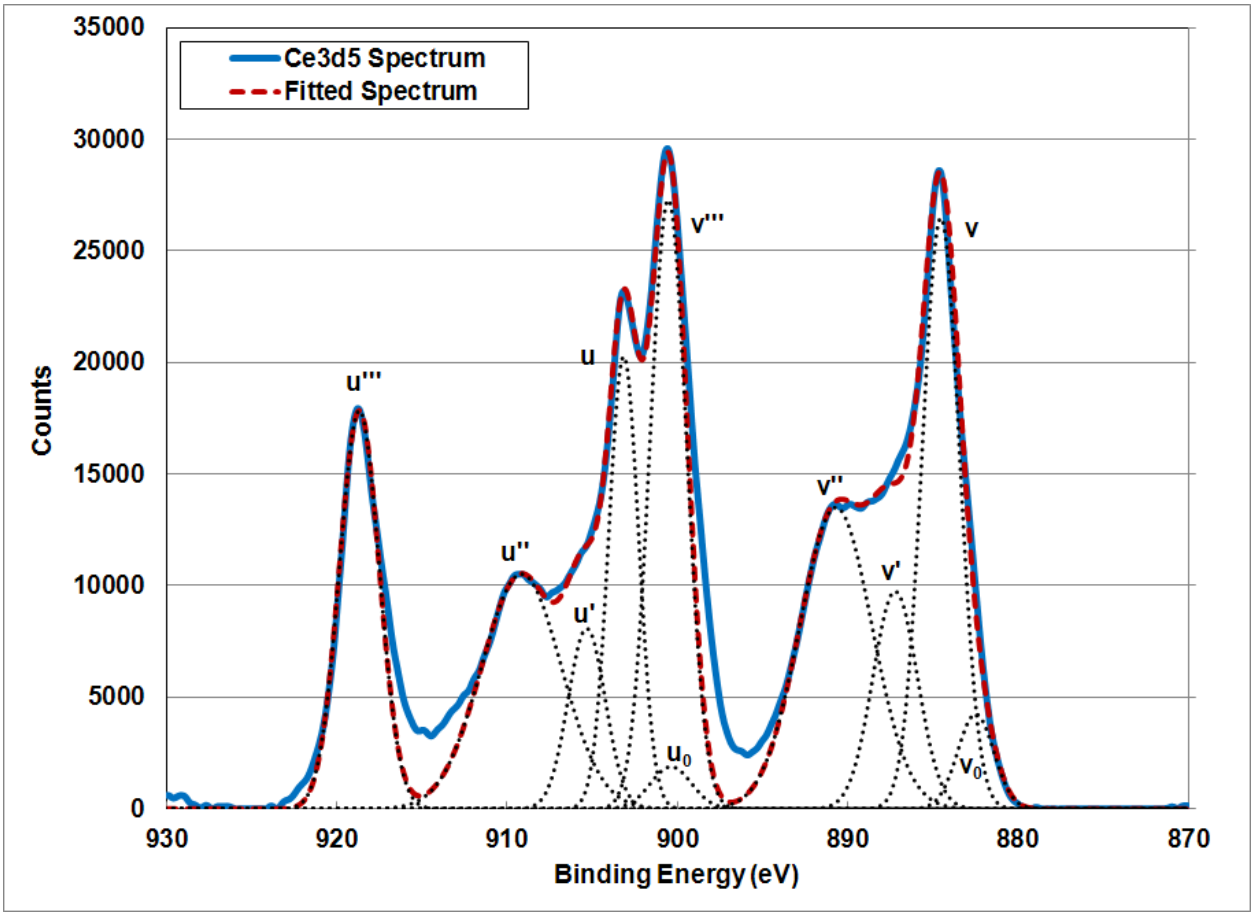

Figure 26 Spectrum of Ce3d5 peaks of commercial ceria powder with fitted peaks from a Thermo Scientific K-Alpha XPS instrument

Table 6 Ce(III) concentration of ceria nanoparticles calculated from XPS data

	Ce(III) Concentration
Synthesized ceria	11%
Commercial ceria	16%

An inverse proportionality between Ce(III) concentration and particle size has been demonstrated [2]. The data shown here stands in contradiction to those observations as a higher concentration of Ce(III) would be expected in the smaller particle

synthesized ceria. As only one measurement of each formulation was performed it was concluded that this discrepancy was within the margin of error of the experiment. It can, however, be said that the concentration of Ce(III) for both is low.

3.2.3.2 In CCMs

It is of interest to know the oxidation state of ceria after fuel cell testing. As explained below, it was observed that cerium oxide is reduced to Ce^{3+} ions when exposed to the conditions experienced during proton conductivity measurements (see section "3.2.5 Proton Conductivity"). The behavior in CCMs is unknown.

Attempts were made to determine the oxidation states of the ceria in CCMs that had been tested in 94 h OCV hold testing. To do this, synthesized 2.0 wt% ceria- and commercial 2.0 wt% ceria-containing CCMs were cut at a low angle to obtain longer cross-sections. The ca. 400 µm cross-sections were scanned with a 50 µm X-ray spot size on the Thermo Scientific XPS instrument. This method was also employed in an attempt determine the location of ceria, which is known to disperse during operation (also see section "3.2.5 Proton Conductivity").

Though cerium was observed, its peaks were too small to allow deconvolution and thereby concentration calculations. The large spot size also did not enable the determination of the location of ceria within the membrane.

3.2.4 Solution Reactions

To explore certain aspects of ceria's chemical behavior, experiments were performed in liquid environments that mimicked its environment during the synthesis, membrane treatment, proton conductivity measurements and accelerated durability tests. Suspensions of both ceria formulations (7 mM) were made in:

- water to mimic various membrane treatment steps,
- ethanol to mimic the synthesis and
- 1 M sulfuric acid to mimic various membrane treatment steps and the generally acidic environment that the additives experience in the membrane.

The dispersions, aided by sonication, yielded milky-white suspensions with ceria precipitating as a yellow-white powder over time. The commercial material fell out faster due to its larger particle size. To model the behavior of ceria with respect to the Fenton and OCV hold experiments, where membranes are exposed to hydrogen peroxide, a tenfold molar amount of H_2O_2 with respect to cerium was added to some of the suspensions. Similarly, to model the behavior of ceria with respect to iron(II), as experienced during the Fe^{2+} ion-exchange process (section "2.13.2 Fe^{2+} Ion-Exchange"), a tenfold molar amount of $FeSO_4$ with respect to cerium was added to some of the suspensions. The results of the experiments are discussed in detail below.

Figure 27 shows the UV/Vis spectra of several solutions used in the experiment, among them one containing both Ce^{3+} and Ce^{4+} ions. Ce^{3+} shows a strong absorbance around 265 nm and Ce^{4+} around 315 nm.

3.2.4.1 In Water and Ethanol

Reactions in water and ethanol were found to be very similar to each other and will be discussed as one.

Addition of hydrogen peroxide to the water or ethanol suspension resulted in a color change from milky-white to orange, indicating the oxidation of Ce(III) to Ce(IV). Addition of iron(II) sulfate yielded an orange precipitate that was considered to be an iron compound. The color change for the commercial ceria was not as visibly strong.

3.2.4.2 In 1 M Sulfuric Acid

In sulfuric acid, the synthesized ceria dissolved after about a week to form a clear, yellow-green solution. The UV/Vis spectrum given in Figure 27 shows a large peak around 325 nm demonstrating that the solution consisted almost entirely of Ce(IV). A TEM image of the solution evaporated onto a copper grid showed no particles confirming that the ceria had indeed been dissolved to Ce^{4+} ions. The commercial ceria, however, did not dissolve in 1 M H_2SO_4, even after months of exposure.

Addition of hydrogen peroxide to both ceria suspensions resulted in the formation of a clear solution. As seen in Figure 27, the UV/Vis spectrum of both solutions was identical with a large peak at 270 nm, demonstrating the reduction of cerium oxide to Ce^{3+} ions.

However, the difference in time scales for the two reactions was significant. The synthesized ceria formed the clear solution within 10 min of the peroxide addition while the same reaction was only observed 4 weeks later for the commercial material.

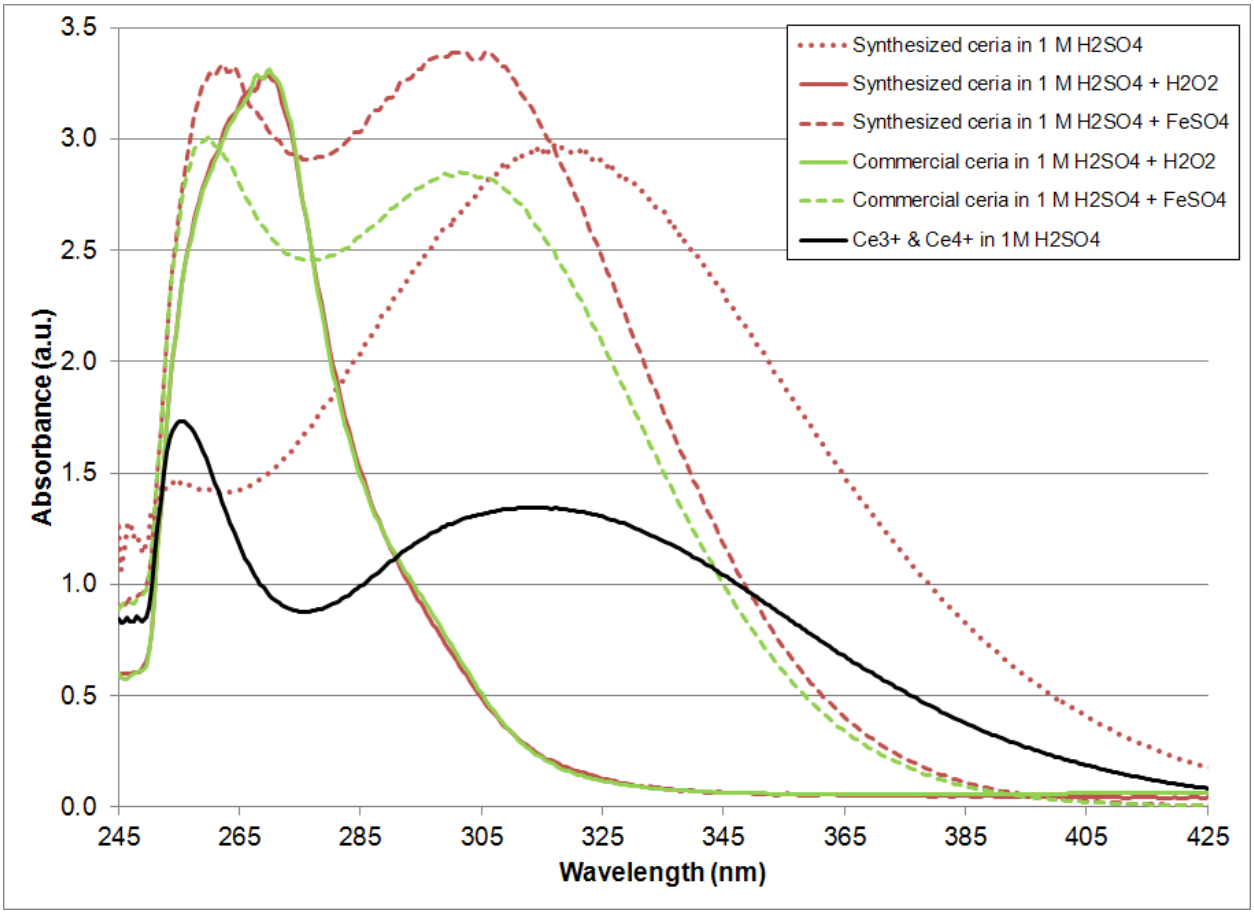

Figure 27 UV/Vis absorbance spectrum of various cerium-containing solutions

Similarly, the addition of iron(II) sulfate caused a change of the milky-white suspension to a clear solution. Its UV/Vis spectra showed two peaks that were very similar to the mixed cerium ion solution. The first absorbance at 260 nm was characteristic of Ce(III) and the second at 305 nm of Ce(IV). This suggests that both dissolution and reduction

of the cerium oxide is occurring, resulting in a solution of Ce^{3+} and Ce^{4+} ions. Once again, the main difference between the two ceria formulations was the kinetics. Upon addition of iron sulfate, the synthesized ceria dissolved instantaneously, while the same reaction took approximately one day for the commercial material.

With the exception of the dissolution in acid, which did not occur for the commercial ceria on the time scale measured, both ceria formulations showed very similar chemical behavior, with the main difference being the rates of the reactions. This difference in kinetics is thought to be due to the greater than one order of magnitude larger particle size of the commercial ceria. [11].

3.2.5 Proton Conductivity

One important metric of an ionomer's suitability as a membrane for PEM fuel cells is its ability to conduct protons. PFSA ionomers used in fuel cells are able to transport protons by either diffusion through absorbed water or by the Grotthus mechanism where protons hop from one sulfonic acid group to the next via conducting channels [12] (see section "1.3.2: Proton Conductivity". For either mechanism, the level of conduction is dependent on the level of hydration and, hence, the relative humidity to which the membrane is exposed. Though some research groups have used zirconium-based reagents to improve humidification, and thereby conductivity [13, 14], incorporation of additives into PFSA membranes can have a detrimental effect on proton conduction if the particles inhibit either of these two mechanisms [15-18].

To determine the effect of added ceria, attempts were made to measure the in-plane proton conductivity at various relative humidities. The method of measurement involved holding membranes at each relative humidity level and allowing enough time for the membrane to reach a steady-state condition. However, for ceria-containing membranes, the conductivity was found to slowly but continually decrease over time, with a concurrent decrease in membrane opacity. To determine the cause of this phenomenon, the proton conductivity was measured while holding the membranes at 80 °C and 70% RH for up to ~90 h.

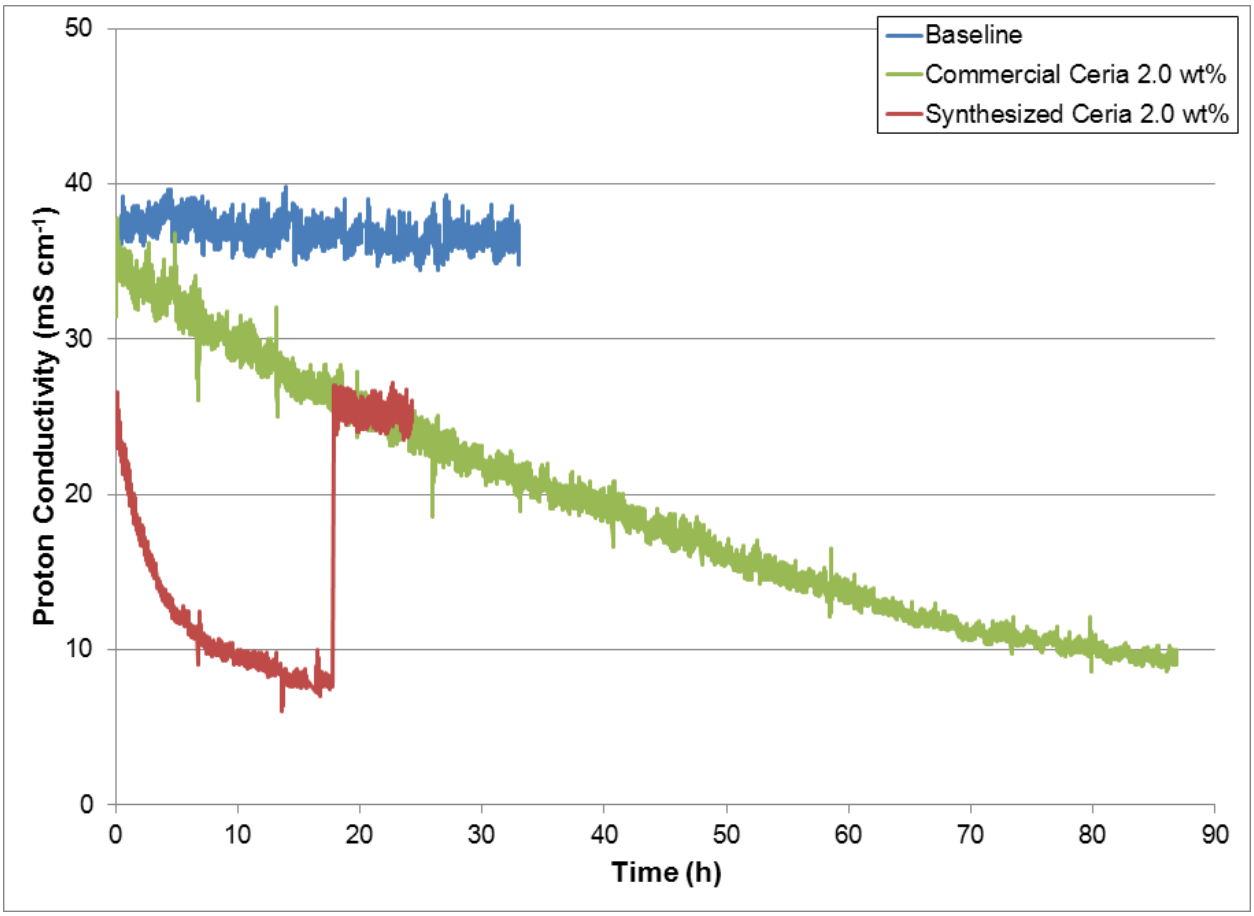

Figure 28 In-plane proton conductivity of various membranes held at 80 °C and 70% RH

Figure 28 shows no significant change in the conductivity of the baseline material, even over 30 hours of measurement, yielding a typical value for PFSAs of 35 mS cm^{-1} [8]. Both ceria-containing membranes, on the other hand, showed a greater than three-fold decrease in proton conductivity, which did not reach a minimum even after 18 and 90 hours for the synthesized and commercial ceria, respectively (the increase in conductivity for the synthesized material at ~18 hours is discussed further below).

In order to gain a better understanding of the loss in membrane opacity and decrease in proton conductivity, further tests were conducted. Figures 29a and b show SEM images of the cross-sections of the synthesized ceria-containing membrane before and after 18 hours of measurements at 80 °C and 70% RH, respectively. Before testing, the agglomeration of ceria around the PTFE support was clearly visible in the form of a intermittent band of white nanoparticles. These particles were no longer observable after conductivity testing.

However, EDS mapping of a six hour tested membrane, shown in Figure 29c, clearly demonstrates the presence of cerium, as seen by the intense band highlighted by the white rectangle. The ceria particles, after being exposed to conductivity measurement conditions, were distributed over a much larger region, indicating the dispersal of the ceria agglomerates, which was considered as one of the causes leading to the decrease in opacity.

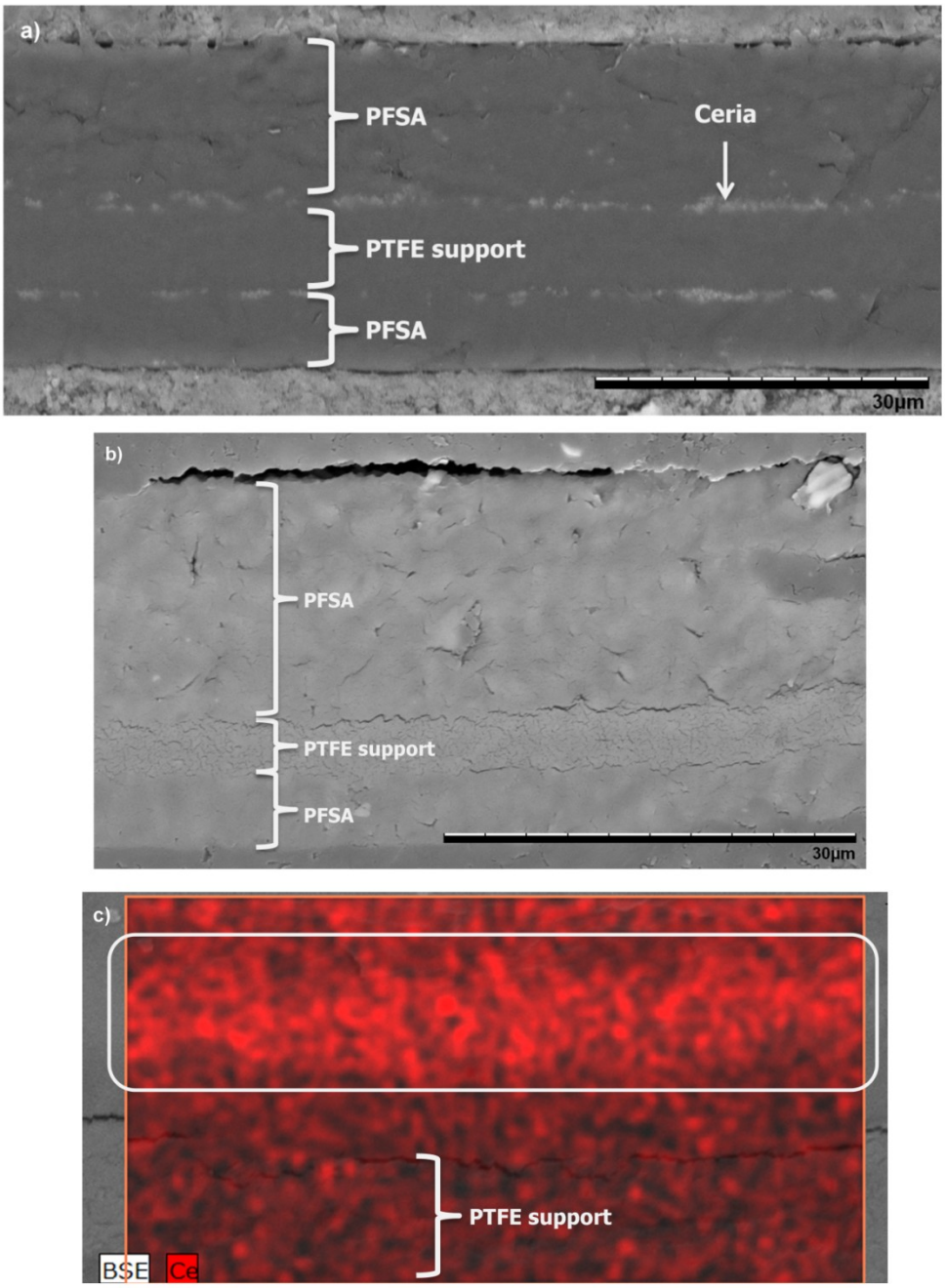

Figure 29 SEM images of cross-sections of a 2.0 wt% synthesized ceria-containing membrane a) before proton conductivity testing, b) after 18 h of proton conductivity testing and c) after six hours of proton conductivity testing with an EDS cerium map overlay (intense cerium band highlighted by white rectangle)

To probe any changes in the chemical nature of the ceria and further understand the complete loss of opacity, UV/Vis spectroscopy measurements were performed. As mentioned Ce(III) and Ce(IV) absorb strongly in the ultraviolet spectrum; ~265 nm and ~315 nm for ionic solutions, respectively. Figure 30 shows the UV/Vis spectra of various membranes, some of which had been exposed to proton conductivity measurements. Prior to testing, both synthesized and commercial ceria membranes showed a broad absorbance from 225 to 400 nm. After conductivity measurements, a noticeable change in the spectrum was observed with a strong peak having developed 255 nm. The UV/Vis spectrum of a baseline membrane ion-exchanged with Ce^{3+} is also plotted which shows very similar absorbance to the tested membranes, strongly indicating the conversion of cerium oxide to Ce^{3+} ions.

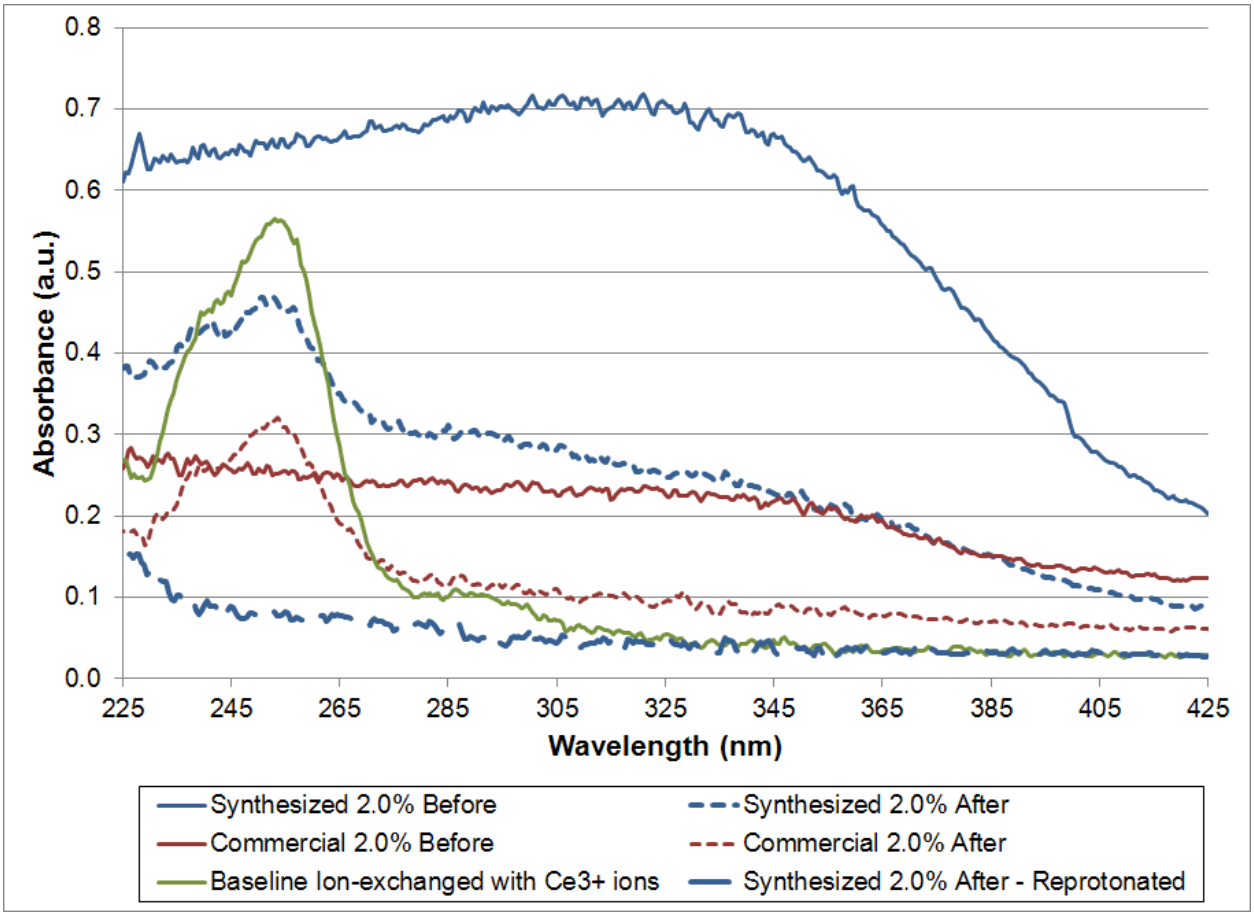

Figure 30 UV/Vis spectra of various membranes before and after conductivity measurements

Um *et al.* [11] had previously shown that in highly concentrated solutions (>8 M) of sulfuric acid at high temperatures (>80 °C), cerium oxide will dissolve and react to form Ce(III) ions, as shown in Equation 3.4:

$$4\ CeO_2 + 12\ H^+ \rightarrow 4\ Ce^{3+} + 6\ H_2O + O_2 \qquad (3.4)$$

Given that PFSAs are classified as superacids and are significantly more acidic than H_2SO_4 (pK_a of -6 and -3 respectively) [19], it is here postulated that during the

humidification process and exposure to flowing gases, the cerium oxide moves throughout the membrane, and is reduced to Ce^{3+} following the reaction given in Equation 3.4. The ions bind to the sulfonate groups resulting in decreased proton conductivity. This conclusion was further confirmed upon reprotonation. After 18 hours of testing the synthesized ceria membrane was immersed in 0.5 M sulfuric acid, which regenerated the PFSA acid sites by replacing the Ce^{3+} with H^{+} ions. This not only returned the membrane's proton conductivity to its original value (Figure 28), but also, as shown in Figure 30, the 255 nm peak in the UV/Vis spectrum disappeared, leaving an absorbance spectrum that was identical to that of a baseline membrane.

As with the solution experiments, the noticeable difference in reaction kinetics is a consequence of the difference in particle size. The commercial ceria diffused slower, due to its large particles, and therefore the kinetics of Ce^{3+} formation and consequent impact on the conductivity were decreased.

Further experiments showed that this reaction occurred even when the membrane was not exposed to cyclic voltammetry or placed in contact with the platinum electrodes, as well as when inert gases were used in place of hydrogen, demonstrating that this reaction was independent of external influences, such as electrochemical reactions or reducing reagents. Similar behavior was observed elsewhere for MnO_2 radical scavenging material [20].

3.3 Conclusion

Cerium oxide nanoparticles were synthesized through the thermal hydrolysis of a Ce(IV) salt in ethanol. Diffraction and electron microscopy measurements showed that the particles were crystalline and had a uniform size distribution of 2-5 nm, which compared to a commercial ceria that was also crystalline but had an order of magnitude larger particles. From X-ray photoelectron spectroscopy measurements, the concentration of Ce^{3+} was estimated and found to be low and, within error, similar for each formulation.

Both nanoparticle formulations were incorporated in perfluorosulfonic acid membranes and found to agglomerate around the polytetrafluoroethylene backing, but did not change their crystal structure or size.

Solvent experiments showed that both formulations, when suspended in sulfuric acid, were susceptible to reaction with hydrogen peroxide, forming solutions of Ce^{3+} ions. The addition of iron sulfate, also a reducing agent, to acidic suspensions, however, mainly resulted in an increase in the dissolution kinetics of the ceria, with some reduction occurring. The commercial ceria, due to its larger particle size, reacted slower than the synthesized material.

In proton conductivity measurements, the initial conductivity of the membranes was found to be unaffected by the presence of ceria. However, prolonged exposure to the hot, humid gas-flowing conditions resulted in the diffusion of the ceria throughout the

membrane and its reduction to Ce^{3+}. The driving force of this reaction is the high acidity of the membrane and the formation of ions results in a decrease in proton conductivity.

3.4 References

[1] A. Karakoti, S. Singh, J.M. Dowding, S. Seal, W.T. Self, Chem. Soc. Rev., 39 (2010) 4422-4432.

[2] S. Deshpande, S. Patil, S.V.N.T. Kuchibhatla, S. Seal, Appl. Phys. Lett., 87 (2005) 133113.

[3] S. Babu, A. Velez, K. Wozniak, J. Szydlowska, S. Seal, Chem. Phys. Lett., 442 (2007) 405-408.

[4] A. Karakoti, in: Mechanical, Materials and Aerospace Engineering University of Central Florida Orlando, 2010.

[5] A.S. Karakoti, N.A. Monteiro-Riviere, R. Aggarwal, J.P. Davis, R.J. Narayan, W.T. Self, J. McGinnis, S. Seal, JOM, 60 (2008) 33-37.

[6] C. Korsvik, S. Patil, S. Seal, W.T. Self, Chem. Commun., (2007) 1056-1058.

[7] F.D. Coms, H. Liu, J.E. Owejan, ECS Trans., 16 (2008) 1735-1747.

[8] P. Trogadas, J. Parrondo, V. Ramani, Electrochemical and Solid State Letters, 11 (2008) B113-B116.

[9] F. Zhang, P. Wang, J. Koberstein, S. Khalid, S.-W. Chan, Surf. Sci., 563 (2004) 74-82.

[10] D.R. Mullins, S.H. Overbury, D.R. Huntley, Surf. Sci., 409 (1998) 13.

[11] N. Um, M. Miyake, T. Hirato, Zero-Carbon Energy Kyoto, (2011) 165-170.

[12] W.H.J. Hogarth, J.C. Diniz da Costa, G.Q. Lu, J. Power Sources, 142 (2005) 223-237.

[13] G. Alberti, M. Casciola, D. Capitani, A. Donnadio, R. Narducci, M. Pica, M. Sganappa, Electrochim. Acta, 52 (2007) 8125-8132.

[14] K.T. Park, U.H. Jung, D.W. Choi, K. Chun, H.M. Lee, S.H. Kim, J. Power Sources, 177 (2008) 247-253.

[15] D. Zhao, B.L. Yi, H.M. Zhang, H.M. Yu, Journal of Membrane Science, 346 (2010) 143-151.

[16] M.M. Mench, E.C. Kumbur, T.N. Veziroglu, Editors, Polymer Electrolyte Fuel Cell Degradation, 1st ed., Elsevier Ltd., 2012.

[17] G.M. Haugen, F. Meng, N. Aieta, J.L. Horan, M.-C. Kuo, M.H. Frey, S.J. Hamrock, A.M. Herring, ECS Trans., 3 (2006) 551-559.

[18] K. Wang, S. McDermid, J. Li, N. Kremliakova, P. Kozak, C. Song, Y. Tang, J. Zhang, J. Zhang, J. Power Sources, 184 (2008) 99-103.

[19] F.D. Coms, ECS Trans., 16 (2008).

[20] F. Finsterwalder, M. Quintus, T. Soczka-Guth, in: Fuel Cell Durability & Performance, Daimler, Ulm, Germany, 2008.

CHAPTER 4: FENTON TESTING

4.1 Introduction

Since membrane degradation is driven by hydroxyl radicals, the Fenton test has been used as an ex-situ accelerated durability test method for hydrogen fuel cell membranes. As described in section "1.3.7 Fenton Testing", this involves exposing a membrane to hydrogen peroxide in the presence of catalytic amounts of Fe^{2+}, which results in the formation of the destructive radicals (Equation 4.1) [1-4].

$$Fe^{2+} + H_2O_2 + H^+ \rightarrow Fe^{3+} + H_2O + HO\cdot \qquad (4.1)$$

However, doubts have been cast on the validity of this test, as discussed below, in relation to actual fuel cell testing, especially when comparing perfluorosulfonic acid to hydrocarbon membranes. Some of the latter fared very poorly in Fenton tests but were found to perform well in OCV hold degradation testing due to their lower hydrogen crossover. It has also been argued that the conditions that membranes encounter in a fuel cell involve gas-phase radicals, as opposed to the liquid conditions of traditional Fenton tests. As such, three separate research groups have independently developed a gaseous version of the Fenton test [5-7]. In this setup, iron ion-exchanged membranes are exposed to a hydrogen peroxide vapor at low RH, which has resulted in greater degradation than in equivalent liquid tests. This observation was described as originating from a side-chain scission reaction, though no further reaction mechanisms

were given at the time. These have since been described as sulfonic acid hydrogen abstraction and ether-adjacent carbon attack.

Despite its weaknesses, the Fenton test, both in its liquid and gaseous form, is useful as a method for determining the efficacy of ceria as a radical scavenger in membranes as a function of both concentration and formulation versus a baseline material.

4.2 Fe^{2+} Uptake

For both the liquid Fenton test (LF) and the gas Fenton test (GF), membranes were ion-exchanged with Fe^{2+} by immersion in an iron(II) sulfate solution with a ratio of protons in the membrane to ions in solution of 10:1 as described in section "2.13.2 Fe^{2+} Ion-Exchange". The aim of this procedure was to have 20% of the proton sites occupied by Fe^{2+}.

To verify that the appropriate level of ion-exchange had been achieved, the iron ions from ion-exchanged membranes were extracted into solution by immersion in 1 M KCl and quantified against calibration curves by UV/Vis spectroscopy at 508 nm using 1,10-phenanthroline as a complexing agent [8], as described in section "2.13.3 Fe^{2+} Uptake Determination".

Figure 31 shows the Fe^{2+} uptake as function of ceria concentration. The amount of iron-exchange for a plain PFSA membrane was found to be ~17%, slightly below the desired level. However, increased concentrations of ceria in the membranes decreased the level of iron ion uptake up to four fold. The type of ceria used also impacted the uptake, with larger concentrations being retained with synthesized ceria.

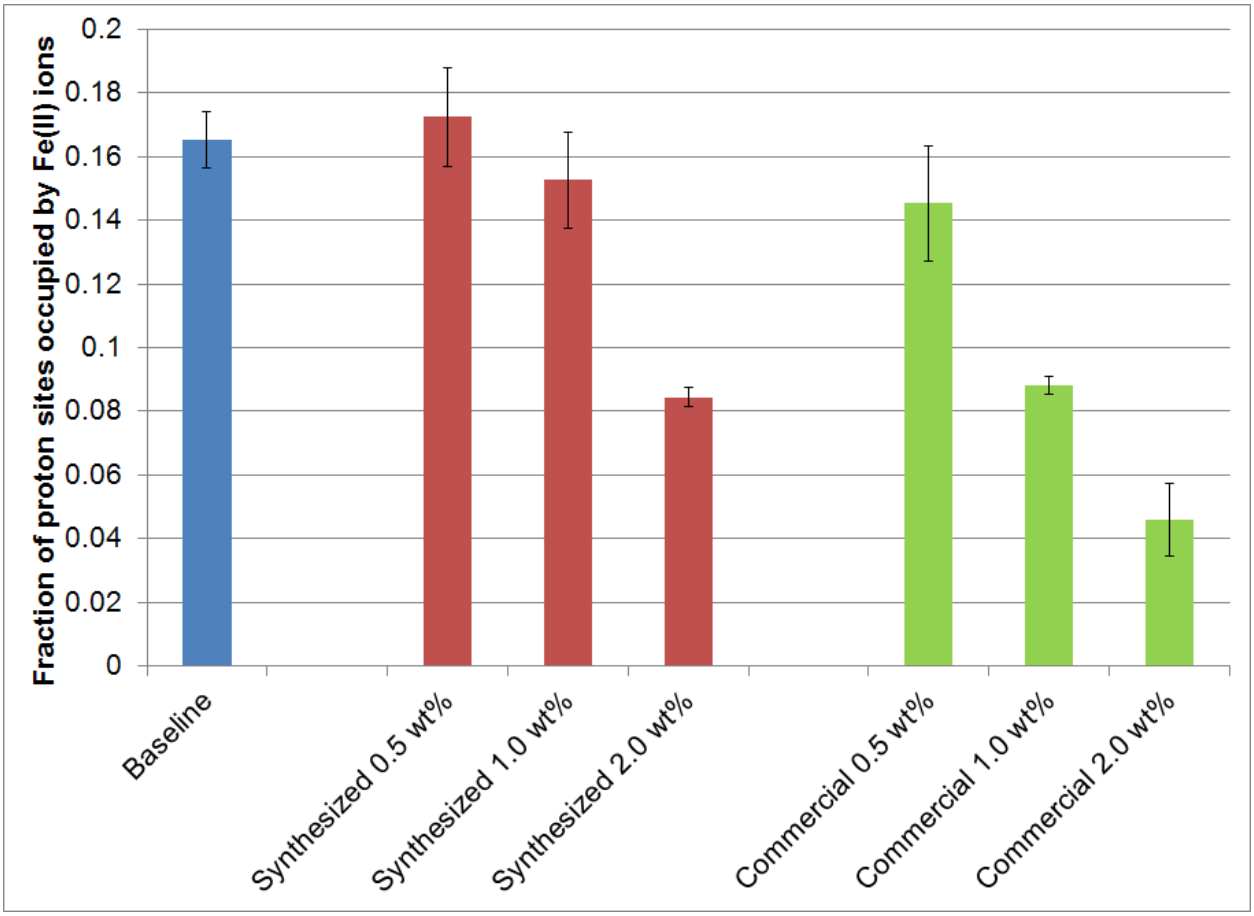

Figure 31 Fe^{2+} uptake of ceria-containing membranes

4.3 Fenton Tests

4.3.1 Emission of Fluoride

As mentioned, ceria has the ability to scavenge radicals by facilely switching the oxidation states of the cerium ions within its lattice. The catalytic scavenging reactions of cerium were given earlier in given in Equation 3.1, 3.2 and 3.3 [4, 9].

Figures 32 and 33 show the results for Fe^{2+} ion-exchanged membranes exposed to liquid and gaseous hydrogen peroxide. In both tests, ceria produced a large decrease in the emission of fluoride, a degradation mitigation effect that increased with increasing additive concentration up to an order of magnitude. The durability improvement was independent of the ceria formulation and therefore particle size.

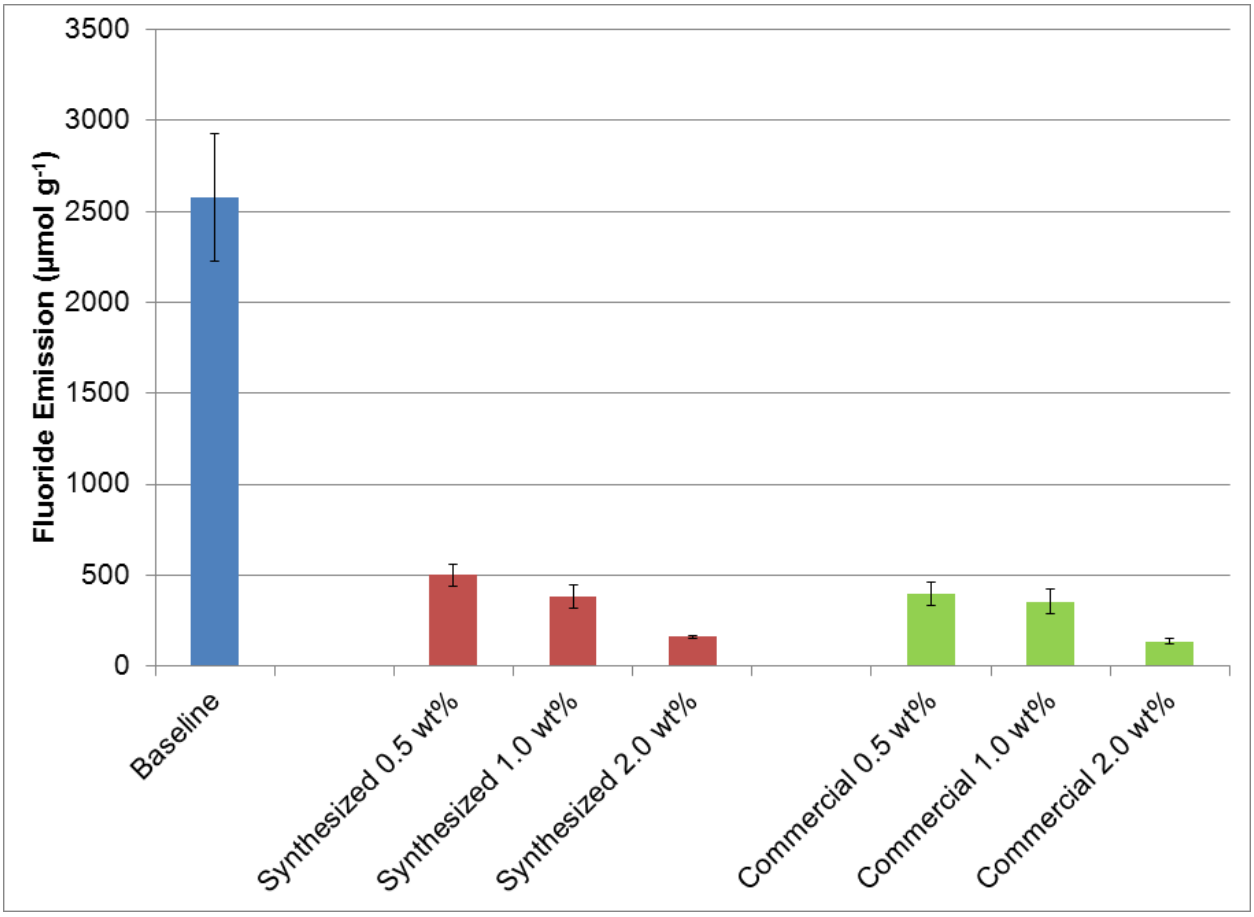

Figure 32 Normalized total fluoride emission after 48 h for the liquid Fenton test

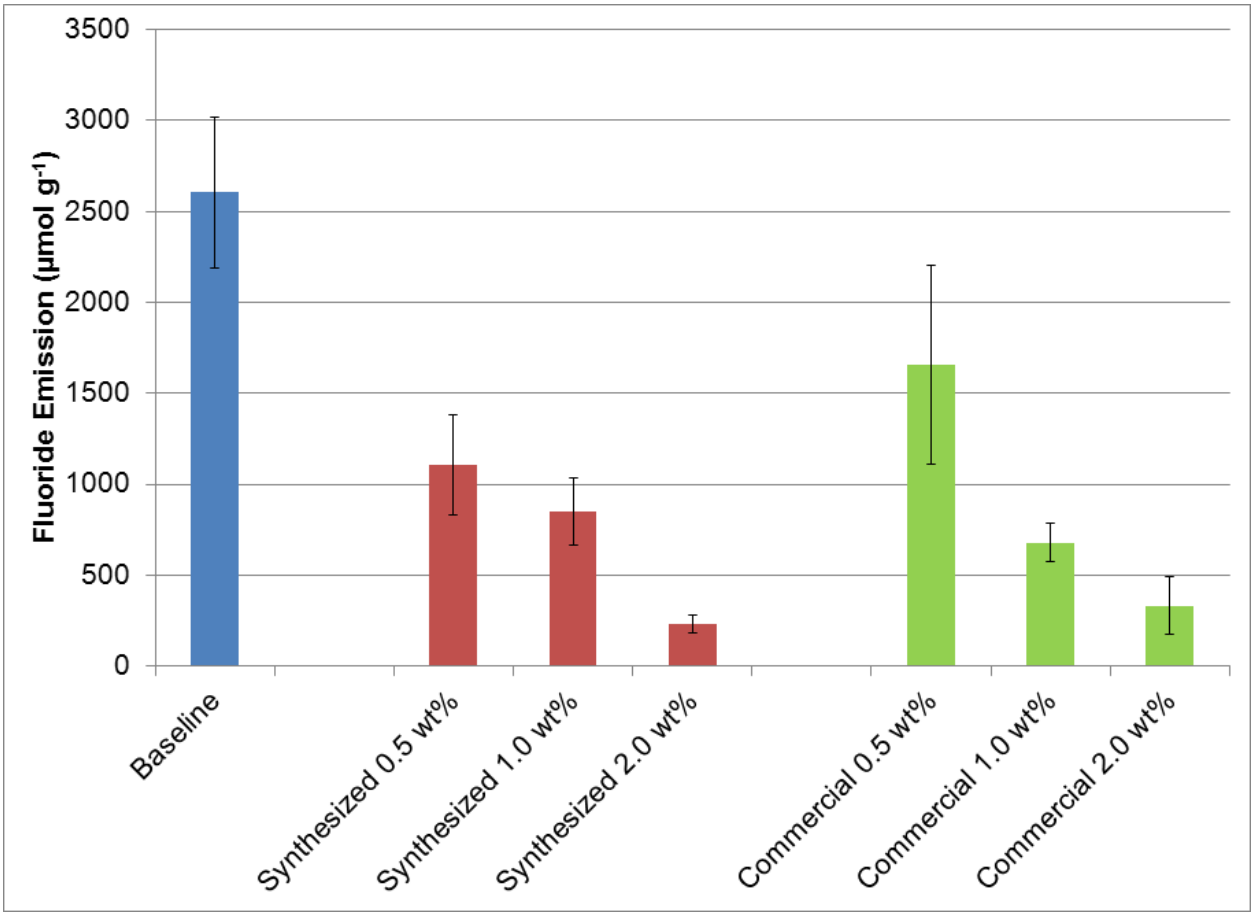

Figure 33 Normalized total fluoride emission after 48 h for the gas Fenton test

However, for the LF, the initial emission of fluoride reduction was significantly more pronounced than for the GF. It is thought that this difference was a consequence of the different reaction mechanisms that are effective in the different phases.

In solution, the majority of hydroxyl radicals that are formed react with the large amounts of available hydrogen peroxide more rapidly than with the low concentrations of vulnerable groups of the membrane. This reaction, given in Equation 4.2, produces

HOO·. This radical is less reactive than HO· and only capable of attacking COOH end groups. Due to its longer life and the lower concentration of potential reaction targets, it has a higher likelihood of diffusing to a ceria particle where it is reduced to oxygen, as shown in Equation 3.3.

$$HO\cdot + H_2O_2 \rightarrow HOO\cdot + H_2O \qquad (4.2)$$

Consequently, even low concentrations of ceria can significantly decrease degradation and increases in additive concentration result in only slight further improvement. However, in the vapor phase of the GF, the HO· is not in close contact with many other H_2O_2 molecules and therefore has a higher residence time to attack the membrane. As opposed to the hydroperoxyl radical, the hydroxyl radical, in addition to reacting with COOH end groups, can attack sulfonic acid hydrogen atoms (a significant number of which reside on their sulfonic acid groups due to the low RH of the experimental setup (~40%) [10, 11]) and ether group adjacent carbon atoms. The combination of the higher concentration of the more reactive radical and greater number of vulnerable targets yields a smaller time frame for added ceria to mitigate membrane degradation. For this reason, higher concentrations of ceria have a greater impact on the fluoride emission in the LF tests.

4.3.2 Reaction Products

During the measurement of fluoride by ion chromatography, a number of other ions were observed in the solutions. A representative spectrum is shown in Figure 34. Fluoride and sulfate, typical PFSA degradation products [10, 12, 13], and the occasional chloride contamination from the hydrogen peroxide and potassium hydroxide solutions were identified. For the GF, two additional unknown peaks were observed. A representative ^{19}F NMR spectrum of the reduced eluents, given in Figure 35, consists of a singlet at −75 ppm and a doublet at −119 ppm. The singlet matched literature NMR data for trifluoroacetic acid [14], which was confirmed by the IC retention time of pure solutions. The lower shift peak is thought to be the fluoride ion. One other IC peak could not be identified with NMR spectroscopy but retention time analysis suggested that the molecule was formic acid.

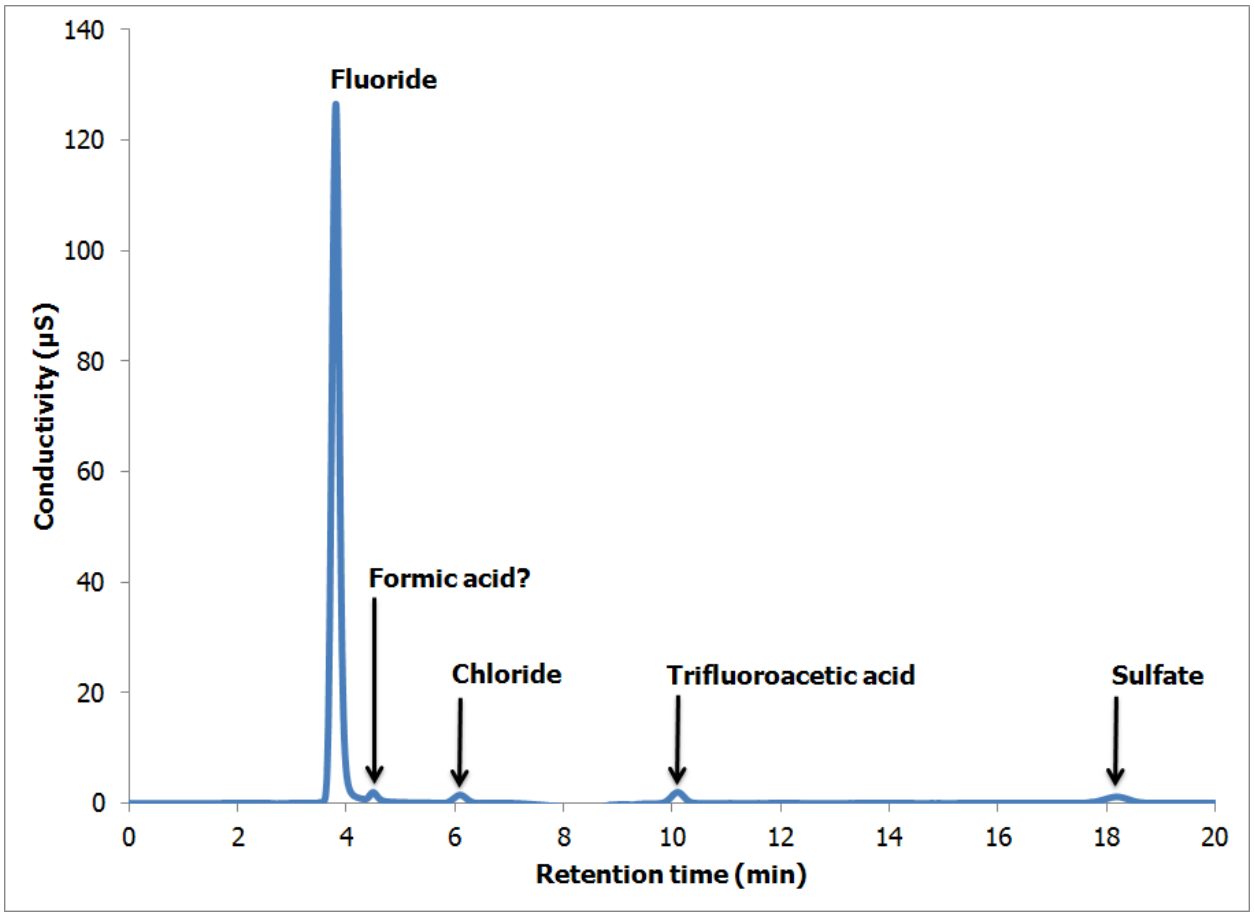

Figure 34 Representative IC spectrum of a Fenton test effluent sample

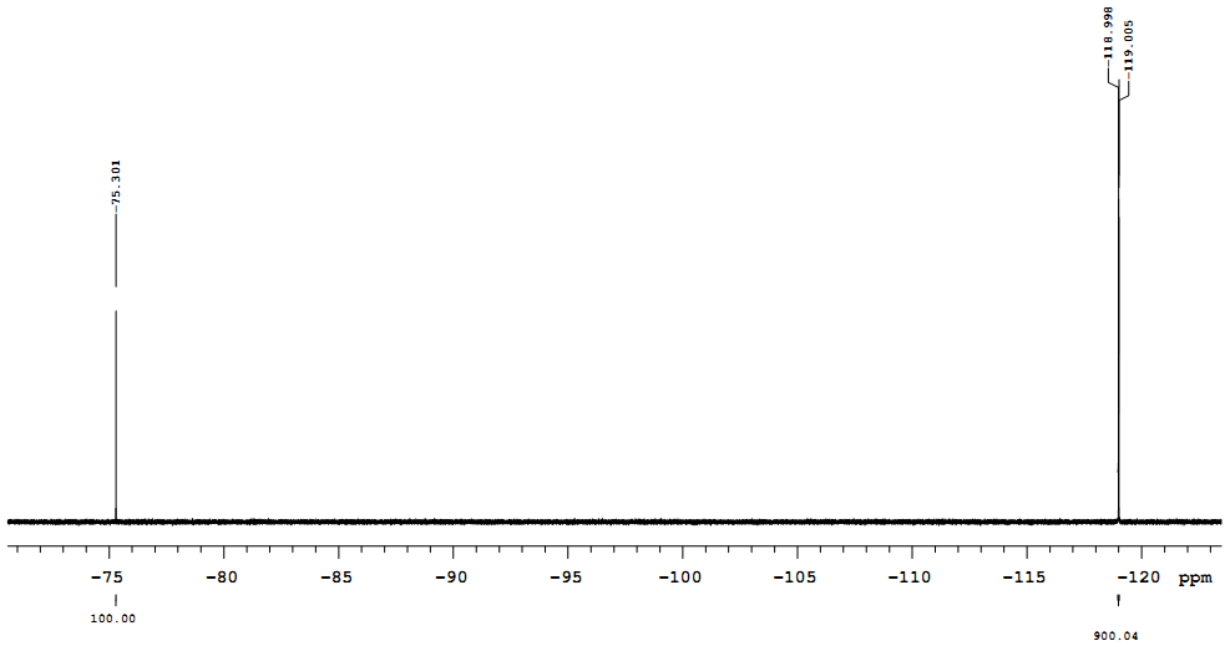

Figure 35 Representative NMR spectrum of GF test effluent

The nature of TFA was only elucidated after the Fenton test experiments had been performed. Due to the need for frequent recalibration of the IC with standards, the concentration of TFA could not be determined after the fact. However, as peak area is approximately proportional to concentration, a plot thereof, adjusted for time and eluent mass, presented in Figure 36, yields a near mirror to the emission of fluoride of Figure 33, showing a reduction in emissions dependent on ceria concentration. The ratio of TFA to F^- adjusted peak areas is, within error, the same for all ceria concentrations. Chen and Fuller [12] had observed the same proportionality of TFA and fluoride in the effluents of OCV hold tests performed at low relative humidity. They considered that the TFA formation was an indicator of side-chain attack, by the

mechanism mentioned earlier and depicted in Figure 9. This confirms that in the GF test, side-chain attack on the ether group adjacent carbon is a significant factor.

In the LF, TFA peaks were only detected for baseline membranes, but were too low to allow for peak area analysis. This supported the theory that end-group unzipping occurred. The baseline membranes showed very high emission of fluoride and the trace amounts of TFA are believed to come from the mechanism described by Xie and Hayden [15], depicted in Figure 10. As the polymer chain is degraded one CF_2 unit at a time, at regular intervals a COOH group adjacent to the side-chain will be attacked, which causes side-chain fragments to split off. These are subjected to further degradation, resulting in TFA and other polymer fragment formation.

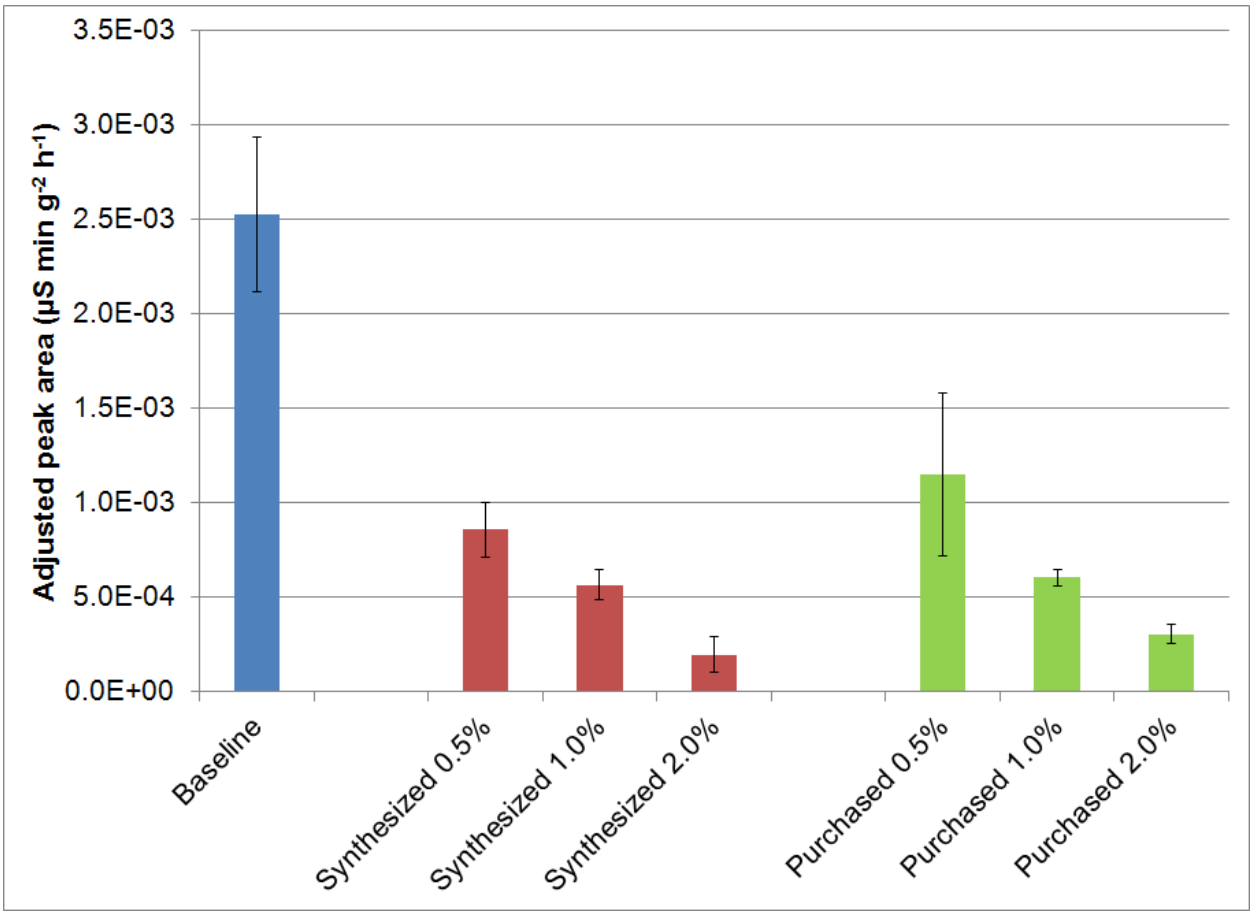

Figure 36 Average TFA emission after 48 h for the gaseous Fenton test

Formic acid is considered to be a side-product that is the consequence of oxidation of carbon-containing compounds by H_2O_2. A PFSA specific reaction mechanism is not proposed. The concentrations of sulfate were found to be too low to perform useful analysis. Other ions were observed in the LF IC spectra but due to the low concentrations, their molecular structures could not be identified by the techniques available.

4.3.3 Discoloration of Gas Fenton Test Membranes

After Fenton tests, membranes were heated in an oven at 100 °C for one hour under vacuum to determine their dry weight. As shown in Figure 37, during this treatment the GF membranes turned brown and gave off a sweet, sugary odor, while also reacting with their tissue paper drying support. This phenomenon was observed even when the membranes were not wrapped in a tissue paper, and the oven was purged with nitrogen prior to drying, making it independent of oxygen. However, the discoloration and odor were less pronounced for the less degraded, ceria-containing membranes.

Figure 37 GF tested membrane after drying in oven: a) baseline and b) synthesized 2.0 wt%

It was postulated that degradation products were responsible for the reactions described. In order to determine the nature of those materials, several mass spectrometry measurements were attempted.

Tested membranes were placed in a closed, though not completely gas-tight, glass vial and heated under the drying conditions described. A sample of the headspace gas was injected into a GC/MS and a DART-MS. In both cases the concentrations of the released gases were too low to obtain spectra that would enable qualitative analysis.

Membranes, before and after drying, were washed in water or acetone to remove soluble species and small amounts of the liquid (1-2 µl) were injected into a GC/MS and a DART-MS. Again, the concentrations of the soluble species were too low to obtain spectra that would enable qualitative analysis.

Pieces of tested membranes before and after drying were placed in a TGA/MS. The membranes were held at the drying temperature under flowing helium. Again, however, the concentrations of the released gases were too low to obtain spectra that would enable qualitative analysis.

Due to the low concentrations of the samples and limitations of the methods and equipment used, the reacting species were not successfully determined. In light of other observations, two suggestions are provided as to the origin of these reactions.

1. Thermal degradation

   The reaction was a thermal degradation of the polymer or polymer fragments. The color change and odor were only observed with GF and not LF membranes. Due to the chain scission degradation mechanisms described in section "4.3.2 Reaction Products" and their effects on the polymer chains, small polymer fragments with lower thermal stability are formed. Exposure to high temperatures resulted in decomposition of these fragments and the subsequent membrane discoloration and odor.

2. Chemical reactions

   The increased temperature upon drying may have accelerated chemical reactions of polymer fragments and other compounds. It is conceivable that small amounts of degradation products, e.g. the highly acidic TFA, reacted with the polymer, polymer fragments and the tissue paper to bring about the color change and odor.

4.4 Conclusion

Perfluorosulfonic acid membranes containing cerium oxide nanoparticles were ion-exchanged with Fe^{2+} and exposed to gaseous and liquid hydrogen peroxide.

The presence of ceria in the membranes was found to affect the uptake of iron(II) ions. Increasing concentrations of ceria resulted in lower concentrations of Fe^{2+} in the membrane. Though the precise origin of this phenomenon was not elucidated, it did not seem to affect the Fenton test measurements.

The Fenton tests resulted in similar levels of baseline degradation. The incorporation of ceria particles showed a concentration-dependent decrease in the emission of fluoride by up to one order of magnitude compared to the baseline. This degradation mitigation is a consequence of the ability of cerium to scavenge hydroxyl and hydroperoxyl radicals. The impact of additive concentration was found to be greater for the gas Fenton test, where the more reactive hydroxyl radical is the main degrading agent. In the liquid Fenton, the hydroperoxyl radicals are more prominent and their longer life-time increases the probability of scavenging by ceria.

Reaction product analysis confirmed end-group unzipping as the main degradation mechanism for the liquid Fenton test, in line with other work reported in the literature. In the gas Fenton test, significant amounts of trifluoroacetic acid were measured, which formed due to side-chain attack by hydroxyl radicals. Exposure of gas Fenton tested membranes to higher temperatures (100 °C) resulted in discoloration and the release of

an odorous gas. Though the precise mechanisms and reactants could not be determined, these observations are thought to be a result of thermal decomposition or chemical reaction of the degraded polymer and polymer fragments.

4.5 References

[1] N.E. Cipollini, Mater. Res. Soc. Symp. Proc., 885 (2006) 33-44.

[2] N.E. Cipollini, ECS Trans., 11 (2007) 1071-1082.

[3] M. Danilczuk, F.D. Coms, S. Schlick, The Journal of Physical Chemistry B, 113 (2009) 8031-8042.

[4] F.D. Coms, H. Liu, J.E. Owejan, ECS Trans., 16 (2008) 1735-1747.

[5] W.E. Delaney, W. Liu, ECS Trans., 11 (2007) 1093-1104.

[6] S. Hommura, K. Kawahara, T. Shimohira, Y. Teraoka, J. Electrochem. Soc., 155 (2008) A29-A33.

[7] F. Finsterwalder, M. Quintus, T. Soczka-Guth, in: Fuel Cell Durability & Performance, Daimler, Ulm, Germany, 2008.

[8] R.A. Day, Jr., A.L. Underwood, Quantitative Analysis. 5th Ed, Prentice-Hall, Inc., 1986.

[9] P. Trogadas, J. Parrondo, V. Ramani, Electrochemical and Solid State Letters, 11 (2008) B113-B116.

[10] M.M. Mench, E.C. Kumbur, T.N. Veziroglu, Editors, Polymer Electrolyte Fuel Cell Degradation, 1st ed., Elsevier Ltd., 2012.

[11] F.D. Coms, ECS Trans., 16 (2008).

[12] C. Chen, T.F. Fuller, Polym. Degrad. Stab., 94 (2009) 1436-1447.

[13] Y. Luan, Y. Zhang, in, CRC Press, 2012, pp. 73-108.

[14] F. Weygand, E. Rauch, Chem. Ber., 87 (1954) 211-214.

[15] T. Xie, C.A. Hayden, Polymer, 48 (2007) 5497-5506.

CHAPTER 5: OCV HOLD TESTS

5.1 Introduction

As mentioned in section "1.3.8 OCV Hold Testing", the OCV hold is an experiment that is very effective at specifically causing chemical membrane degradation in an MEA. At OCV, insignificant amounts of the reactants are consumed. This maximizes gas crossover and thereby radical formation at the electrodes and in the membranes, resulting in maximum degradation without invoking other stress factors such as membrane swelling cycles due to changes in relative humidity. Further, the gas streams are held at low RHs (<50%) which opens up avenues for alternate degradation mechanisms to the primary end-group attack, as outlined in section "1.3.6 Degradation Mechanisms".

An MEAs' health can be monitored by measuring several parameters [1, 2]:

- Hydrogen crossover

  PFSAs are not impermeable to gases and as the membrane is degraded, reactant crossover increases, further promoting degradation. Hydrogen crossover is monitored by linear sweep voltammetry.

- OCV

  The OCV of a cell decreases with increasing hydrogen crossover and is another measure of membrane integrity.

- Emission of fluoride (or other ions and compounds)

  As detailed earlier (section "1.3.6 Degradation Mechanisms"), the most significant product of degradation is fluoride, which can be measured in fuel cell effluents. Other ions, such as sulfate and trifluoroacetate, and compounds, such as polymer fragments, can also be detected. Often, however, their concentrations are so low that meaningful analysis is not possible.

- Performance

  This will be discussed below.

5.1.1 Performance

The performance of a fuel cell is determined from potential-current plots. With flowing gases, the cell is held at various currents and the equilibrium potential is measured. The theoretical potential of the hydrogen-oxygen reaction is 1.23 V at 25 °C (Equation 5.1), though in an actual system the open circuit voltage is found to be below 1 V.

$$H_2 + ½\ O_2 \rightarrow H_2O \qquad E_0 = 1.23\ V \tag{5.1}$$

The difference between these two values is the consequence of mixed potentials, mainly due to inherent kinetic limitations of the reaction and parasitic reactions with crossover hydrogen [3]. Increases in load lead to further decreases in voltage relative to the actual OCV, referred to as polarization. The causes of the potential losses are generally categorized into three regions, which are shown in the schematic in Figure 38. At low current densities, the activation region, where polarization arises mainly due to kinetic limitations of the electrode, such as slow oxygen reduction reactions, platinum oxidation and carbon support corrosion. Potential losses in the ohmic region occur due to resistances, e.g. of the electrodes and the electrolyte (membrane resistance). At high current densities, mass transport of reactants and products to and from reaction sites becomes a limiting factor [2, 4].

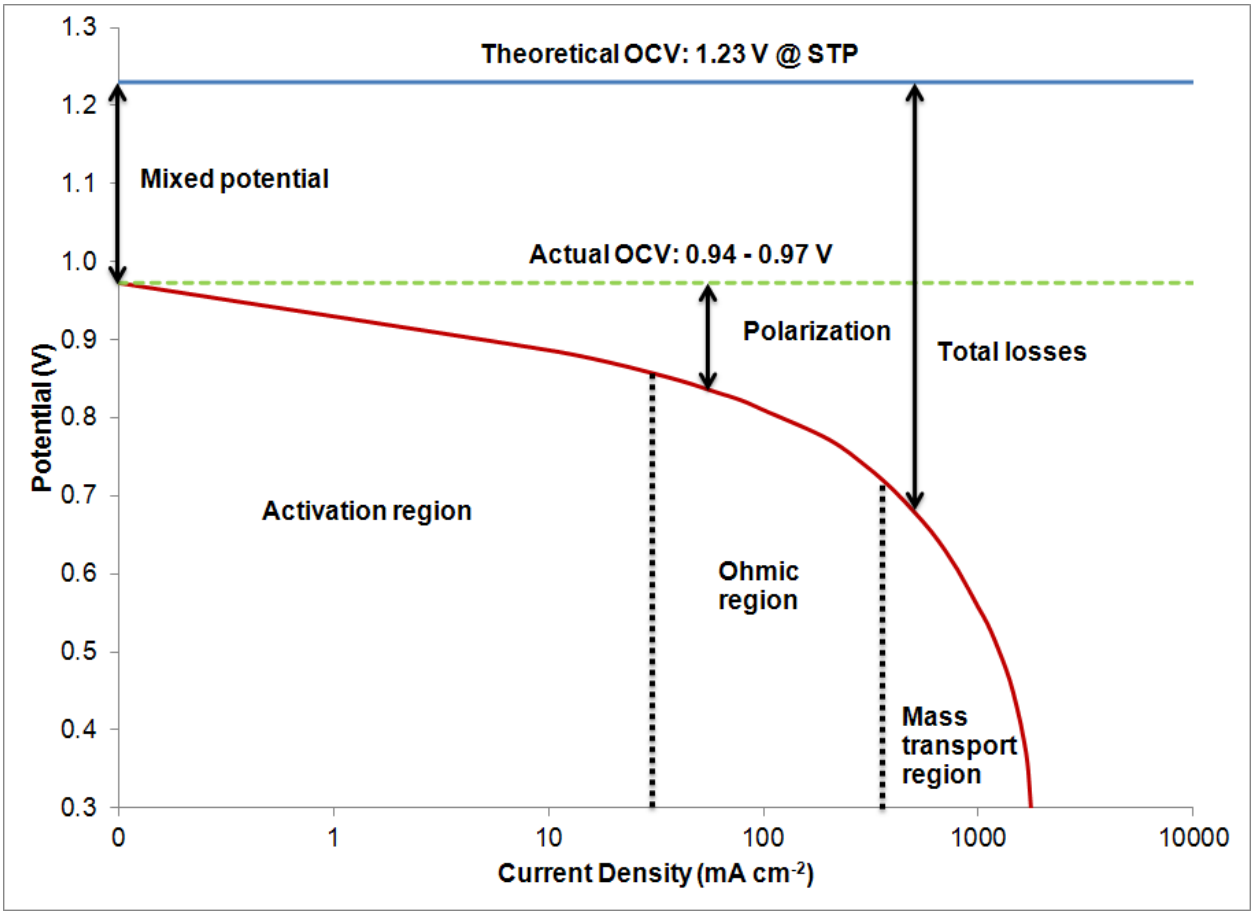

Figure 38 Performance curve schematic with polarization losses

It is desirable to design catalysts, membranes and other cell components to minimize performance losses. Any changes to an MEA's structure, e.g. by degradation or incorporation of additives, become evident by a downward shift in the curve, resulting in lower overall performance. During these measurements, the cell resistance, which contains a number of resistances such as contact and membrane resistances, is determined using a current-interrupt method and can be indicative of changes in the membrane conductivity.

5.1.2 Platinum Dissolution

One side-effect of the high potentials of the OCV hold test is that the platinum catalyst is oxidized [5-7]. The dissolved ions migrate down the potential gradient towards the anode and are reduced in the membrane by crossover hydrogen. As more and more of the catalyst precipitates, a band of Pt nanoparticles is formed. The distance of this band from the cathode has been found to be a function of the hydrogen and oxygen partial pressures [8-12].

The effect that the Pt band has on membrane degradation is still the matter of much debate. Some groups have shown increased membrane decomposition near the Pt precipitation [13, 14]. Using a platinum-cobalt on carbon catalyst, Rodgers *et al.* [15] found that Pt deposited evenly throughout the membrane rather than forming a distinct band. Though they provided no explanation for the origin of this effect, they observed that the fluoride emission was drastically lower than with a Pt/C catalyst, suggesting that the Pt is an important factor in membrane degradation. Others, however, have disputed the role of Pt in membrane degradation [16] and the addition of Pt particles has even been shown to increase durability [17, 18]. A model proposed by Gummala *et al.* [19] suggests that the size and distribution of these platinum particles influences whether they have a significant detrimental impact on to membrane durability.

5.2 94 h OCV Hold Durability Testing

The results of the 94 hour OCV hold tests will be discussed in this section.

5.2.1 Hydrogen Crossover, ECA, and Performance

Two fuel cells with MEAs containing ceria concentrations of 0.5, 1.0 and 2.0 wt% for each ceria formulation as well as three baselines were built and tested. The hydrogen crossover, determined with linear sweep voltammetry was found to be below 1 mA cm^{-2} for all cells and did not change significantly after the 94 h OCV hold. The ECA of the catalyst was found to be around 65 $cm^2Pt\ gPt^{-1}$ and decreased during testing for all cells. This loss of active platinum is considered to be due to particle sintering, crystallite migration and the aforementioned dissolution [9, 20, 21]. No trends were observed with regards to the ECA due to ceria. The addition of ceria to the membranes had no significant effect on either the starting OCV or the performance of their respective cells, an observation confirmed by Trogadas *et al.* [22]. However, Xiao *et al.* [23] arrived at the conclusion that the addition of ceria negatively impacted the performance. Our groups has observed slight variations in performance on a cell to cell basis and attributed it to inhomogeneities in the manufacturing process. Within this error, no significant impact on performance was found. The fact that neither the resistance nor the performance of any ceria-containing MEAs changed indicated that, under OCV hold conditions, ceria was not ionized but remained in its oxide lattice form, thereby not inhibiting proton transport.

5.2.2 OCV Decay and Fluoride Emission

Figure 39 shows the OCV decay rate of the cells over 94 hours as a function of the ceria concentration in the membranes. The addition of ceria reduced the decay rate by approximately 50% compared to the baseline though changes in the concentration of ceria and additive formulation, and therefore particle size, had no significant effect.

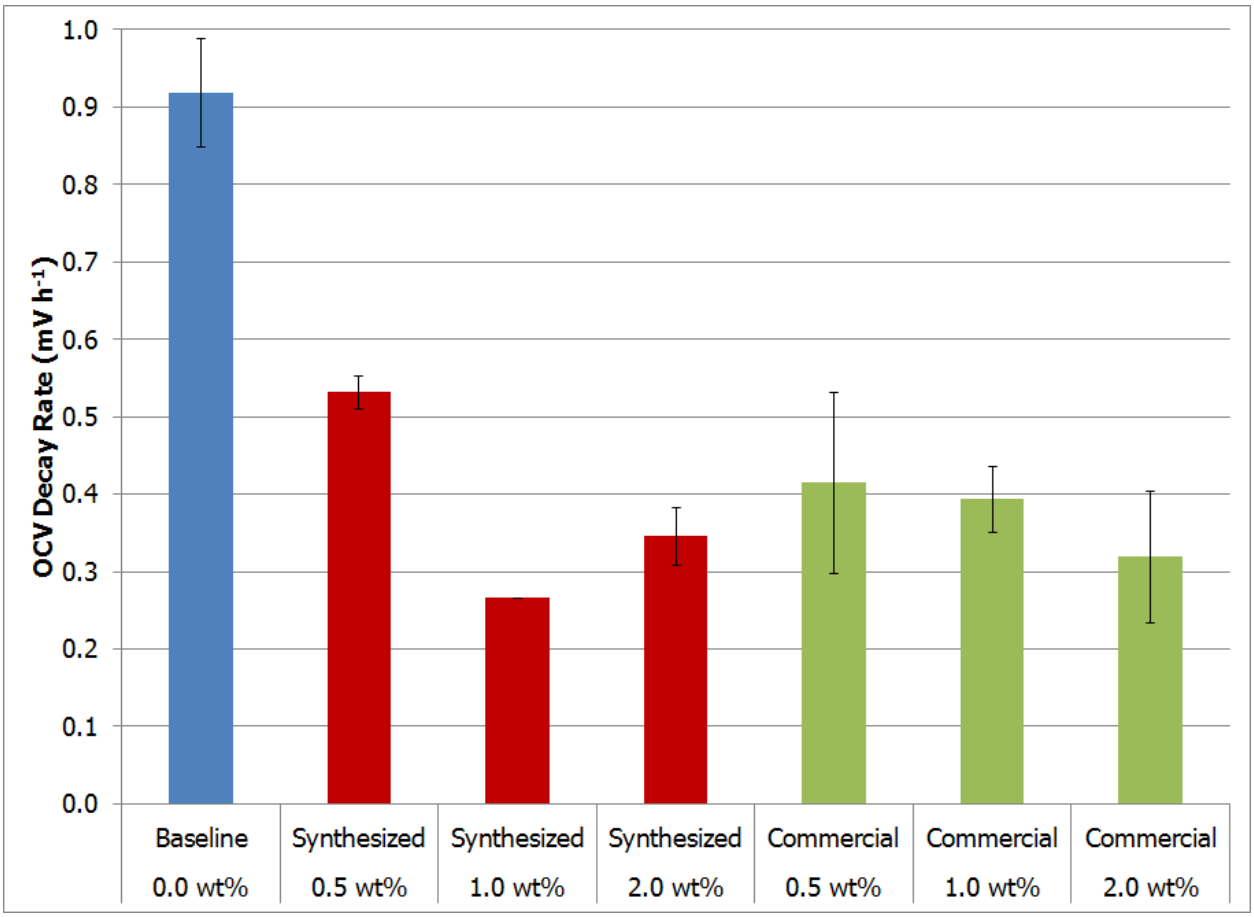

Figure 39 Average OCV decay rates of MEAs in 94 h OCV hold test

While the baseline cells lost between 6% and 18% of their fluorine content, the fluoride ion concentration in effluents released from the MEAs containing ceria were found to be below 1 ppm, which was the limit of quantification (LOQ) of the ion chromatograph used. Based on the LOQ, the ceria-containing MEAs lost less than 0.5% of their fluorine inventory meaning that the addition of ceria reduced the fluoride emission rate by at least one order of magnitude with respect to the baseline MEAs. This indicates that the findings by Trogadas *et al.* [22] made in a 24 hour test hold true even over longer periods of times.

SEM images of cross-sections, as given in Figures 40a-c, showed no significant change in membrane thickness and IR images did not reveal any noticeable pinholes (not shown). For the time period measured, significant membrane degradation occurred in the baseline MEAs while the ceria-containing MEAs were comparatively unaffected.

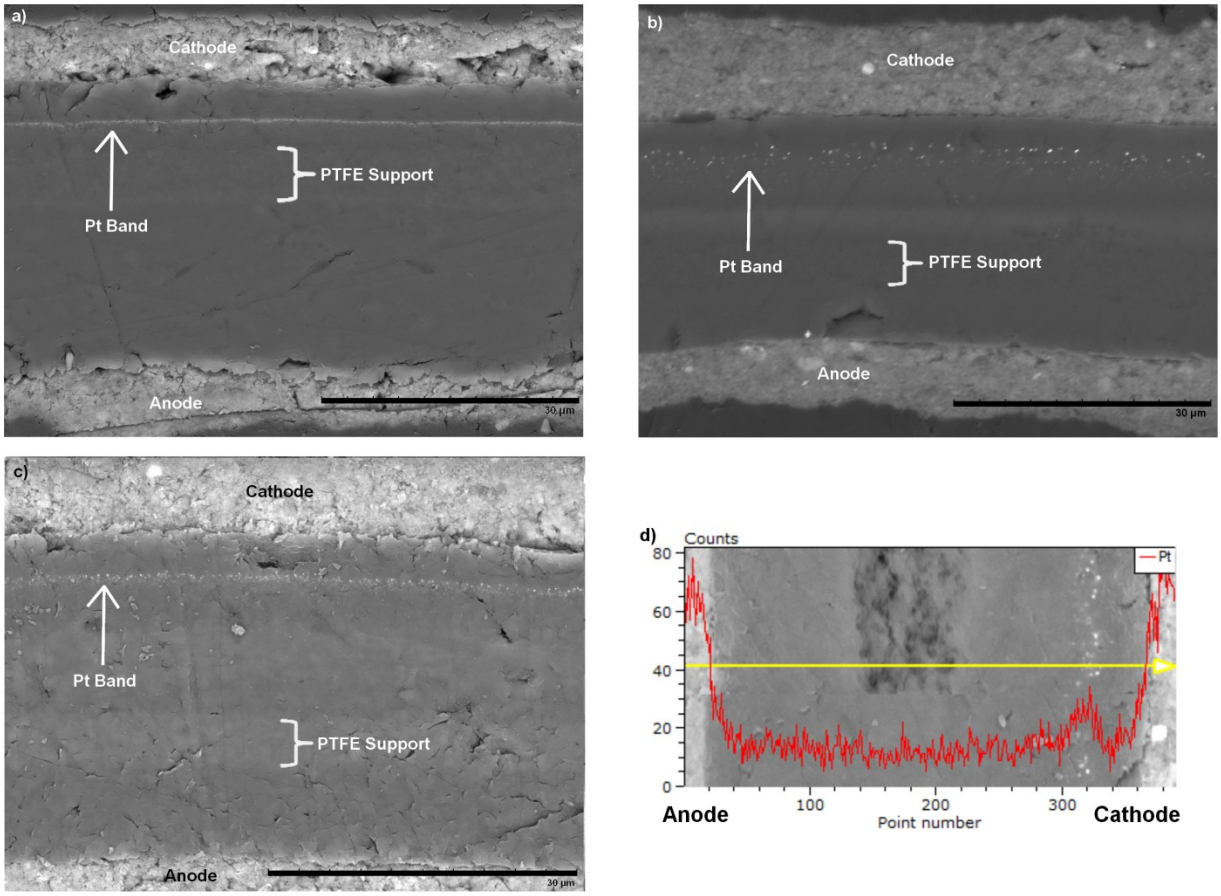

Figure 40 SEM images of 94 h OCV hold tested CCM cross-sections: a) baseline, b) synthesized ceria 2.0 wt%, c) commercial ceria 2.0 wt% and d) commercial ceria 1.0 wt% with platinum EDS spectrum overlap

5.2.3 Pt Band Formation

In Figure 40, SEM images a-c show representative cross-sections of MEAs demonstrating the formation of a distinct band of particles in the membrane at a distance of 3.5 – 4.5 μm from the cathode. The nature of these particles was confirmed by EDS analysis (Figure 40d) to be platinum.

Reports of Pt band particles in the literature have shown that they can be either faceted or dendritic, though the precise mechanism of growth is not well known [5, 24]. Both structures were observed, sometimes even within the same sample. Representative high magnification images of faceted and dendritic particles are given in Figures 41c, d and e, respectively, showing the crystalline nature of both.

The inclusion of ceria into membranes had no effect on the types of Pt particles formed. However, SEM (Figure 40) and TEM images (Figures 41a and b) indicated that fewer particles were present in ceria-containing MEAs. Size and distribution of the Pt particles were determined from STEM images for five MEAs: a baseline, a synthesized ceria 1.0 wt% and 2.0 wt% and a commercial ceria 1.0 wt% and 2.0 wt% MEA.

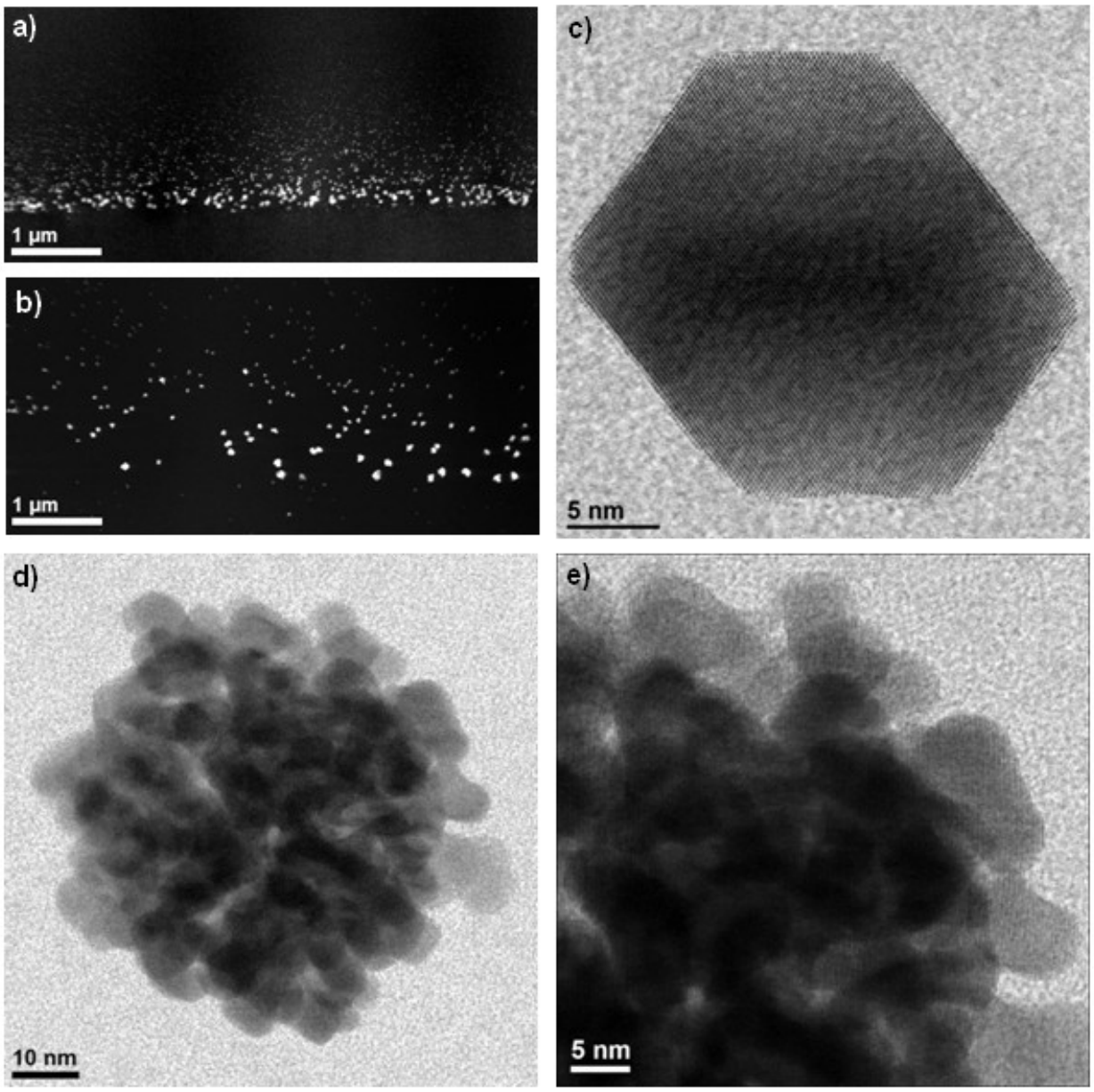

Figure 41 STEM images of cross-sections of 94 h OCV hold tested MEAs: a) Pt band in a baseline MEA (cathode at bottom of image), b) Pt band in a commercial 1.0 wt% MEA (cathode at bottom of image), c) high magnification image of a faceted Pt particle, d) dendritic Pt particle and e) high magnification image of a dendritic Pt particle

As listed in Table 7, the average Pt particle size for the baseline MEA was two to four times smaller than for the ceria-containing MEAs, though it should be noted that there was a significant variation in particle size within each sample. Figures 41a and b clearly show the fading of the Pt band, from many large particles to fewer and smaller particles, with increasing distance from the cathode, a common observation of Pt bands in OCV hold tested membranes [6, 7, 19, 25, 26].

The number of particles per area in the baseline was at least one order of magnitude higher than in the ceria-containing MEAs. The combination of more but smaller particles means that the total area covered by the particles in the baseline was at least three times larger, demonstrating that less Pt had been deposited in the ceria-containing MEAs.

Table 7 Average particle size, relative particle counts and area coverage

		Synthesized		Commercial	
	Baseline	1.0 wt%	2.0 wt%	1.0 wt%	2.0 wt%
Average Particle Size (nm)	19.0±10.1	31.9±26.8	71.3±51.6	50.1±30.1	35.3±21.7
Particle Counts per μm^2	253	8	2	1	24
Area Coverage	9.3%	1.8%	1.3%	0.7%	3.2%

The plot of particle sizes versus the normalized distance from the cathode, shown in Figure 42, supports the previous numerical observations. The basic shape of the particle size-cathode distance distribution is similar for all MEAs. The black line in Figure 42 indicates the theoretical distance of the Pt band from the cathode, calculated according

to references [27] and [28] as a function of hydrogen and oxygen partial pressures. With increasing distance from the cathode, the particles decreased in both size and number. For the ceria-containing MEAs, the Pt particles were noticeably larger and the band extended much further into the membrane than for the baseline MEA. It should be noted that very small Pt particles (<3 nm), observed in some cases beyond the Pt band, and, to a lesser extent, between the cathode and onset of the Pt band, were not included in the measurements.

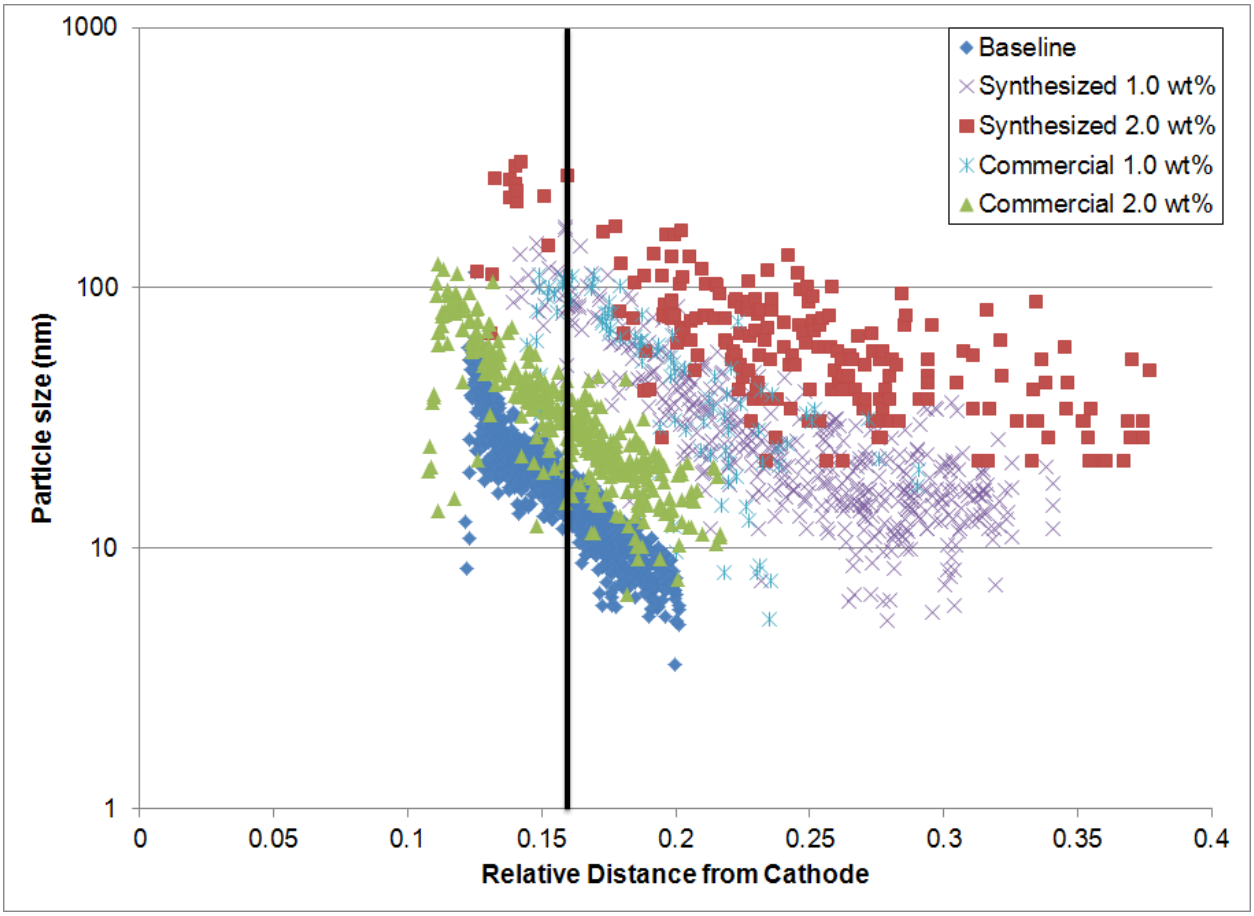

Figure 42 Particle size as a function of normalized distance from the cathode (black line indicates the theoretical location of Pt band, based on references [27] and [28])

Currently it is thought that the nanoparticles are formed by the reduction of diffusing Pt ions by H_2 crossing over from the anode. Due to the crossover of both hydrogen and oxygen, a potential profile for an MEA in a running fuel cell is present. Deposition mainly occurs at the point where the potential rapidly decreases to 0 V, resulting in the formation of the intense band, though particles do form further in the membrane, due to inhomogeneities in the gas crossover and the presence of seeding points [19, 25, 27, 28].

The decrease in the number of particles in the Pt bands of ceria-containing membranes demonstrates that ceria influences the behavior of dissolved Pt. As all MEAs showed a decrease in ECA, it is unlikely that ceria prevented catalyst dissolution. The observation that particles extended further into the membrane, sometimes even all the way to the anode, suggests that the presence of ceria changed the potential profile. Work by Brooker *et al.* [29] has shown that the inclusion of redox-active materials, such as heteropolyacids in a sublayer between the catalyst and the membrane, perturbs the potential profile resulting in the deposition of the metal in said sublayer. The ceria could be acting in a similar manner except that it has the effect of lengthening the Pt band.

It is difficult to ascertain whether the change in the Pt band affects membrane degradation in a positive or negative manner. Radicals can form on platinum from reactions of hydrogen and oxygen. On large particles these radicals are more likely to be quenched before escaping the surface than on smaller particles [19]. This suggests

that in ceria-containing MEAs where larger, and fewer, particles were present, the Pt band contributed less to degradation than in the baseline. However, more research in this area is required, especially with regard to interparticle distance.

5.2.4 Side-Product Analysis

During the IC analysis, other ions were observed in some of the baseline MEA effluents, similar to the Fenton tests. In addition to fluoride and sulfate, typical fuel cell degradation compounds [1] and chloride contaminants, two unknown peaks were observed. Due to low concentrations, the compounds associated with only one of the peaks could be identified. This molecule, as described previously section "4.3.2 Reaction Products", was identified as trifluoroacetic acid. The TFA concentrations were found to mirror the emission of fluoride, which is in line with conclusions reached by Chen and Fuller who described a mechanism of side-chain attack that results in TFA formation [30], which is illustrated in Figure 9. The MEAs containing ceria had very low overall emission of degradation products and no peak for TFA was observed in their IC spectra, demonstrating that the additive was effective at reducing all radical attack.

5.3 500 h OCV Hold Durability Testing

The 94 h OCV hold tests showed a large reduction in the amount of fluoride released and the OCV decay rate as a consequence of the addition of cerium oxide to the membranes. However, the time frame was too short to measure any significant impact on performance or membrane thickness. To ascertain the radical scavenging ability of cerium oxide over longer periods of time, 500 h OCV hold tests were performed on a baseline, a synthesized 1.0 wt% and commercial 1.0 wt% MEA. The test conditions, shown in Table 3, were based on DOE specifications [1] which involved higher flow rates than the 94 hour OCV experiment, and were performed under pressure to increase gas crossover and thereby accelerate degradation.

The pretest hydrogen crossover, platinum ECA, and performance were found to be comparable to the 94 h tested MEAs.

One issue encountered during testing was that the synthesized 1.0 wt% MEA developed a defect after ca. 350 h, which lead to a very large increase in hydrogen crossover. As explained below, the nature of the defect was determined to be localized, as opposed to a general failure of the MEA.

The baseline cell degraded severely, losing over half its total fluorine content during the first 100 h of measurement. The MEA remained intact by virtue of the structural integrity provided by the PTFE support. The SEM images in Figures 43a and b show that the membrane thinned considerably, from ~25 μm to 8-10 μm, whereby the membrane

on the cathode side was completely degraded, leaving the PTFE support in direct contact with the electrode. One consequence of the membrane thinning was the development of an electrical short, most likely due to the penetration of carbon fibers through the membrane, which influenced the linear sweep voltammetry measurements. The 25/25/25 LSV data given in Table 8 for the baseline MEA includes the decreased resistance due to the short and though they do not present accurate values for the hydrogen crossover, increased gas permeability is clearly demonstrated. This is further supported by IR images that the MEA developed pinholes, which are visible as intense red spots in Figure 44a.

Table 8 Emission of fluoride, hydrogen crossover, OCV decay rate and resistance data for 500 h OCV hold

	Baseline	Synthesized 1.0 wt%	Commercial 1.0 wt%
Total fluoride emission (μmol)	3800	340	33
Membrane fluorine inventory loss	89%	8%	1%
Pre500h H_2 crossover & shorting current density (mA cm^{-2})	0.73	0.93	1.00
Post500h H_2 crossover & shorting current density (mA cm^{-2})	21.5	10.0	0.80
OCV decay rate (mV h^{-1})	0.847	0.363	0.120
OCV decay rate (mV h^{-1}) until pinhole formation		0.151	0.116
Pre500h resistance @ 400 mA cm^{-2} (mΩ cm)	67	72	78
Post500h resistance @ 400 mA cm^{-2} (mΩ cm)	469	70	85

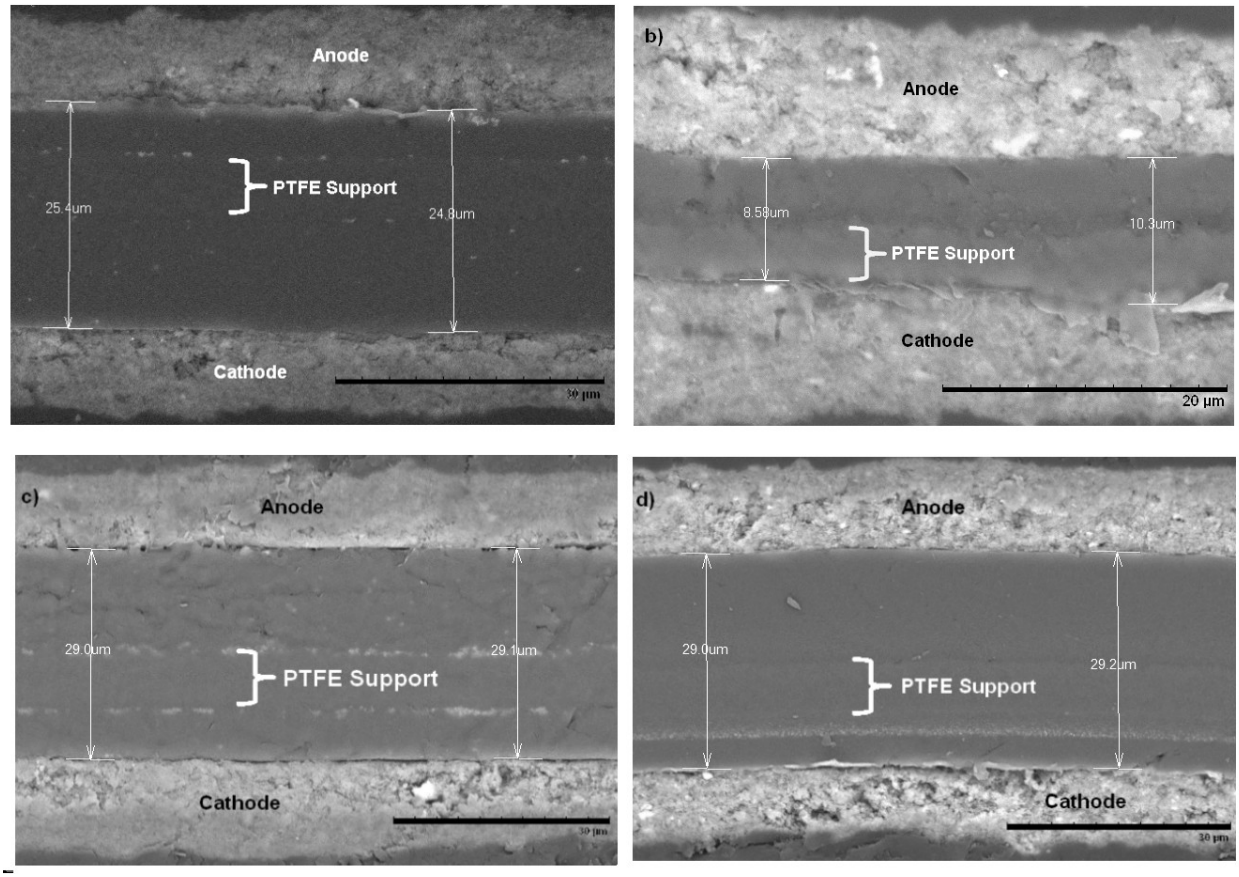

Figure 43 SEM images of CCM cross-sections: baseline a) before and b) after 500h OCV hold test; commercial 1.0 wt% ceria c) before and d) after 500h OCV hold test

The addition of ceria reduced the total amount of fluoride released by one to two orders of magnitude (Table 8). However, such simple comparisons are not adequate. Literature observations of the FER indicate that it generally increases during fuel cell testing [6, 7], which was observed in both ceria-containing MEAs (Figure 45). The baseline cell however, as mentioned, lost the majority of its fluoride within the first 100 h. As shown in Figure 45, its FER actually decreased with comparatively little further degradation occurring after ~150 h, which was due to the complete removal of

the membrane on the cathode side (cf. Figures 43a and b). If more membrane had been available, it is safe to assume that the baseline MEA's total emission of fluoride would have been much greater.

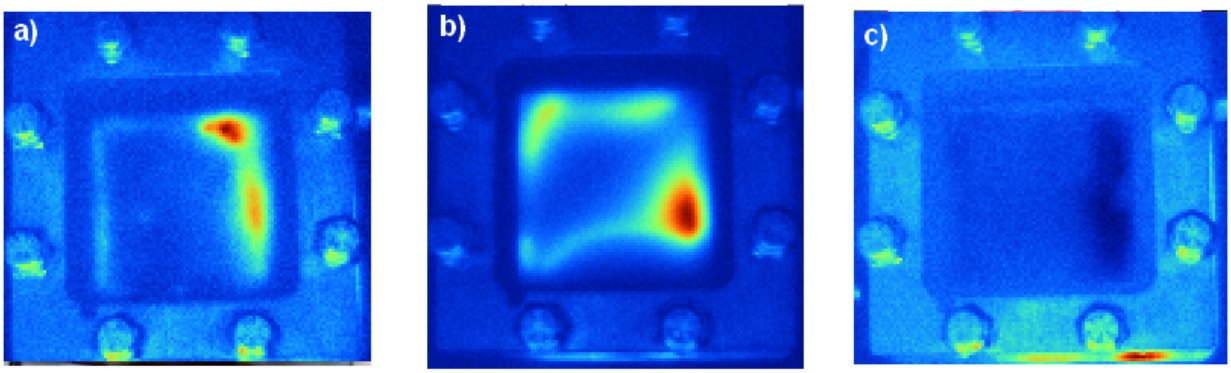

Figure 44 IR images of CCMs after 500 h OCV hold test: a) baseline, b) synthesized 1.0 wt% h and c) commercial ceria 1.0 wt% (red area shows higher temperature caused by reaction of hydrogen and air due to hydrogen crossover)

The fluoride emission of the first 140 h for the synthesized ceria 1.0 wt% and 400 h for the commercial ceria 1.0 wt% MEAs were below the level of quantification. Both membranes showed substantial improvement over the baseline material. Based on the LOQ, the initial FER of the ceria-containing MEAs was two orders of magnitude lower, values in line with those obtained for cerium ion-exchange [1, 31]. Surprisingly, the defect in the synthesized 1.0 wt% MEA did not impact the FER (Figure 45). Prior to the pinhole formation, which is shown in Figure 44b as an intense red area of higher temperature, it had already released approximately half of the total fluoride measured during the experiment (Figure 45). This failure was therefore considered to be localized and not representative of the whole membrane. The amount of fluoride released was

still one order of magnitude lower than the baseline. Throughout the 500 hours of the experiment, the commercial 1.0 wt% MEA lost less than one percent of its total fluorine inventory (Table 8) and showed no change in membrane thickness (Figures 43c and d). IR images, a representative sample is given in Figure 44c, showed no significant hydrogen crossover.

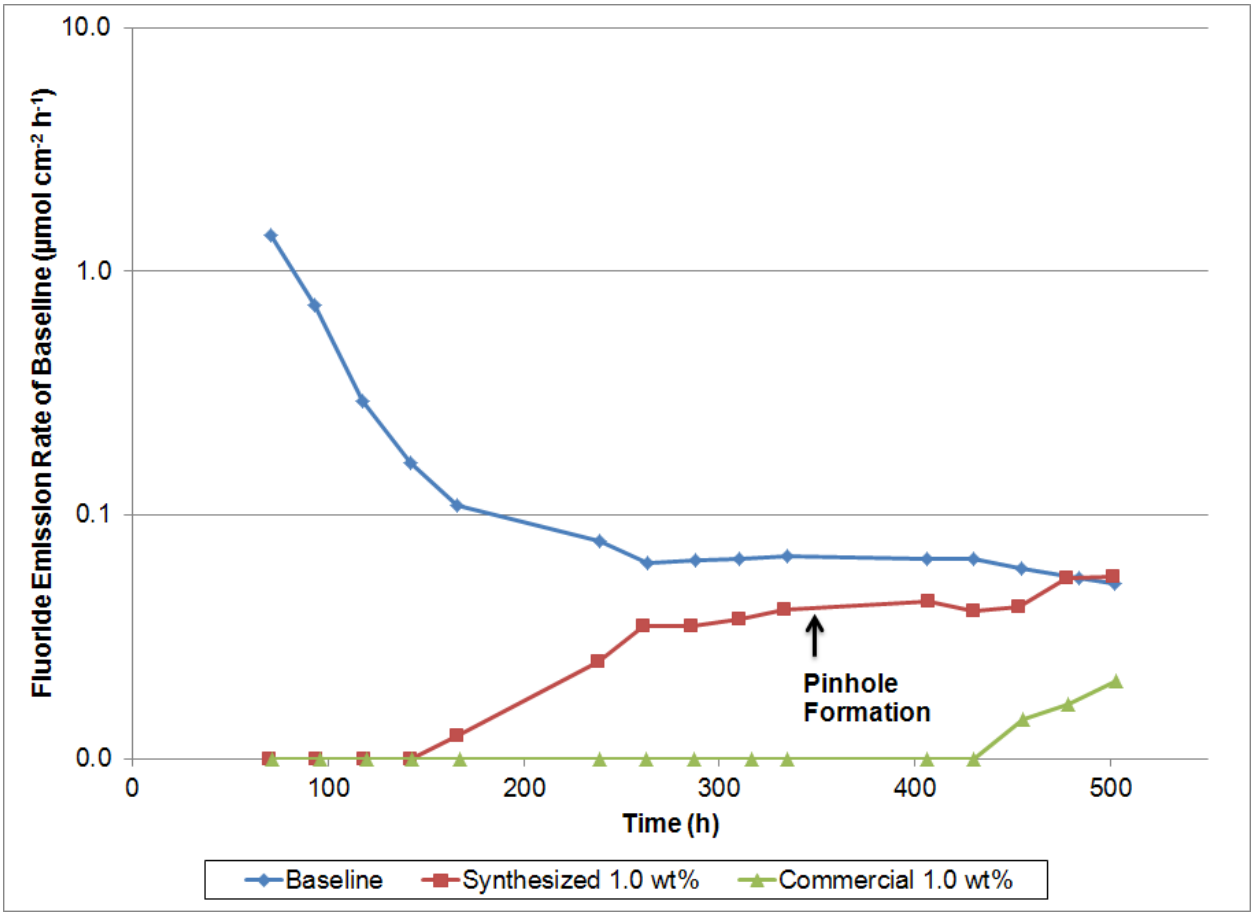

Figure 45 Fluoride emission rates for the 500h OCV hold

Though it did not impact the emission of fluoride, the defect formation in the synthesized 1.0 wt% MEA did increase the OCV decay rate that, until 350 h, had been similar to the commercial 1.0 wt%. The values measured and given in Table 8, ~0.1 mV h^{-1}, are in line with literature data [32]. In Figure 46, the sudden decrease in potential after the pinhole formation can be seen, which correlates well with the rapid increase in hydrogen crossover observed in the daily LSV measurements.

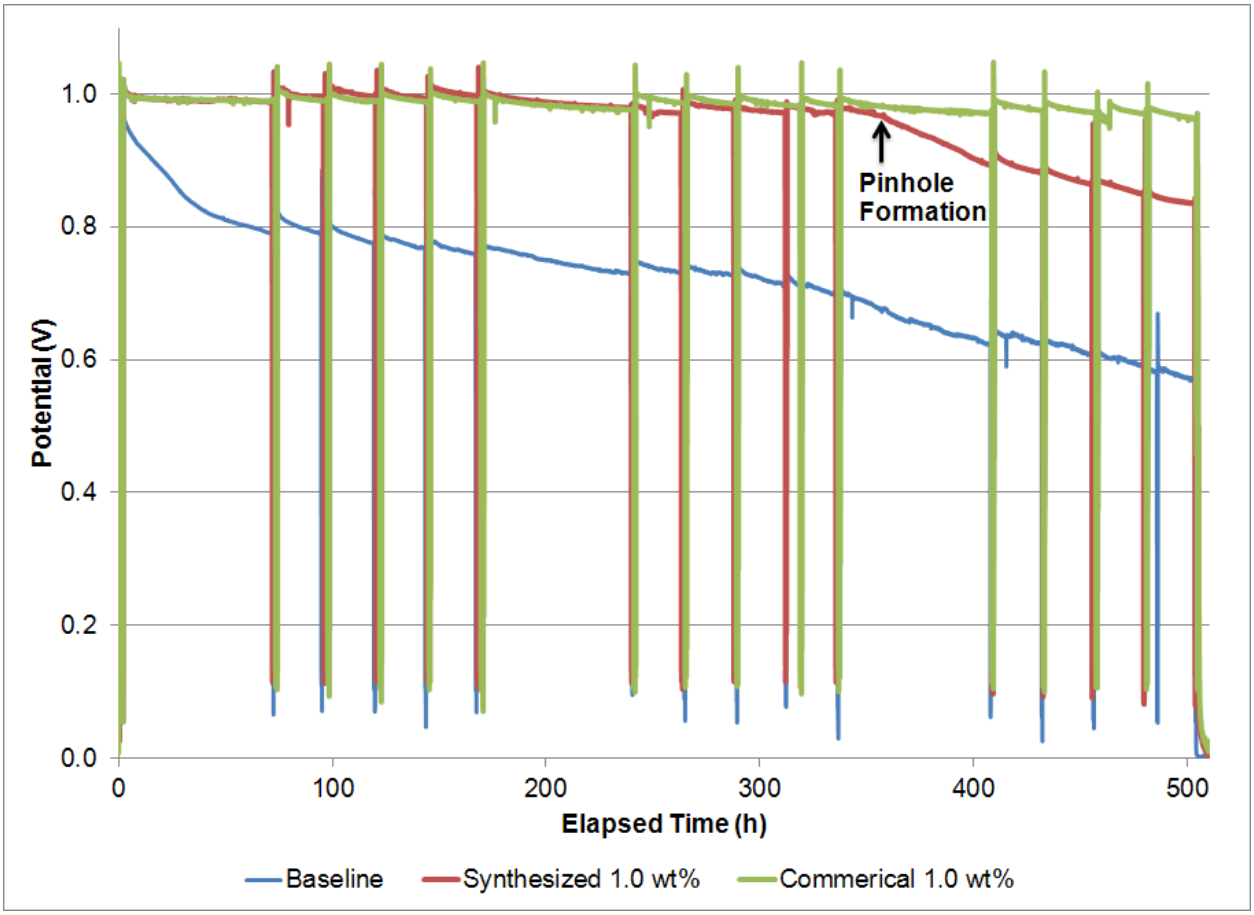

Figure 46 OCV decay for 500 h OCV hold (spikes in potential show breaks in the experiment to perform electrochemical measurements)

The potential plot for the baseline MEA is given in Figure 46 and shows a very fast decay in the first ~40 h due to the large degradation which slows, presumably due the membrane compacting. The overall OCV decay rate was seven times higher than for the ceria-containing MEAs (Table 8).

The membrane degradation had a very large effect on the both the performance (Figure 47) and resistance, which increased seven-fold (Table 8), of the baseline MEA. The performance, which pretest had shown to be very similar to the ceria-containing MEAs, decreased dramatically and did not even pass 400 mA cm^{-2} post-test. The fact that the electrochemical measurements yielded any result was once again due to the PTFE support. The pinhole in the synthesized 1.0 wt% MEA's only affected its performance in the low current density regions (<20 mA cm^{-2}) where the hydrogen crossover has a significant impact on the potential. At higher currents, both ceria-containing MEAs were unchanged with regard to their pretest performance. The commercial 1.0 wt% MEA showed a slight increase in resistance, which is considered to be within the error of the experiment. Otherwise, no significant change in any parameters that would indicate a lowering in proton conductivity was measured. While this provides little reason to believe that cerium oxide is being reduced to Ce^{3+}, more work in this area is needed.

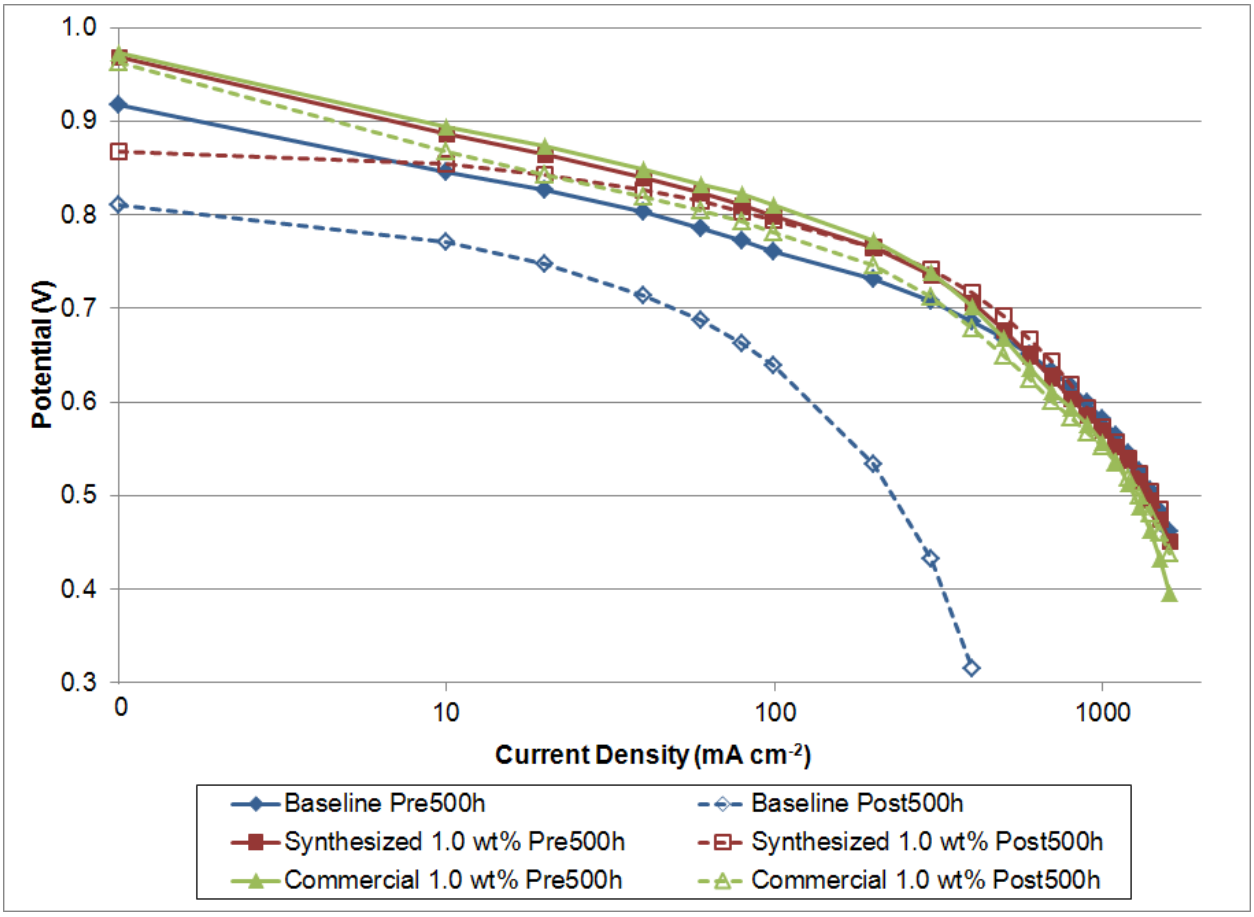

Figure 47 Pre- and post-500 h OCV hold test performance curves

When comparing the 94 h and 500 h test, it is clear that the shorter test is insufficient to demonstrate the very large durability improvement that ceria provides fuel cell membranes. The decrease in total emission of fluoride upon incorporation of the additives for 500 h test was more than an order of magnitude larger than the 94 h test indicated. Barring localized failures, ceria, of either formulation, was able to dramatically inhibit membrane degradation, to the extent that even after 500 h of extreme degradation conditions, it remains nearly pristine.

5.4 Conclusion

Two formulations of crystalline cerium oxide nanoparticles of varying particle sizes, an in-house synthesized and a commercially available material, were added to hydrogen fuel cell membranes that were coated with a platinum on carbon catalyst. These MEAs were held at OCV with hydrogen and air for 94 and 500 hours. Pre- and post-test performance and hydrogen crossover were determined and OCV decay and fluoride emission were monitored throughout.

The 94 h test confirmed the findings in shorter tests that cerium oxide acts as a radical scavenger and protects the membrane, reducing both the OCV decay and fluoride emissions dramatically, independent of formulation. The analysis of the platinum particles deposited in the membrane showed that the Pt band formation is also influenced by the presence of this additive. Cerium oxide incorporation resulted in the formation of fewer and larger particles, reaching further into the membrane with less platinum precipitated overall. It is suggested that the potential profile through the membrane is perturbed by the presence of the ceria, resulting in an altered Pt band.

In a 500 h test, a baseline MEA degraded severely, losing nearly 90% of its fluorine inventory. This was accompanied by a high OCV decay, large increase in hydrogen crossover and profound performance deterioration. The MEA survived the test only due to the presence of a mechanically stabilizing PTFE support. Incorporation of ceria reduced the OCV decay rate and fluoride emission dramatically. An in-house

synthesized ceria MEA developed a localized pinhole which impacted its hydrogen crossover and low current performance. Addition of 1.0 wt% of the commercial ceria resulted in a sevenfold decrease in the OCV decay rate versus the baseline while losing less than 1% of its fluorine inventory. It also showed no change in performance and hydrogen crossover, resulting in an essentially unchanged MEA that seems capable of showing the required durability for practical applications.

5.5 References

[1] M.M. Mench, E.C. Kumbur, T.N. Veziroglu, Editors, Polymer Electrolyte Fuel Cell Degradation, 1st ed., Elsevier Ltd., 2012.

[2] F. Barbir, PEM fuel cells : theory and practice, Elsevier Academic Press, Amsterdam ; Boston, 2005.

[3] V. Ramani, The Electrochemical Society Interface, (2006) 4.

[4] M.V. Williams, H.R. Kunz, J.M. Fenton, J. Electrochem. Soc., 152 (2005) A635.

[5] T. Akita, A. Taniguchi, J. Maekawa, Z. Siroma, K. Tanaka, M. Kohyama, K. Yasuda, J. Power Sources, 159 (2006) 7.

[6] N.E. Cipollini, Mater. Res. Soc. Symp. Proc., 885 (2006) 33-44.

[7] N.E. Cipollini, ECS Trans., 11 (2007) 1071-1082.

[8] W. Yoon, X. Huang, J. Electrochem. Soc., 157 (2010) B599-B606.

[9] K. Yasuda, A. Taniguchi, T. Akita, T. Ioroi, Z. Siroma, Physical chemistry chemical physics : PCCP, 8 (2006) 746-752.

[10] J. Peron, D.J. Jones, J. Roziere, ECS Trans., 11 (2007) 7.

[11] W. Bi, G.E. Gray, T.F. Fuller, Electrochem. Solid-State Lett., 10 (2007) B101.

[12] J. Zhang, B.A. Litteer, W. Gu, H. Liu, H.A. Gasteiger, J. Electrochem. Soc., 154 (2007) B1006.

[13] W. Yoon, X. Huang, J. Electrochem. Soc., 157 (2010) B680.

[14] L. Gubler, S.M. Dockheer, W.H. Koppenol, J. Electrochem. Soc., 158 (2011) B755.

[15] M.P. Rodgers, N. Mohajeri, L.J. Bonville, D.K. Slattery, J. Electrochem. Soc., 159 (2012) B564.

[16] E. Endoh, S. Hommura, S. Terazono, H. Widjaja, J. Anzai, ECS Trans., 11 (2007) 1083-1091.

[17] P. Trogadas, J. Parrondo, F. Mijangos, V. Ramani, J. Mater. Chem., 21 (2011) 19381.

[18] P. Trogadas, J. Parrondo, V. Ramani, Degradation Mitigation in PEM Fuel Cells Using Metal Nanoparticle and Metal Oxide Additives, in: Functional Polymer Nanocomposites for Energy Storage and Conversion, American Chemical Society, 2010, pp. 187-207.

[19] M. Gummalla, V. Atrazhev, D. Condit, N. Cipollini, T. Madden, N.Y. Kuzminyh, D. Weiss, S. Burlatsky, J. Electrochem. Soc., 157 (2010) 7.

[20] C.G. Chung, L. Kim, Y.W. Sung, J. Lee, J.S. Chung, Int. J. Hydrogen Energy, 34 (2009) 8.

[21] L. Kim, C.G. Chung, Y.W. Sung, J.S. Chung, J. Power Sources, 183 (2008) 9.

[22] P. Trogadas, J. Parrondo, V. Ramani, Electrochemical and Solid State Letters, 11 (2008) B113-B116.

[23] S. Xiao, H. Zhang, C. Bi, Y. Zhang, Y. Ma, X. Li, H. Zhong, Y. Zhang, J. Power Sources, 195 (2010) 8000-8005.

[24] P.J. Ferreira, Y. Shao-Horn, Electrochem. Solid-State Lett., 10 (2007) 4.

[25] S.F. Burlatsky, V. Atrazhev, N. Cipollini, D. Condit, N. Erikhman, ECS Trans., 1 (2006) 239-246.

[26] F.D. Coms, H. Liu, J.E. Owejan, ECS Trans., 16 (2008) 1735-1747.

[27] V.V. Atrazhev, N.S. Erikhman, S.F. Burlatsky, J. Electroanal. Chem., 601 (2007) 251-259.

[28] R.M. Darling, J.P. Meyers, J. Electrochem. Soc., 150 (2003) A1523.

[29] P. Brooker, Journal of the Electrochemical Society (accepted), (2012).

[30] C. Chen, T.F. Fuller, Polym. Degrad. Stab., 94 (2009) 1436-1447.

[31] F.D. Coms, ECS Trans., 16 (2008).

[32] S. Xiao, H. Zhang, C. Bi, Y. Zhang, Y. Zhang, H. Dai, Z. Mai, X. Li, J. Power Sources, 195 (2010) 5305-5311.

CHAPTER 6: SUMMARY AND FUTURE OUTLOOK

One of the main obstacles hindering the wide-spread commercialization of polymer electrolyte membrane hydrogen fuel cells is their insufficient life-time. Of the various components, the ionomer membrane is of particular concern. Perfluorosulfonic acid polymers degrade chemically by workings of radicals formed during fuel cell operation. Hydroxyl and hydroperoxyl radicals, formed through chemical or electrochemical reactions between hydrogen, oxygen and catalytic metals, particularly platinum, attack vulnerable groups, such as carboxylic acid, sulfonic acid and ether groups, resulting in the emission of hydrogen fluoride, trifluoroacetic acid, sulfate and other compounds. In this work, an approach to increase the chemical durability of the polymer electrolyte membrane, by incorporation of radical scavenging additives, was investigated.

Cerium oxide nanoparticles of two formulations, an in-house synthesized and commercially available material, were characterized, incorporated into perfluorosulfonic acid membranes and subjected to accelerated durability tests. The synthesized ceria was found to be made up of 2 – 5 nm, the commercial ceria of larger, 20 – 150 nm single-crystal nanoparticles.

In proton conductivity measurements of membranes containing the additives, the ceria particles were found to move through the membrane and be reduced to Ce^{3+} ions with the protons of the superacid ionomer providing the driving force. This decreased the conductivity at least threefold.

Iron(II) ion-exchanged membranes were exposed to hydrogen peroxide in liquid and gaseous phase Fenton experiments. Both accelerated durability setups resulted in approximately the same amount of degradation of the baseline materials. Addition of ceria to the membranes improved the durability significantly, reducing the emission of fluoride by up to one order of magnitude. The extent of the radical quenching of the ceria nanoparticles, which arises due to its ability to switch between its Ce^{3+} and Ce^{4+} oxidation states, was dependent on its concentration but not on the particle formulation and therefore particle size. The impact of the additive concentration was significantly greater in the gas Fenton test. It was postulated that in the liquid experiments hydroxyl radicals react with hydrogen peroxide to form hydroperoxyl radicals. The longer lifetime of this less reactive radical increased the probability of their being quenched by ceria.

Membranes were also fabricated into membrane electrode assemblies by spraying on a platinum-containing catalyst layer, and subjected to accelerated durability fuel cell tests. MEAs were held at open-circuit voltage with hydrogen and air at low relative humidities for 94 and 500 hours, conditions that causes maximum chemical membrane degradation. One side-effect of the high potentials involved in these experimental conditions is that the catalyst is oxidized at the cathode. The resulting ions diffuse through the MEA and are reduced in the membrane by crossover hydrogen. In the shorter tests the addition of ceria cut the OCV decay rate in half and reduced the fluoride emission rate below the limit of quantification (at least tenfold). No significant impact on membrane thickness, hydrogen crossover or performance was measured. In

electron microscopy imaging, the formation of a platinum band was observed in all membranes. Pt particle sizes and relative locations to the cathode were determined from high-magnification scanning transmission electron microscopy images. The addition of ceria resulted in the formation of a more diffuse Pt band consisting of fewer, larger particles that reached further into the membrane than in the baseline MEA. A ceria formulation or concentration dependence could not be determined. It was theorized that the incorporation of the redox-active compound perturbed the potential profile experienced by the membrane due to hydrogen and oxygen crossover. This resulted in the extension of the platinum band.

In the 500 h OCV hold tests, the baseline MEA degraded significantly and endured the whole test by virtue of its included perfluorinated support. It lost nearly 90% of its fluorine inventory, leading to significant membrane thinning (25 μm down to 8 – 10 μm). This resulted in the formation of a short, significant increase in hydrogen crossover and thereby an over 40% decrease in its OCV. The cathode side of the membrane was completely decomposed, placing the perfluorinated support in direct contact with the electrode. This increased the resistance sevenfold and concomitant loss in performance rendered the cell unusable. In comparison, the incorporation of 1.0 wt% cerium oxide reduced the fluoride emission by two orders of magnitude, showed no measurable membrane thinning or change in hydrogen crossover and a seven-fold lower OCV decay rate. Post-test performance was unchanged yielding a nearly pristine membrane after 500 hours of harsh durability experiments.

Though many of the numerous questions that arose, concerning ceria's behavior in accelerated durability tests, were answered, there are some areas where further work is required.

The reduction of cerium oxide to Ce^{3+} ions was observed in ex-situ proton conductivity experiments. However, none of the parameters that were monitored in fuel cell testing, notably cell performance and resistance, demonstrated that the same reaction was taking place. Given that the total cell resistance is made up of several different parts, only one of which is the membrane resistance, more precise measurements are required to elucidate the impact, if any, of cerium oxide on membrane performance.

In solution experiments and proton conductivity measurements, the kinetics of dissolution and reduction of the commercial ceria were slower, which was considered to be due to the larger particle size and unknown synthetic method. For most of the degradation experiments, there was little difference in the durability improvement between the two formulations used. The exception to this was the 500 hour test, where the commercial ceria MEA exhibited lower fluoride emission than the synthesized MEA. Whether this improvement was due of the type of ceria used or merely experimental variation (only one of each membrane was tested) requires repeated experiments. Elucidation of the chemical behavior of ceria in-cell would help in the design of improved formulations and methods of incorporation that are resistant to reduction, dissolution or other reactions.

Though the diffusion of ceria was observed in both conductivity and fuel cell measurements, its final location or vector of movement were not determined. In light of the possibility of ionization and loss of radical scavenger by diffusion outside the active area, further study needs to be performed. The size and shape of nanoparticles could be modified to inhibit movement. Other possible approaches involve methods to fix the additive in place by use of sterically hindered materials, such as crown ethers. The membrane fabrication method could be altered to achieve similar effects. A synthetic method where ceria is formed directly within the polymer membrane has been suggested. This offers the possibility of inhibiting the movement of the particles by forming a network of inorganic oxide, which could also improve mechanical properties, though its impact on proton conductivity and performance would need to be taken into account.

In terms of the Pt band formation, many questions regarding the impact of deposited catalyst particles on membrane durability in general remain. The change in precipitation behavior due to the addition of ceria is of great interest. Elucidation of this phenomenon, by modeling or further experiments, would provide insight into the formulation of other additives. These could be included in electrodes, to reduce the loss of platinum catalyst which is a significant factor in terms of performance and cost of a fuel cell, and membranes, to decrease precipitation of metals which may contribute to membrane degradation.

The final result of all this work would be the optimization of the whole process. Adjustments in the synthesis of cerium oxide nanoparticles to control particle size, shape and oxidation states, combined with the method of incorporation into membranes would result in improved mechanical, physical and chemical properties. This in turn would lead to even more durable polymer electrolyte hydrogen fuel cell membranes.